The Design of an Axial Flow Fan for Air-Cooled Heat Exchanger Applications

by

Michael Briers Wilkinson

Thesis presented in partial fulfilment of the requirements for the degree of Master of Engineering (Mechanical) in the Faculty of Engineering at Stellenbosch University

Declaration

By submitting this thesis electronically, I declare that the entirety of the work contained therein is my own, original work, that I am the sole author thereof (save to the extent explicitly otherwise stated), that reproduction and publication thereof by Stellenbosch University will not infringe any third party rights and that I have not previously in its entirety or in part submitted it for obtaining any qualification.

Date: ....

Abstract

The Design of an Axial Flow Fan for Air-Cooled Heat Exchanger Applications

M.B. Wilkinson

Department of Mechanical and Mechatronic Engineering,
University of Stellenbosch,
Private Bag X1, Matieland 7602, South Africa.

Thesis: MEng (Mech)

December 2017

Large air-cooled heat exchangers are used to cool process fluids in thermodynamic cycles in a range of industrial processes. These systems consume less water than wet-cooled systems and thus have major environmental and economic benefits. Axial flow fans are used to force air through the heat exchanger bundles of mechanical draft air-cooled heat exchangers, allowing heat to be transferred from the process fluid to the ambient air. Distorted inflow conditions can occur in large air-cooled heat exchangers reducing fan performance and therefore heat transfer. Recent trends of using high volume flow rate, low pressure rise fans in these applications have led to a requirement for a fan designed for the specific conditions encountered in these systems.

An axial flow fan for a forced draft air-cooled heat exchanger is designed with the aim of attaining as high as possible total-to-static efficiency at a given operating point. The design procedure is carried out by means of an algorithm which optimises both the flow distribution through the fan, as well as the blading for maximum total-to-static efficiency. Aerofoil selection and its effect on total-to-static efficiency is also taken into account using XFOIL, a program which provides a range of aerofoil design and polar prediction tools.

The procedure results in the M-fan. The performance of the M-fan is assessed using computational fluid dynamics (CFD) by means of a periodic three dimensional numerical model (P3DM). An actuator disk model (ADM) is also developed with the aim of providing a simplified numerical model for future use, as well as to assess to possibility of using the ADM as a design tool. Results obtained from the P3DM and ADM indicate that the design assumptions made are reasonable and that the fan meets the design requirements

under ideal conditions. The P3DM predicts a fan total-to-static efficiency of 59.4% at the design point, with the ADM predicting 63.1%.

Further numerical results obtained using the P3DM indicate that the introduction of a tip gap between the M-fan blade tip and shroud has a detrimental effect on fan performance. This results in the M-fan underperforming when operating with the recommended tip gap and a 7.9% drop in total-to-static efficiency. These results also show that the introduction of a tip gap alters the flow field in the vicinity of the entire blade span, not just the tip region, with implications for blade loading and specific work distributions. Reduction of the tip gap is shown to significantly improve fan performance. Further it is also noted that the aerofoil optimisation process may have resulted in poor aerofoil geometry at the blade root.

Based on these results it is recommended that the M-fan is operated with the minimum tip gap reasonably possible. It is also recommended that the blade setting angle be adjusted to ensure the total-to-static pressure specification is met. The results of this study also indicate that further work should be undertaken to improve the aerofoil optimisation process and account for tip gap related effects in the design procedure.

Uittreksel

Die Ontwerp van 'n Aksiale-vloei Waaier vir Lugverkoelde Hittte-uitruiler Toepassings

("The Design of an Axial Flow Fan for Air-Cooled Heat Exchanger Applications")

M.B. Wilkinson

Departement Meganiese en Megatroniese Ingenieurswese,
Universiteit van Stellenbosch,
Privaatsak X1, Matieland 7602, Suid Afrika.

Tesis: MIng (Meg)

Desember 2017

Groot lugverkoelde hitte-uitruilers word gebruik om prosesvloeistowwe in ter-
modinamiese siklusse te verkoel in 'n verskeidenheid van industriële prosesse.
Hierdie sisteme verbruik minder water as nat-verkoelde sisteme en het dus
groot omgewings en ekonomiese voordele. Aksiale-vloei waaiers word gebruik
om lug te forseer deur die hitte-uitruiler bondels van meganiese treklugver-
koelde hitte-uitruilers wat die oordrag van hitte vanaf die prosesvloeistof na die
omgewingslug toelaat. Verwronge invloei-kondisies kan in groot lugverkoelde
hitte-uitruilers voorkom, wat waaier werkverrigting en gevolglike hitte-oordrag
verminder. Onlangse tendense om waaiers met hoë-volume vloeitempo en lae
drukstyging in hierdie toepassings te gebruik, het gelei tot die aanvraag vir 'n
waaier wat vir die spesifieke kondisies wat in hierdie sisteme teëgekom word,
ontwerp is. 'n Aksiale-vloei waaier vir 'n geforseerde treklugverkoelde hitte-
uitruiler word ontwerp met die doel om die hoogs moontlike totaal-tot-statiese
benutting by 'n gegewe operasionele punt te verkry. Die ontwerpprosedure
word uitgevoer deur middel van 'n algoritme wat beide die vloeidistrubisie
deur die waaier, sowel as die lemvorming vir maksimum totaal-tot-statiese
benutting, optimiseer. Die keuse van lemprofiel en die effek daarvan op totaal-
tot-statiese benutting word ook in ag geneem met die gebruik van XFOIL, 'n
program wat 'n reeks instrumente vir lemprofielontwerp en poolvoorbereke-
ning bied. Die prosedure het die M-waaier tot gevolg. Die werkverrigting van
die M-waaier word geassesseer deur die gebruik van berekende vloeistofdina-
mika (CFD) deur middel van 'n periodiese driedimensionele numeriese model
(P3DM). 'n Aandrywerskyfmodel (ADM) word ook ontwikkel met die doel

om 'n vereenvoudigde numeriese model vir toekomstige gebruik te voorsien, en om ook die moontlikheid van die gebruik van die ADM as 'n ontwerpinstrument te assesseer. Resultate verkry van die P3DM en ADM dui daarop dat die ontwerp-aannames wat gemaak is, redelik is en dat die waaier aan die ontwerpvereistes onder ideale toestande voldoen. Die P3DM voorspel 'n waaier totaal-tot-statiese benutting van 59.4% by die ontwerppunt, met die ADM wat 63.1% voorspel. Verdere numeriese resultate wat verkry is met die P3DM dui daarop dat die implementering van 'n puntgaping tussen die M-waaier lempunt en omhulsel 'n nadelige uitwerking op waaier werkverrigting het. Die gevolg is onderprestasie van die M-waaier wanneer met die aanbevole puntgaping gewerk word en 'n 7.9% afname in totaal-tot-statiese benutting. Hierdie resultate dui ook aan dat die implementering van 'n puntgaping die vloeiveld in die omgewing van die hele lemspan, nie net van die punt nie, verander, wat implikasies vir lembelasting en spesifieke werkverspreidings inhou. Daar word aangetoon dat 'n vermindering van die puntgaping die waaier se werkverrigting aansienlik verbeter. Verder word ook bevind dat die lemprofiel-optimiseringsproses moontlik kon lei tot swak lemprofielgeometrie by die lembasis. Op grond van hierdie resultate word aanbeveel dat die M-waaier bedryf word met die minimum puntgaping wat redelik moontlik is. Daar word ook aanbeveel dat die lem se instellingshoek verstel word om te verseker dat daar aan die totaal-tot-statiese drukspesifikasie voldoen word. Die resultate van hierdie studie dui ook aan dat verdere werk onderneem behoort te word om die lemprofiel-optimiseringsproses te verbeter asook puntgaping-verwante effekte in die ontwerpprosedure te verklaar.

Acknowledgements

Dedications

To anyone who finds the work in this thesis of use - good luck!

Contents

List of Figures

List of Tables

Nomenclature

Acronyms

ADM	Actuator disk model
BS	British standard
CAD	Computer aided drawing
CFD	Computational fluid dynamics
CSP	Concentrated solar power
EADM	Extended actuator disk model
GDES	Geometry design routine
NURBS	Non-uniform rational basis spline
P3DM	Periodic three-dimensional model
PJM	Pressure jump model
RAM	Random access memory
REEADM	Reverse engineered empirical actuator disk model
UDF	User defined function

Variables

a	Outer-to-inner radius ratio	[ ]
A	Area	$[\,\mathrm{m}^2\,]$
B	Dimensionless flow rate	[ ]
C_D	Drag coefficient	[ ]
C_L	Lift coefficient	[ ]
c	Absolute Velocity	$[\,\mathrm{m/s}\,]$
c_h	Chord length	$[\,\mathrm{m}\,]$
c_p	Specific heat	$[\,\mathrm{J/kgK}\,]$
D	Drag force	$[\,\mathrm{N}\,]$
d	Diameter	$[\,\mathrm{m}\,]$
F	Force	$[\,\mathrm{N}\,]$
K	Loss coefficient	[ ]
L	Lift force	$[\,\mathrm{N}\,]$

$\dot{m}$	Mass flow rate	[kg/s]
n	Swirl coefficient	[ ]
N	Rotational speed	[RPM]
n_b	Number of blades	[ ]
P	Power	[W]
p	Pressure	[Pa]
$\dot{Q}$	Heat transfer rate	[W]
r	Radius	[m]
Re	Reynolds number	[ ]
RR	Radius ratio	[ ]
s	Tip clearance	[m]
s_p	Circumferential blade pitch	[ ]
t	Dimensionless radius	[ ]
T	Torque	[Nm]
T	Temperature	[°C]
$tan\gamma$	Drag to lift ratio	[ ]
u	Dimensionless tangential velocity	[ ]
U	Blade speed	[m/s]
U_c	Blade tip speed	[m/s]
$u(r)$	Blade Speed as a function of radius	[m/s]
$\dot{V}$	Volumetric flow rate	[m³/s]
v	Dimensionless axial velocity	[ ]
W	Specific work	[J/kg]
w	Relative velocity	[m/s]
x_h	Hub-to-tip ratio	[ ]

Greek Symbols

α	Absolute flow angle	[°]
α_{att}	Angle of attack	[°]
β	Relative flow angle	[°]
Δ	Change in a property	[ ]
ϵ	Swirl factor	[ ]
ξ	Stagger angle	[°]
η_{ann}	Annulus efficiency	[ ]
η_{tt}	Total-to-total efficiency	[ ]
η_{ts}	Total-to-static efficiency	[ ]
μ	Dynamic viscosity	[Pa.s]

ρ	Density	$[\,\text{kg/m}^3\,]$
σ	Blading solidity	[ ]
ϕ	Flow coefficient	[ ]
ψ	Pressure coefficient	[ ]
ω	Rotational speed	$[\,\text{rad/s}]$

Subscripts

a	Air
act	Actual
atm	Atmosphere
avg	Average
b	Blade
c	Casing
d	Dynamic
D	Design
F	Fan
h	Hub
i	Inner
m	Mean
o	Outer
p	Process fluid
r	Radial direction
ref	Reference
s	Static
$shaft$	Shaft
t	Total
tip	Tip
th	Theoretical
x	Axial direction
θ	Tangential (swirl) direction
1	Inlet
2	Outlet

Chapter 1

Introduction

1.1   Background and Motivation

Large diameter axial flow fans are used in mechanical draft air-cooled heat exchangers to move air through the heat exchanger bundles, allowing the rejection of heat from the process fluid into the ambient air. This type of heat exchanger finds use in many industrial applications such as chemical processing and power generation. Air-cooled systems have a significant advantage over wet-cooled systems in that they minimise water consumption (Kröger (2004)). Air-cooled heat exchangers are therefore well suited to applications such as providing cooling in concentrated solar power (CSP) plants, which are typically situated in desert regions where solar potential is high but water resources are limited. A typical air-cooled heat exchanger makes use of an array of axial flow fans in order to drive air through several heat exchanger bundles. This can result in distorted inflow conditions occurring even under normal operating conditions as shown in figure 1.1, resulting in fans near the edge of the heat exchanger seeing off-design inflow conditions. This effect can be exacerbated by ambient conditions such as wind as well as flow obstructions caused by nearby buildings or walkways. Distorted inflows have been shown to have a detrimental effect on fan performance, and thus the overall heat transfer ability of the heat exchanger, in studies by Salta and Kröger (1995) and Bredell *et al.* (2006).

Efficiency is a major concern when designing an axial flow fan for this application. According to EPRI (2004) the capital outlay required for air-cooled heat exchangers is typically 3.5 times higher than for wet-cooled systems. In addition growing environmental concerns have led to legislation such as European Commission Regulation (EU) No. 327/2011 which stipulates minimum efficiency requirements for axial flow fans in order to reduce their environmental impact. Recent trends of using low pressure rise, high volume flow rate fans in air-cooled heat exchangers have led to the requirement for highly efficient axial flow fans designed to perform effectively under the unique operating
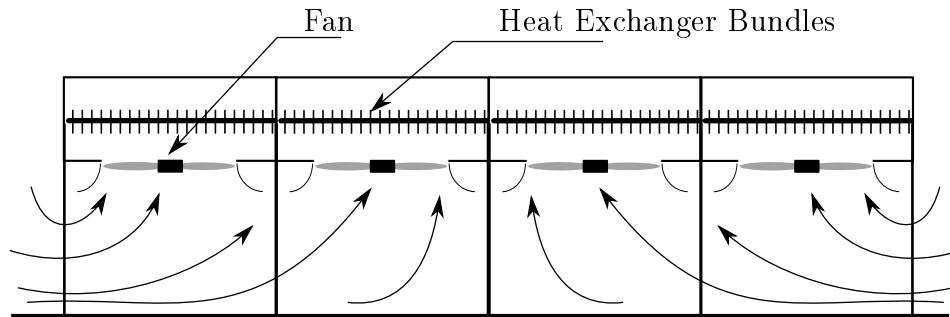
Figure 1.1: Depiction of distorted inflows into an air-cooled heat exchanger under ideal operating conditions

conditions found in these systems.

Bruneau (1994) carried out a study that aimed to design a new high performance rotor only axial flow fan to replace existing power plant air-cooled condenser fans, which resulted in the B1 and B2 fans. The B-fan used by Van der Spuy (2011) and the B2a-fan used by Louw (2015) are refinements of the B2-fan. The aim of Bruneau's study stemmed from the work of Venter (1990) who showed that fan performance could be improved by reducing reversed flow at the hub. The method used by Bruneau was largely based on the work of Wallis (1983) and Dixon (1978) and made use of a modified free vortex assumption. Testing has shown these fans to have better performance characteristics than the existing fans, especially under reduced flow conditions resulting from distorted inflow conditions , as well as improved fan total-to-static efficiency. Further work by Bredell *et al.* (2006) and Van der Spuy (2011) has shown the B-fan to be less sensitive to distorted inflow conditions than other fans designed for air-cooled heat exchanger applications.

Since the completion of Bruneau's research much work has been carried out in fan design. This work has largely been driven by improvements in numerical modelling techniques that have resulted in better understanding of the flow structures around axial flow fan blading. While the majority of recent work in fan design focuses on low noise design requirements, several studies have also resulted in improvements in fan efficiency. This includes work on understanding three dimensional flows carried out by Vad and Bencze (1998), optimisation studies carried out by Bamberger and Carolus (2012) and tip modifications to reduce noise and improve performance by Corsini *et al.* (2010) to name a few. Tools such as XFOIL (Drela (1989)) have reduced the reliance on experimental testing for aerofoil data as well as providing tools to develop aerofoils for specific applications, such as axial flow fans. These developments have led to a better understanding of the flow mechanisms in axial flow fans as well as improved design methods.

Improvements in numerical methods and computational power have resulted in the ability to accurately model axial flow fans by means of computational fluid dynamics (CFD) software. An example of this is the numerical model

used by Louw *et al.* (2015) in order to model the B-fan. Three dimensional explicit models such as that of Louw *et al.* (2015) show good correlation with experimental fan data as well as providing valuable insight into the flow field around the fan blades. While highly accurate, these models are computationally expensive and require very fine meshing. This creates a need for simplified numerical models which can be used to represent axial flow fans in numerical simulations of air-cooled heat exchanger systems. The actuator disk model (ADM) of Thiart and Von Backström (1993) is one such simplified fan model which makes use of blade element theory to replicate the influence of a fan on a flow field. The ADM currently makes use of experimental data sets, where linear interpolations between data sets are used to approximate Reynolds number effects (Meyer and Kröger (2001)). The requirement for experimental data has proved limiting in the past and tools such as XFOIL provide an opportunity to improve this model. The potential of the ADM to be used as a design aid should also be investigated owing to its advantages in terms of computational expense.

Recent trends have seen a move towards low pressure rise, high volume flow rate fans being required for air-cooled heat exchanger applications. The B-fan was designed to provide a static pressure rise of 210 Pa whereas modern design requirements call for fans with a static pressure rise in the order of 100 Pa. Additionally strict limits on fan blade tip velocities owing to noise requirements increasingly feature in design specifications. This has led to the requirement for a new design procedure that builds on previous work, to be developed in order to generate high efficiency axial flow fan designs for more recent design specifications. Numerical modelling will be used to assess the performance of the design procedure. Additionally the feasibility of using the actuator disk model (ADM) to assess how a fan performs compared to its design data will also be investigated. In order to demonstrate this the design specifications for the MinWaterCSP project (MinWaterCSP (2017)) will be used, although the work presented here aims to be more generally applicable. The MinWaterCSP project is a European Union funded project aimed at reducing water usage in concentrated solar thermal power (CSP) plants while maintaining cycle efficiency (MinWaterCSP (2017)). Improvement of air-cooled heat exchanger systems is one area where the project aims to achieve this. Specifications provided by the project organisation call for a rotor only axial flow fan for a forced-draft air-cooled heat exchanger. This suits the aims of this study as the rotor only fan configuration is most commonly used in air-cooled heat exchangers.

1.2   Research Objectives and Approach

Based on the background given, several main research objectives have been identified:

1. **The development of a design procedure for a rotor only axial flow fan for air-cooled heat exchangers.** The design procedure should be capable of generating designs for high efficiency axial flow fans subject to a variety of design constraints. The design procedure should build on historical work while making use of more recent design tools. The procedure developed will be used to generate a fan based on the design requirements of the MinWaterCSP project for the purposes of validation and analysis. The method developed should however be applicable to other design requirements.

2. **The development and assessment of an Actuator Disk Model appropriate for representing fans developed by the design procedure.** An Actuator Disk Model will be developed based on the work of Thiart and Von Backström (1993). The model developed in this study should reduce the ADM's reliance on experimental data. The ADM should also be able to account for variations in aerofoil profile, thickness and Reynolds number along the blade span. This model should be relatively simple to construct and reasonably computationally inexpensive.

3. **Validation and critical assessment of the design procedure and Actuator Disk Model by means of three dimensional numerical simulations.** A three dimensional periodic blade model will be developed to assess the performance of the fan both in terms of flow field and fan characteristics. Performance should be measured both at the design point as well as at higher and lower flow rates. The model will also be used to gauge the effect of tip-gap on the designed fan as well as validating the actuator disk model developed earlier.

In order to achieve these objectives this thesis first considers relevant literature in Chapter 2, in order to assess recent trends in fan design, flow phenomena as well as design requirements in terms of the intended application of the fan. Chapter 3 then details the design procedure developed, as well as the final design produced. Chapters 4 and 5 provide details of the numerical models used to assess the quality of the design produced. These numerical models are then used to validate the design method, as well as critically assess the performance of the fan. Results from the numerical study are presented and discussed in Chapter 6 before concluding remarks are drawn in Chapter 7.

Chapter 2

Literature Study

This chapter will provide an overview of the literature relevant to this study. A short description of the role of the axial flow fan in an air-cooled heat exchanger system is also provided as the context of the study. This is followed by a review of turbomachinery literature on major aspects of fan design including flow distribution through the fan, blading design, aerofoil selection and fan blade modifications. As numerical modelling will be used extensively in this study in order to estimate performance, an overview of fan modelling techniques is also provided.

2.1   The Air-Cooled Heat Exchanger

In order to provide context for this study a brief overview of the workings of air-cooled heat exchangers is provided. This aims to provide the reader with sufficient background to understand the role of an axial flow fan in an air-cooled heat exchanger, as well as potential design requirements for the fan. This section also aims to provide some background on specific conditions that fans can be exposed to in air-cooled heat exchangers. This information will guide the design procedure in order to produce a fan that is suitable for operation in such a system.

2.1.1   Basic Principles

In general two types of mechanical draft air-cooled heat exchangers are found in industry, forced draft heat exchangers and induced draft heat exchangers. The major difference between the systems being the position of the fan, with the fan being mounted below the heat exchanger bundles in forced draft systems and above in induced draft systems, as shown in figure 2.1.

There are several variations on these two basic configurations, with several possible types of heat exchanger and fan configurations (Kröger (2004)). The basic operating principle for an air-cooled heat exchanger remains the same re-
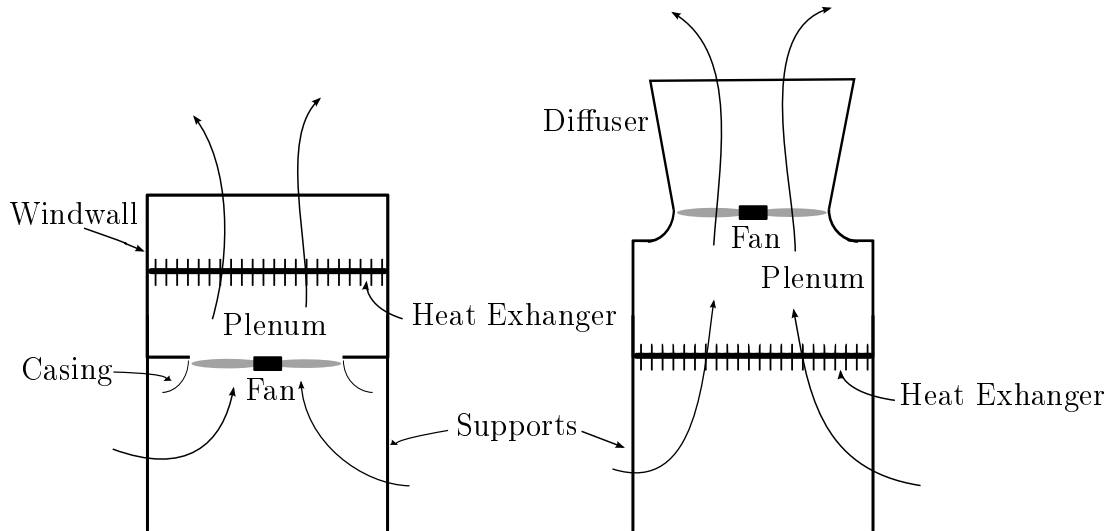
Figure 2.1: Forced draft (L) and induced draft (R) air-cooled heat exchangers (Adapted from Kröger (2004))

gardless of configuration. According to Kröger (2004) the heat transfer ability can be described as follows:

$$\dot{Q} = \dot{m}_a c_{p_a}(T_{a_o} - T_{a_i}) = \dot{m}_p c_{p_p}(T_{p_o} - T_{p_i}) \qquad (2.1.1)$$

The mass flow rate term for air can be rewritten as follows:

$$\dot{m}_a = \dot{V}_F \rho_a \qquad (2.1.2)$$

These equations demonstrate how the volume flow rate provided by the axial flow fan directly influences the heat transfer rate of the air-cooled heat exchanger, with obvious implications for performance. The fan also has to overcome the various pressure losses in the system due to flow obstructions such as walkways and heat exchangers as well as ambient conditions such as wind. Kröger (2004) characterises these pressure losses into a draft equation. The draft equation is specific to each type of air-cooled heat exchanger design, however in general the draft equation serves as an energy balance for the air flow through the system. The draft equation takes into account all pressure loss terms encountered in the system due to flow obstructions and friction and balances them against the pressure rise imparted by the fan. Once the draft equation has been solved for a system and the required pressure rise is known, experimental or simulated data can be used to deduce the volume flow rate provided by the fan and thus the heat transfer capacity of the system can be determined. In general, for a specific fan, if a higher pressure rise is required the volume flow through the system will be reduced, reducing heat transfer.

The type of heat exchanger used in a specific application is usually determined by performance requirements as well as economic considerations. According to Kröger (2004) the design of an air-cooled heat exchanger is heavily

influenced by operating conditions such as temperatures and ambient effects, practicality and process specifications. With this in mind both forced draft and induced draft systems have advantages that can make one system more favourable than the other. Fans in forced draft systems are also better located for ease of maintenance and are not exposed to high temperatures, resulting in the selection of material for the fan blades being less critical, reducing costs. The disadvantages of forced draft systems are that they are highly susceptible to hot plume recirculation and ambient conditions such as wind, both of which have a detrimental effect on performance (Kröger (2004)). According to Kröger (2004), induced draft systems are less sensitive to ambient conditions and due to high air escape velocities, less susceptible to plume recirculation and cross wind effects. Owing to their lower running and construction costs forced draft systems are highly popular in industry, especially in power generation. For this reason this study will focus on forced draft systems, however in practice the design procedure developed is applicable to induced draft systems as well.

2.1.2 Fan Operating Conditions

Axial flow fans in forced draft air-cooled heat exchangers are often exposed to distorted inflow conditions, with the flow pattern resulting from a large array of fans resulting in edge fans being exposed to cross flow (figure 1.1). This cross flow effect can be exacerbated by unfavourable wind conditions, resulting in reduced volume flow through the fans and thus reduced heat exchanger performance. Due to the impact of flow distortions on heat exchanger performance, several studies have been conducted with the aim of better understanding the flow mechanisms present in the vicinity of fans subjected to distorted inflows. A number of these studies have highlighted aspects that should be taken into account when designing a fan for a forced draft air-cooled heat exchanger.

Several early studies aimed to experimentally characterise fan performance in air-cooled heat exchangers under off design conditions. Venter (1990) conducted experimental measurements of the velocity field upstream of an operational fan in ESKOM's Matimba plant's forced draft air-cooled condenser. It was found that wind speed and direction had a significant effect on fan performance, with an increase in wind speed reducing the volume flow rate through the fan. This resulted in the fan operating at off design conditions, reducing fan total-to-static efficiency. Salta and Kröger (1995) experimentally investigated the effect of cross flow on a scaled model of a street of an air-cooled heat exchanger. It was found that the fans at the edge of the air-cooled heat exchanger are worst affected by cross flow, with fan performance improving towards the centre. Stinnes and Von Backström (2002) experimentally investigated the effect of off-axis flow on scaled heat exchanger fans in a BS 848 type A fan test facility. Fan configuration was demonstrated to have an influence on the reduction in volume flow rate encountered when a fan is sub-

jected to off axis flow. Fans with steep total-to-static pressure characteristic curves were shown to pay a smaller penalty in terms of volume flow rate under these conditions. Both Venter (1990) and Stinnes and Von Backström (2002) indicate that fan hub configuration has an influence on fan performance at off design conditions.

Thiart and Von Backström (1993) showed that the off design performance of an axial flow fan could be reasonably estimated by means of a simplified numerical model incorporated into a computational fluid dynamics (CFD) code. A similar numerical model to that used by Thiart and Von Backström (1993) was used by Meyer (2005), who performed a numerical investigation of a system of two banks of air-cooled heat exchangers. Meyer (2005) shows that the large performance loss in the edge fans is due to flow separation occurring around the fan inlet bellmouth, while losses in fans further from the edge of the heat exchanger unit are due to oblique flows at the fan inlets. A comparable study by Bredell *et al.* (2006) investigated the effect of cross-flow and platform height on the performance of two different fans. Bredell *et al.* (2006) attributed the drop in volume flow through the fans under off design conditions to a combination of factors such as increased inflow losses, off axis flow conditions and poor distribution of air flow into the fan resulting in blade stall. Owing to the complex nature of the findings and the fact that a simplified numerical model was used, further insight was not possible. Another finding made by Bredell *et al.* (2006) is that the B-fan of Bruneau (1994) with an optimised hub-to-tip ratio outperformed the more basic A-fan, which had a smaller hub-to-tip ratio, under distorted flow conditions. An extensive numerical and experimental investigation by Van der Spuy (2011) provides further insight into the sensitivity of fans to distorted inflows. Using a number of numerical models as well as experimental investigations of Van der Spuy (2011) investigated the performance of several fans, designed to the same operating point, subjected to distorted inflow conditions. It was found that distorted inflows reduced the volume flow rate through a given fan, potentially resulting in the fan operating outside its design operational range. This potentially leads to fan stall in some cases, however Van der Spuy (2011) indicates that local reductions in flow rate through the fan blades due to factors such as flow separation at the inlet may be more severe. It was also found that fans with higher solidities and larger hub-to-tip ratios were less sensitive to distorted inflows in terms of volumetric effectiveness, however these fans were not necessarily the most efficient in terms of power consumption.

While several of the above mentioned studies also investigated aspects of heat exchanger design, such as walkway positioning and screens, the focus of this study is on the fan itself. With this in mind the following conclusions can be drawn from literature:

- Distorted inflow operating conditions lead to a reduction in volume flow rate through the axial flow fans in an air-cooled heat exchanger, with fans

near the edge of the heat exchanger being worst effected. This reduction in flow rate leads to severe performance losses in the heat exchanger system.

- Axial flow fans with steep static pressure to volume flow performance characteristics experience a smaller loss in volume flow rate when exposed to off design inflow conditions, such as wind or other distortions.

- Several authors indicate that fan hub-to-tip ratio has an influence on fan sensitivity to distorted inflow conditions, making hub-to-tip ratio an important consideration when designing a fan for this application.

- There is an indication from Van der Spuy (2011) that fan blading solidity has an influence on sensitivity to distorted inflow condition, with higher solidity fans generally experiencing a smaller loss in volume flow. It is also however highlighted that there is a trade off between solidity and fan efficiency.

2.2   Axial Flow Fan Design

Axial flow fan design is a widely researched topic globally with many studies being undertaken with the aim of improving fan performance. At Stellenbosch University a range of studies have been carried out on fan design and numerical modelling over the last twenty years, mainly focused on large diameter axial flow fans for air-cooled heat exchangers. This section presents the literature from previous research that is relevant to this study.

2.2.1   Vortex Design

Vortex design entails the design of the flow field downstream of a fan, thus defining the flow through the fan. The aim is to provide the desired flow turning angle to generate the required pressure rise whilst minimising losses and keeping flow angles within a reasonable range. Broadly speaking there are two approaches to vortex design, namely free vortex and non-free vortex.

Classical fan design methods such as those described by Dixon (1978) and Wallis (1983) make use of the free vortex method. The free vortex assumption indicates that the swirl velocity through a fan is inversely proportional to the radius, as shown in equation 2.2.1.

$$c_\theta = \frac{k}{r} \tag{2.2.1}$$

where $k = $ constant.

This assumption has several simplifying benefits, one being that there is no radial flow component ie. $c_r = 0$. Other benefits are that the axial velocity through the blade row is constant, both radially and axially. Work and total pressure distributions along the blade span are also constant. The use of the free vortex method is also indicated to produce fan designs with high efficiencies by several authors including Wallis (1983) and Van Niekerk (1958). The lack of a radial flow component in the free vortex distribution means that simple two dimensional blade element theory can be used to design the fan blading, greatly simplifying the fan design procedure. This technique was used by Bruneau (1994) in the design of the B fans. Tests of the B2a fan, a variant of the original B2 fan (Louw *et al.* (2012)), have shown operating point total-to-static efficiencies in excess of 60%. The fan was also shown to perform better at off design conditions than existing fans for similar applications at the time (Louw *et al.* (2012)). Van Niekerk (1958) investigated the limiting theoretical total-to-static efficiencies of free vortex rotor-only axial flow fans and found that depending on design specifications, total-to-static efficiencies in excess of 70% are possible. Other design studies such as that of Dugao and Jiang (1996) demonstrate the effectiveness of the free vortex method, where a free vortex fan was found to have improved efficiency as well as reduced noise emissions compared to an existing fan for the same application.

The free vortex method does however have limitations as the flow distribution can result in unrealistically high flow turning angles near the hub. This can lead a fan to stall, even at design point. In order to counteract this Wallis (1983) suggests limiting the swirl coefficient at the hub, where swirl coefficient is defined as follows:

$$\epsilon(r) = \frac{c_\theta(r)}{c_x(r)} \tag{2.2.2}$$

In order to improve efficiency and obtain reasonable flow turning angles at the hub Bruneau (1994) makes use of the hub-to-tip ratio optimisation method of Van Niekerk (1958). This technique aims to optimise the hub-to-tip ratio of a free vortex axial flow fan with inlet guide vanes and flow straighteners, however Bruneau (1994) adapted the technique to apply to rotor only fans. Van Niekerk (1958) also suggests that this technique can be extended to non-free vortex fans. The method, as used by Bruneau (1994), takes into account estimates of various system losses at the operating point, as well as the swirl coefficient limitations of Wallis (1983) in order to optimise the hub-to-tip ratio for maximum static efficiency, while ensuring reasonable flow angles at the hub. However in several applications this design method is limiting as it can still result in unrealistic twist distributions, or designs that do not meet physical or noise design constraints.

Due to the limitations of the free vortex method many fans are designed using non-free vortex methods, where the vortex distribution is specified to meet specific design requirements. In a extensive study of axial flow fan litera-

ture Louw (2015) found that non-free vortex designs tend to dominate. Louw (2015) suggests that this is due mainly to a large amount of literature on axial flow fans being devoted to the redesign of non-free vortex fans. Non-free vortex designs are also commonly used when specific constraints apply to the fan being designed. Downie *et al.* (1993) suggest that non-free vortex designs should be used in the following circumstances:

- To meet manufacturing constraints related to injection moulding

- Where a large total-to-total pressure rise is to be achieved in the absence of a stator or diffuser

- Where improved performance is required from a fan through rotor redesign alone

Downie *et al.* (1993) also state that well designed non-free vortex fans are efficient and quiet in operation. Sørensen (2001) demonstrated that the trailing edge noise of an axial flow fan design can be minimised while maintaining efficiency, in part due to the lack of constraints on velocity distributions in the fan as a result of using a non-free vortex design technique. Vad and Bencze (1998) state that non-free vortex design should be used when a high total pressure rise is required from a fan with a low blade number, rotational velocity and hub-to-tip ratio. Non-free vortex design techniques also provide means for hub loss reduction as well as reduced blade twist (Vad and Horváth (2008)). There are indications in literature that high total-to-static efficiencies can be obtained in non-free vortex designs. While Bruneau (1994) used a free vortex design methodology, it was found that an optimum static efficiency was obtained for a swirl distribution that differed slightly from the free vortex assumption. The disadvantage of non-free vortex design is that the flow through the fan will have a radial flow component. According to Vad and Horváth (2008) the radial flow component can increase blade tip losses, even at design flow rate. Vad and Horváth (2008) also found that non-free vortex designs tend to have poorer stall behaviour when compared to free vortex designs.

Several authors present vortex optimisation techniques that aim to maximise fan efficiency while producing realistic designs. These techniques generally result in non-free vortex fan which are capable of attaining high efficiencies, as well as meeting other design criteria, such as reduced blade twist or improved off-design performance. Von Backström *et al.* (1996) developed a vortex design technique that minimises the kinetic energy flux at the fan exit, with a view to improve fan efficiency. A similar method was used by Bamberger and Carolus (2015*a*) in their investigation of achievable total-to-static efficiencies of low pressure rise fans. The method used by Bamberger and Carolus (2015*a*) minimises the exit kinetic energy flux by means of artificial neural networks assuming the swirl distribution of Horlock (1958) whereas the

method of Von Backström *et al.* (1996) directly determines the swirl distribution in the fan using the Sequential Quadratic Programming method of Powell (1978). Bamberger and Carolus (2012) found that in their parameter space maximum total-to-static efficiencies of 68% are realistically achievable for fans with large specific diameters and medium specific speeds, under the conditions prescribed. Von Backström *et al.* (1996) found that their method reduced exit kinetic energy flux by 1.8% compared to the free vortex. It was also found that the method significantly reduced blade twist at the hub, reducing manufacturing costs as well as reducing blade camber. This method was successfully employed by Van der Spuy (1997) in the design of a series of axial flow fans. Sorensen *et al.* (2000) also advocate the use of non-free vortex design methods, as off-design performance of well designed non-free vortex fans is generally better than of free vortex fans. This was demonstrated through the design and optimisation of non-free vortex fans for a high average efficiency over a range of flow rates. According to Sorensen *et al.* (2000) optimum efficiency of non-free vortex fans is strongly dependent on the fan hub-to-tip ratio, with small hubs resulting in unrealistic blading designs at the blade root and large hubs resulting in increased tip losses. A similar dependence of fan performance, especially static efficiency, on hub size is also found by Bamberger and Carolus (2015*b*).

In general, literature indicates that the free vortex is an effective swirl distribution which greatly simplifies the design of an axial flow fan. The free vortex swirl distribution also generally gives good performance with very high static efficiencies possible. The design is however limiting due to excess blade twist at the hub in some cases. There is a an indication that non-free vortex designs can also attain very high efficiencies, provided that the swirl distribution is correctly optimised. Non-free vortex designs can also be designed and optimised to a wider range of operating conditions or design constraints. For both types of swirl distribution literature agrees that the selection of an optimum hub-to-tip ratio for the fan being designed is imperative to ensure high performance.

2.2.2   Fan Blading Design

Once the flow distribution through the fan is known, the blade loading and solidity can be determined. These parameters can be used to calculate the required chord lengths and stagger angles. The blade sections are then stacked to define the fan blade. Although the determination of blade loading and solidity is straight forward, the stacking scheme employed in the design is known to have an influence on fan performance. Traditionally fans are stacked radially, however often sweep can be incorporated into the blading design, as shown in figure 2.2. Blading can also be designed to have a lean component in the upstream or downstream directions. These blading design schemes have been extensively investigated and are worthy of discussion here.
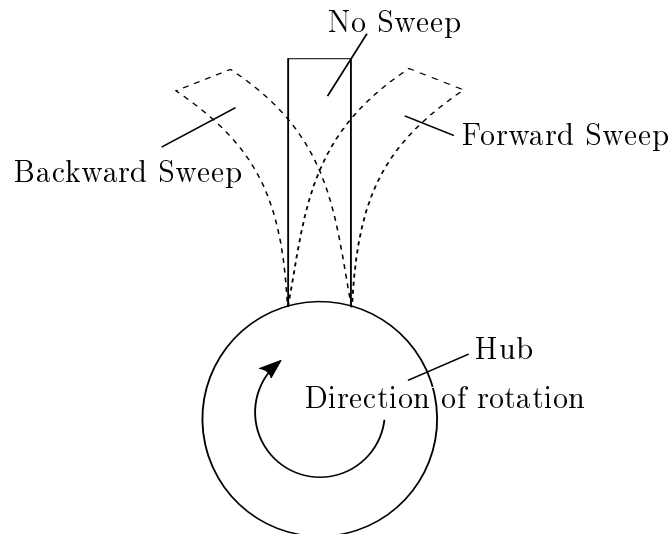
Figure 2.2: Schematic of common non-radial blade stacking schemes

Non-radial blading designs stem from the aircraft industry where sweep and lean have benefits such as drag reduction at higher Mach numbers (Lewis and Hill (1971)). An early study by Lewis and Hill (1971) found that sweep has a profound effect on meridional and blade-to-blade flow. More recently Beiler and Carolus (1999) investigated the effect of various degrees of both forward and backward sweep in low-pressure rise rotor only axial fans of a controlled vortex design. This investigation found that back sweep tends to have a negative impact on fan performance with flow separation occurring at relatively high flow rates, reducing aerodynamic performance and increasing noise levels. Beiler and Carolus (1999) however demonstrate that forward sweep was generally beneficial for the class of fan in question, resulting in better outlet flow distribution, reduced discharge losses and improved acoustic performance. These findings are backed up extensively by literature, with the vast majority of studies focusing on the benefits of forward sweep.

Corsini and Rispoli (2004) found that the stall margin of the fan was improved as sweep counteracted some of the radial flow effects prevalent due to the non-free vortex flow distribution in the fan, preventing the accumulation of low energy fluid near the blade tip, thereby controlling the onset of stall. Similar finds are made by Yang *et al.* (2007), who additionally found that optimising forward sweep resulted in a reduction in noise emissions. Vad (2008) conducted an extensive literature review in order to better understand the benefits of sweep. It was found that forward sweep tends to have efficiency benefits for fans of increased solidity, tip gap, loading and specific performance. Masi and Lazzaretto (2015) shows that backsweep is generally undesirable while forward sweep is of particular benefit in non-free vortex fans with high circulation gradients, improving both pressure and efficiency. Forward seep is also found to improve low flow rate performance for free vortex fans by exten-

ding the stall margin, although performance is reduced at moderate and high flow rates. Masi and Lazzaretto (2015) also finds sweep to be of little benefit for non-free vortex fans with moderate circulation gradients.

Based on these findings the following conclusions can be drawn:

- Backsweep is undesirable in rotor only axial flow fans, as it results in performance losses across the entire fan operating range.

- Forward sweep tends to have positive benefits, particularly for non-free vortex fans with high circulation gradients. These benefits include a reduction in tip losses and noise as well as potential gains in efficiency, dependent on fan parameters such as solidity and loading as well as the suitability of the non-radial stacking blading design procedure used.

- Literature indicates that forward sweep can be used to extend the stall free operating range in both free vortex and non-free vortex fans. In some cases this is associated with a steeper fan pressure characteristic.

2.2.3 Aerofoil Selection

In order to design a fan for maximum efficiency, whilst maintaining a reasonable operating range, special attention needs to be paid to the selection of aerofoil sections to be used in the fan blading. Traditionally aerofoil selection was a design decision based on the designer's knowledge of aerofoil physics, available aerofoil data and fan design specifications in question. More recently the rise of numerical modelling methods for aerofoils as well as various optimisation methods have given designers more freedom to develop and optimise aerofoils for the application at hand.

Wallis (1983) defines an aerofoil as a two dimensional lifting surface with a lift to profile drag ratio of ten or more. Flow over an aerofoil has to travel a greater distance over the upper surface than the lower surface. In order to satisfy continuity the flow over the upper surface has to travel at a greater velocity than the flow over the lower surface. This difference in velocities results in increased static pressure on the lower surface and decreased static pressure on the upper surface resulting in a net lifting force, acting perpendicular to the relative flow direction across the aerofoil. Drag is primarily a result of skin friction, pressure forces and secondary effects such as trailing edge vortex shedding (Wallis (1983)). The net drag force acts parallel to the relative flow direction as shown in figure 2.3. In axial flow fan applications the lift force is responsible for providing the flow deflection which creates a static pressure rise across the fan blading, as well as being the main contributor to fan power consumption. The drag force is considered a loss term, reducing flow deflection and contributing to fan power consumption. In the interests of efficiency it is thus desirable to select aerofoils with good lift to drag characteristics.
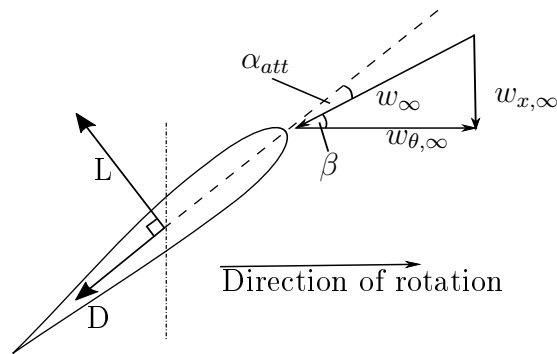
Figure 2.3: Depiction of fan blade element with relevant force components

Lift and drag are both functions of angle of attack, which is defined as the angle between the aerofoil chord line and the mean relative velocity vector w_∞ (figure 2.3). In the context of an axial flow fan w_∞ is comprised out of axial and tangential mean relative velocity components, $w_{x,\infty}$ and $w_{\theta,\infty}$. The axial component is equivalent to the mean absolute axial velocity through the fan at a given radius and the tangential component is defined as the mean absolute tangential velocity component subtracted from the fan blade speed at a given radius. Lift increases with increasing angle of attack up to the point where flow separates off the upper surface of the aerofoil, resulting in a large and sudden drop in lift and an increase in drag. This phenomenon is known as stall and is depicted in figure 2.4. In axial flow fans fan blade speed and thus mean relative tangential velocity, increases with increasing radius. Decreasing flow rate through a fan decreases $w_{x,\infty}$, increasing angle of attack. As the blade speed and therefore $w_{\theta,\infty}$, is lowest, stall tends to occur first at the hub, propagating radially with deceasing flow rate. Stall in fans results in large aerodynamic losses, reducing fan performance. It is thus important to pay careful attention to aerofoil selection in order to ensure satisfactory stall properties as well as good pressure and efficiency characteristics (Wallis (1983))

The fan design methods presented by Wallis (1983) place special emphasis on aerofoil selection. Wallis (1983) states that any aerofoil section for which aerofoil polar data is available can be used in fan design, however in order to achieve an accurate design it is recommended that aerofoil sections with experimentally established performance characteristics are selected. Wallis (1983) advocates the use of F-series aerofoils, a modified version of the C-4 aerofoil section for general fan blading design. This series allows for the incorporation of nose droop, a small amount of local camber near the leading edge which according to Wallis (1983), improves the fan's stall free operating range as well as the maximum amount of lift produced. This approach was used with some success by Van der Spuy (1997), however he indicates that the additional nose droop creates some issues with negative angles of attack near the blade tip. Bruneau (1994) made use of the Clark-Y and NASA LS aerofoil
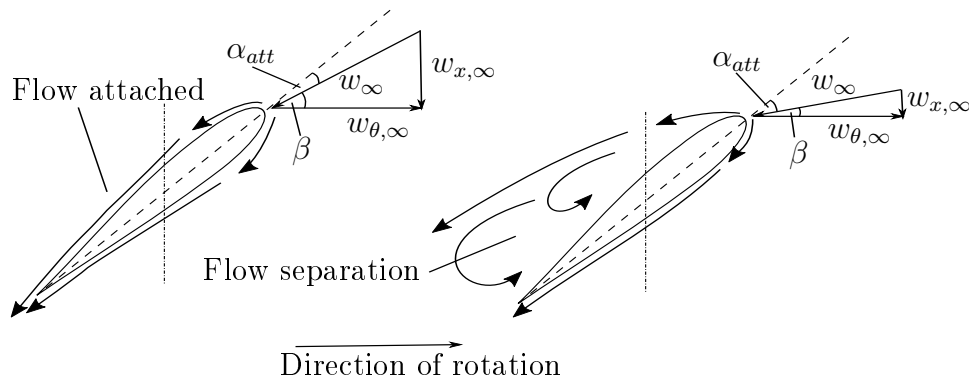
Figure 2.4: Depiction of fan blade element under normal operating conditions (L) and under stall conditions (R)

sections in the development of the B1 and B2 fans. Bruneau (1994) found that the B1 fan with the flat bottomed Clark-Y aerofoil section performed slightly better than the B2 design with the circular arc NASA LS section.

More recently numerical aerofoil modelling techniques such as XFOIL (Drela (1989)) and computational fluid dynamics (CFD) have reduced the reliance on experimental aerofoil data. Additionally these numerical methods have allowed designers to develop and optimise aerofoil profiles specifically for turbo-machinary applications. XFOIL is a boundary layer and potential flow solver that makes use of a panel method to provide polar and pressure distribution predictions for aerofoils. Additionally XFOIL also incorporates design tools for the design and manipulation of aerofoil sections (Drela (1989)). Several authors have shown XFOIL to provide accurate aerofoil polars, provided that the settings are correct and that high quality aerofoil coordinates are provided (Carolus and Starzmann (2011a), Van der Spuy (2011)). Cencelli (2006) successfully used XFOIL to design and model a series of aerofoil sections for use in a small scale wind turbine by blending base aerofoil profiles in order to generate new profiles. Cencelli (2006) concedes that the Geometry Design Routine (GDES) in XFOIl would have allowed more freedom than the blending of base profile, however it was found the the GDES functions could lead to stability issues when setting up a robust optimisation procedure. Wessels et $al.$ (2012) developed a scheme to describe aerofoils by means of non-uniform rational B-splines (NURBS) in order to efficiently parametrise aerofoil sections for optimisation purposes. A thickness-camber and top and bottom NURBS representation schemes were developed and evaluated. Wessels et $al.$ (2012) found that the top and bottom scheme was more accurate, however the thickness-camber scheme is less numerically intensive. In both cases XFOIL was found to give accurate results up to the stall point. It was found that the thickness-camber NURBS scheme could completely represent an aerofoil using only 13 variables. Lee et $al.$ (2008) made use of Bezier curves in order to describe the aerofoil sections of a low speed axial flow fan. The control points of the Bezier

curves were used as variables in an optimisation procedure which made use of CFD analysis in order to optimise the efficiency of an axial flow fan. Lee *et al.* (2008) found that using two variables the thickness and location of maximum thickness of an aerofoil section could be described. These parameters were optimised resulting in a 1.5% improvement in fan total-to-total efficiency.

In Summary:

- Aerofoil selection is key to ensuring efficient and stall free fan operation over the desired operating range. High quality aerofoil polar data aides the designer in achieving this.

- Aerofoil optimisation and modification can provide an effective means of improving fan performance. Factors such as nose droop and thickness distribution have been shown to have an impact on fan performance characteristics such as total-to-total efficiency.

- Several strategies for the parameterisation and design of aerofoils do exist, these include XFOIL's GDES and aerofoil blending options as well as more advanced techniques such as the use of NURBS and Bezier curves. In strategies that incorporate optimisation it is desirable to reduce the number of variables used to describe the aerofoil.

2.2.4   Tip Clearance Effects

The clearance between the blade tip and duct in an axial flow fan has a significant impact on the performance of the fan. These effects have been widely studied from both a fan performance and noise perspective. The basic mechanism behind the effect is well understood. Simplistically, flow is drawn through the tip gap from the high pressure outlet side of the blade to the low pressure inlet side.

Venter and Kröger (1992) found through experimental testing that a reduction in tip gap leads to improved fan static pressure, power and static efficiency characteristics. Based on these results an empirical correlation for performance loss and tip clearance was developed. Wilkinson and Van der Spuy (2015) made similar finds on a different design of fan that was developed to the same operating point as the fan used by Venter and Kröger (1992) and tested on the same test facility. Wilkinson and Van der Spuy (2015) applied the same technique as Venter and Kröger (1992) in order to develop an empirical correlation for performance loss and tip clearance, however a comparison between the two results sets shows that the correlations obtained are different indicating that tip effects are design dependent. Fukano *et al.* (1986) also found that a reduction in tip clearance led to an improvement in fan performance as well as a reduction in fan noise.

All studies agree that tip clearance should be minimised as far as possible in order to maximise the performance of an axial flow fan. Literature however

presents little to no evidence of a reliable method of taking tip effects into account at the design stage. However according to Wallis (1983), provided that the tip gap is 1% or less of the blade height, no adjustments are necessary.

2.2.5 Performance Enhancing Modifications

In order to overcome specific problems encountered in axial flow fans several authors have proposed making performance enhancing modifications to axial flow fans. These modifications aim to address specific issues such as stall, noise emissions or leakage flow. A brief overview of modifications potentially relevant to this study is provided below.

In many designs of axial flow fan, such as the V-fan of Venter (1990) the fan blades do not seal to the fan hub. This is often for manufacturing or installation reasons. Venter (1990) found through experimental analysis of the velocity profiles downstream of the fan that severe reversed flow occurred in the root gap region. This lead to a reduction in fan total-to-static pressure rise and efficiency, especially at low flow rates. Venter (1990) proposed fitting a solid 2 mm mild steel disk on the downstream side of the fan in order to alleviate this problem. It was found that this improved the fan total-to-static pressure and efficiency characteristics of the V-fan, especially at low flow rates.

When designing the B-fan Bruneau (1994) placed special emphasis on the configuration of the hub, based on the findings of Venter (1990) . The B-fan hub extends almost to the blade root, with a small clearance left to allow for blade angle adjustment. The hub also extends along the full length of the blade in the axial direction. Bruneau (1994) found that by inserting a wooden seal between the blade root and hub, the performance of the fan in terms of static pressure rise and efficiency could be significantly improved.

Modifications to the blade tip have been proposed by several authors in order to reduce tip leakage losses or the noise emissions associated with the flow structure in the tip region. Corsini et al. investigated the use of blade tip end plates in order to control tip leakage and the vortex structures that result from this phenomenon (Corsini *et al.* (2007), Corsini *et al.* (2010), Corsini *et al.* (2013)). The overall aim of this work was to reduce the noise emissions that result from the blade tip vortex structures which result from tip leakage flow. Several concept endplates have been developed with varying geometries, however in all cases the endplates were found to improve fan performance slightly, by reducing tip gap losses thereby improving fan efficiency. A more simplistic study by Wilkinson and Van der Spuy (2015) found that basic square endplates could improve the performance of fans with large tip gaps, however not to the same extent as minimising the tip gap.

2.3   Fan Numerical Modelling

Numerical modelling is commonly used in fan design as it can provide performance and flow field data that can aid the designer, without having to construct prototype fans. Generally two types of fan computational fluid dynamics (CFD) models exist, three dimensional models which solve the flow around the fan blades and simplified numerical models, such as the actuator disk model, which approximate the influence of a fan on the flow field. These models are discussed in further detail below with reference to accuracy of flow field and performance prediction as well as ease of implementation. This section will be used to asses which models are most appropriate to this study.

2.3.1   Three Dimensional Modelling

Three dimensional numerical models of axial flow fans are commonly implemented in CFD in order to gain insight into the flow around fan blading that cannot be obtained experimentally. These models can also be used for detailed performance analysis of existing or prototype fans. Almost all studies considered in this thesis model only a single fan blade with periodic boundary conditions. Only the study of Liu *et al.* (2010) models the fan with all blades present. Most studies also model the blade in a simple annular duct with specified inlet and outlet conditions to replicate the conditions the fan would operate under. Notable exceptions are the works of Augustyn *et al.* (2016) and Louw (2015) who model axial flow fans in a domain designed to replicate a BS 848 (ISO 5801) type A test facility. The rationale behind simplifications such as periodic models and simple annular geometries relates to the computational requirements of three dimensional fan models.

Out of twenty two papers surveyed in this study sixteen made use of one or other variant of the $k-\epsilon$ turbulence model of Launder and Spalding (1974). Three make use of the SST model of Menter (1993), two make use of the Sparlat Allmaras model (Spalart and Allmaras (1992)) and one makes use of the $k-\omega$ model. The $k-\epsilon$ model is commonly selected as it is relatively computationally inexpensive and results in a fair correlation with experimental data. More recently trends have seen a move towards non-linear versions of the standard $k-\epsilon$ model, such as the Cubic $k-\epsilon$ of Lien and Leschziner (1994) and the Realizable $k-\epsilon$ model of Shih *et al.* (1995), which are better suited to the flow conditions encountered in turbomachinery. Louw (2015) tested three different turbulence models, the transitional SST model, the $k-kl-\omega$ model and the Realizable $k-\epsilon$ model. According to Louw (2015), the Realizable $k-\epsilon$ model gave a good comparison with experimental data and required the least computational effort.

2.3.2 The Actuator Disk Model

Owing to the computational expense involved in three dimensional fan modelling several simplified fan models have been developed. These models aim to replicate the effect of an axial flow fan on a flow field without explicitly modelling the fan blading, thereby reducing computational expense. This is of particular interest when simulating a fan, or array of fans in a system such as a heat exchanger where the computational expense of three dimensional modelling is prohibitive.

The actuator disk model (ADM) and its variants provide a simplified axial fan model which avoids some of the shortcomings of the pressure jump model, which is unable to predict the tangential flow component downstream of the fan. Originally developed by Thiart and Von Backström (1993) and based on the work of Pericleous *et al.* (1987), the ADM models a fan as a plane of cells at which momentum source terms are introduced. Momentum source terms are calculated using two dimensional blade element theory, based on the spanwise lift and drag distribution, blade chord length and rotational speed. This allows for the ADM to take into account inlet flow distortions as well as predict the swirl velocity component downstream of the fan. The ADM can therefore model both the pressure rise of the fan as well as the flow field in the vicinity of the fan blading with reasonable accuracy, as demonstrated by Thiart and Von Backström (1993) and Meyer and Kröger (2001). The use of lift and drag data also make it possible to estimate fan power consumption and efficiency based on specific inlet flow conditions (Thiart and Von Backström (1993)).

The ADM has been used to model arrays of fans in large cooling systems with some success as demonstrated by Meyer (2005) and Bredell *et al.* (2006). A version of the ADM has been used in the design of axial fans, as described by Bonanni *et al.* (2016). The main limitation of the ADM is that it tends to under predict fan performance at low flow rates (Louw (2015),Van der Spuy (2011), Wilkinson *et al.* (2016)). According to Meyer and Kröger (2001) this is due to increased radial flow occurring at low flow rates, which the ADM cannot account for. In order overcome this two different approaches have been proposed, namely the extended actuator disk model (EADM) and the reverse engineered empirical actuator disk model (REEADM). The EADM of Van der Spuy (2011) extends the linear region of the aerofoil lift curve at low flow rates, based on the model of Gur and Rosen (2005). The rationale behind the EADM stems from the work of Himmelskamp (1947) who measured high lift coefficients at low flow rates during a study of the aerofoil properties of rotating airscrews, which is attributed to boundary layer stabilisation due to radial flow. The REEADM of Louw (2015) aims to correct for radial flow by incorporating a radial momentum source term derived from a detailed three dimensional numerical study of the relevant axial flow fan into the ADM. Wilkinson *et al.* (2016) compared the ADM EADM and REEAM and found

that the EADM does improve performance at low flow rates, however it tends to over predict pressure rise and power consumption. The REEADM was found to perform slightly better at low flow rates than the ADM, however not significantly enough to justify the effort of the three dimensional simulations. Of the literature surveyed, all studies make use of the $k - \epsilon$ model of Launder and Spalding (1974).

While unable to accurately model fan performance at low flow rates, the ADM gives accurate predictions of the flow field in the vicinity of the fan as well as being sensitive to inlet distortions. This makes the ADM suitable in applications where the flow field in the vicinity of the fan is of interest, such as in the design of axial flow fans.

2.4 Concluding Remarks

A broad overview of literature pertinent to this study has been provided, discussing in detail aspects such as the unique flow conditions found in forced draft air-cooled heat exchangers and aspects of fan design. The findings of the literature survey are summarised below, with the intention of linking common themes as well as setting out the direction this study will take.

The operating conditions which axial flow fans are subjected to in air-cooled heat exchangers have been thoroughly studied and understood. Cross flow effects such as wind or induced flow patterns caused by the sheer number of fans in a system can have a detrimental effect on fan performance, reducing the flow rate through the fans near the edges. In order to overcome this literature suggests that fan design parameters such as hub-to-tip ratio and solidity have a profound effect on the fan performance loss experienced under these conditions. Several authors show that fans with optimised hub-to-tip ratios result in improved performance. It is also understood that fans with steep static pressure to volume flow characteristics perform better under distorted flow conditions. There is some indication from literature that depending on the severity of the cross flow conditions fan or blade stall may occur.

In order to mitigate these effects several options are considered in terms of fan design. Vortex design is the starting point of any fan design process and highly important to ensure good fan performance. A significant amount of literature strongly advocates the use of non-free vortex design methods. Indications are that non-free vortex designs are not constrained to one specific flow condition and thus the flow field can be better optimised to suit the desired fan application. Non-free vortex designs are able to better control physical parameters such as blade twist, which can be very high in free vortex designs. Reduced blade twist is desirable in this study as excessive twist can lead to stall at the blade root. In both cases the importance of hub-to-tip ratio selection is highlighted as being key to a good design. Aerofoil selection is also shown to be an important consideration in the design of fan blading.

Traditionally designers have been limited by the need for experimental aerofoil data. However more recently numerical tools have allowed for the design and optimisation of aerofoil sections for turbomachinary applications. These tools have also resulted in the possibility of optimising aerofoil sections along the blade span. Increasing tip clearance is also shown to lead to a loss in fan performance, which may be more severe in non-free vortex designs owing to the occurrence of radial flow. Non-radial blading design is also considered, however literature indicates that this is most beneficial for non-free vortex fans with high circulation gradients and will thus only be considered if necessary. A number of fan modifications are also considered such as root seals and end plates.

A brief survey of numerical modelling provides an overview of the effectiveness of three dimensional numerical modelling as well as preferred turbulence models. Three dimensional models generally give highly accurate results which match well with experimental data. This means of modelling provides a method to validate a fan design. Simplified numerical models are shown to be far less computationally expensive than three dimensional models. The actuator disk model provide a means of reasonably accurately modelling the flow field in the vicinity of fan blading.

With above in mind the following design and modelling approach is adopted:

1. The use of a non-free vortex design method in order to reduce blade twist at the blade root, whilst maximising fan efficiency. This aims to improve the stall margin of the fan which should improve off design performance.

2. The optimisation of the fan hub-to-tip ratio in order to improve efficiency as well as make the design more tolerant of the operating conditions encountered in air-cooled heat exchangers.

3. Aerofoil optimisation should be considered in order to improve stall margin as far as possible.

4. The development of an actuator disk model capable of modelling the fan based on design data.

5. The three dimensional modelling of the axial flow fan designed in this study in order to accurately model its performance and the flow field around the blades at a number of flow rates.

Chapter 3

Fan Design

A fan design method is developed and presented in order to meet the aims of this study. The method aims to be rational, robust and capable of designing a fan to meet a given set of specifications. In order to demonstrate this, a set of specifications is presented, followed by the design techniques used in this study. Finally a brief overview of the final fan design, to be analysed numerically, is presented.

3.1 Design Procedure Overview
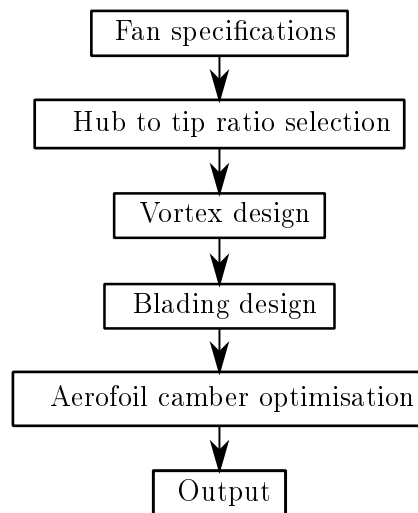
Figure 3.1: Overview of fan design procedure

The fan design procedure follows the process indicated in figure 3.1. The method is developed in a stepwise manner in order to ensure the validity of each calculation step. There is however scope to combine certain steps, such as blading design and camber optimisation, in the future. The procedure

presented here is loosely based on the works of Bruneau (1994) and Van der Spuy (1997) and serves as a further development of these design methods. An overview of Bruneau's design method is provided in Appendix B. Appendix C details the concept design procedure that aided in the development of the method presented here. The layout of this chapter follows the design procedure shown in figure 3.1, first the design specifications are detailed, followed by the the various design steps, then the final design is presented.

The design procedure is implemented by means of a PYTHON script (Van Rossum and Drake (2010)), which makes use of XFOIL (Drela and Youngren (2001)), for aerofoil modification and polar prediction, as well as van der Plaats Research and Development DOT software (Vanderplaats Research & Development Inc (2001)) which provides a suit of numerical optimisation tools. The final output of the PYTHON script is a text file containing key parameters such as rotor outlet flow distribution, chord and blade twist distributions as well as coordinate files that can be used to define the fan blade in a CAD program.

3.2   Design Specifications

The design specifications presented in here are for a 24 ft fan that is intended for use in a forced draft air-cooled heat exchanger in the power generation industry, as part of the MinWaterCSP project (MinWaterCSP (2017)). These specifications provide a performance target that is comparable to other fans of this type currently used in this application. The specifications are presented in table 3.1.

<div align="center">

Table 3.1: Fan Specifications

Diameter	24 ft [7.3152 m]
Flow rate	333 m^3/s
Fan total-to-static pressure	116.7 Pa
Blade tip speed	58 m/s
Inlet air temperature	20 °C
Relative humidity	65%
Atmospheric pressure	101 325 Pa

</div>

The fan is to be of rotor only configuration with blades that are radially stacked. It should also be noted that the blade tip speed value is a maximum value and lower blade tip speeds are permissible as this will result in a reduction in fan noise. The fan should be designed for a total-to-static efficiency at the design point of $\approx 60\%$ or higher. A hub plate and root seals may be included in the design in order to prevent back flow through the fan, and thus improve

performance. The fan will be installed in the configuration shown in figure 3.2.
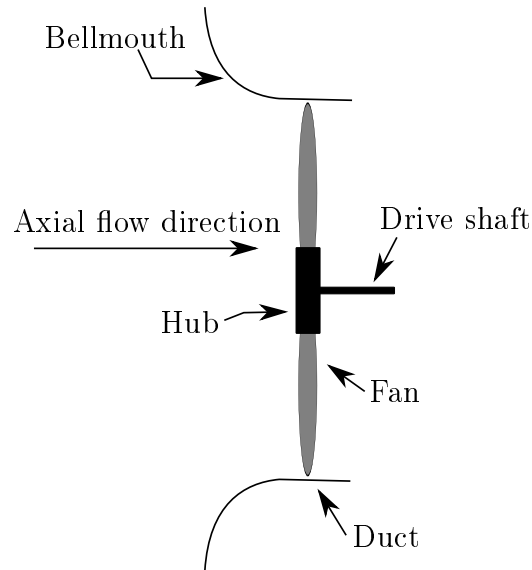
Figure 3.2: Fan configuration

Another important design consideration is the tip gap. Tip gap is well known to have a detrimental effect on fan performance as demonstrated by Wilkinson and Van der Spuy (2015) and Venter and Kröger (1992). The specification provided is that the tip gap should have a value of $s/d_F = 0.004$ at any point within the shroud. This value should however be considered a maximum and can be reduced if needed.

Following consultation with NOTUS Fan Engineering, the following manufacturing constraints are also specified:

- Linear or near linear leading edge

- Linear or near linear trailing edge

- Linear thickness distribution

- Stacking point must be situated at the thickest part of the aerofoil cross section

- The axial length of the fan may not exceed 1 m and should be minimised as far as reasonably possible

The first three constraints ensure that the fan blades designed will be easy to remove from their moulds, should they be manufactured using composite materials. The fourth constraint ensures that enough structural support can be built into the blades. This support will enhance the stiffness of the blades making them less likely to fail in operation. The final constraint ensures

that the length of the duct is reasonable from a manufacturing and assembly perspective.

Aside from the above mentioned constraints the structural design and manufacture of the fan is beyond the scope of this study.

3.3   Definition of Variables

At this point it is important to clearly define the main performance variables used in this study, namely:

- Fan total-to-static pressure

- Fan power

- Fan total-to-static efficiency

These three variables can be plotted as a function of volume flow rate in order to give an indication of fan performance. The definitions that follow are based on the definitions described in British Standard 848 Part 1 (2007). Fan total-to-static pressure, also referred to as fan static pressure is defined as the difference between the total pressure directly upstream of the fan and the static pressure directly downstream of the fan, as shown in equation 3.3.1.

$$\Delta p_{ts} = p_{t_1} - p_{s_2} \quad [Pa] \tag{3.3.1}$$

Fan power is defined as follows:

$$P = T_{shaft}\omega_F \quad [W] \tag{3.3.2}$$

Finally fan total-to-static efficiency is defined as:

$$\eta_{ts} = \frac{\dot{V}\Delta p_{ts}}{P} \quad [\,] \tag{3.3.3}$$

where $\dot{V}$ is the volume flow rate in m^3/s that corresponds with the power and pressure values.

3.4   Hub-to-tip Ratio Selection

The first major design decision made when designing an axial flow fan is the selection of the hub-to-tip ratio. It is well known that selecting the optimum hub to tip ratio is a major factor in designing an efficient fan. Van Niekerk (1958) developed an optimisation technique for optimising the design of axial flow fans with inlet guide vanes and flow straighteners. This technique was adapted by Bruneau (1994) to be used for fans of a rotor only configuration

and used successfully in the design of the B fans. The technique assumes free vortex flow distribution through the fan and that solidity is low enough at every point in the blading so that isolated aerofoil theory can be used. According to Bruneau (1994) isolated aerofoil data can be used when fan solidity is below 0.7. The accuracy of the isolated aerofoil approach tends to deteriorate at higher solidities. It is also noted that Van Niekerk (1958) suggests that the method can be extended to non free vortex fans, as in this case, and fans with higher solidities. The method presented allows for the hub-to-tip ratio to be selected, while accounting for losses due to friction at the walls of the fan annulus as well as aerofoil profile losses.

The following equations for fan total-to-total and total-to-static efficiency are derived by Bruneau (1994), based on the work of Van Niekerk (1958):

$$
\begin{aligned}
(1 - \eta_{tt}) = &\frac{2(\tan\gamma)_{avg}(1 - x_h^3)}{3\phi_{tip}(1 - x_h^2)} + \frac{2(\tan\gamma)_{avg}(\phi_{tip} - \epsilon_h x_h)}{1 + x_h} \\
&+ (1 - \eta_{ann})\frac{\phi_t}{2\epsilon_h x_h}
\end{aligned}
\tag{3.4.1}
$$

$$
(1 - \eta_{ts}) = (1 - \eta_{tt}) + \frac{\phi_{tip}}{2\epsilon_h x_h}\left[1 - 2(\epsilon_h x_h)^2\frac{\ln(x_h)}{1 - x_h^2}\right]
\tag{3.4.2}
$$

where $\tan\gamma$ is the average lift to drag ratio and η_{ann} is the annulus efficiency. As these values are unknown at this stage of the design process it is necessary to assume values. The assumed values are:

$$
\tan\gamma = 0.0167
\tag{3.4.3}
$$

and

$$
\eta_{ann} = 0.8
\tag{3.4.4}
$$

According to Van Niekerk (1958) these values are conservative and reasonable. The tip flow coefficient and hub swirl factor are given by equations 3.4.5 and 3.4.6.

$$
\phi_{tip} = \frac{c_{x_{2tip}}}{\omega_F r}
\tag{3.4.5}
$$

$$
\epsilon_h = \frac{c_{\theta_h}}{c_{x_2}}
\tag{3.4.6}
$$

where

$$
c_{x_2} = \frac{\dot{V}}{\pi\left(\left(\frac{r_F}{2}\right)^2 - \left(\frac{x_h r_F}{2}\right)^2\right)}
\tag{3.4.7}
$$

The value of ϵ_h is limited to a maximum of 1.1 based on the recommendations of Wallis (1983), in order to prevent excessive flow turning at the hub. As the

tip flow factor is constant for a specific hub-to-tip ratio, considering equations
3.4.1 and 3.4.2 it is clear that efficiency will be maximised when ϵ_h is set to
the maximum value. Therefore fan total-to-total and total-to-static efficiencies
are calculated for the range of hub-to-tip ratios under consideration, with ϵ_h
set to 1.1. Considering equations 3.4.6 and 3.4.7, it is clear that the absolute
hub swirl velocity (c_{θ_h}) is a function of hub-to-tip ratio. With this in mind
Bruneau (1994) provides the following equation to calculate the theoretical
total-to-total pressure rise:

$$\Delta p_{tt,th} = \rho_a \omega_F r_h c_{\theta_h} \tag{3.4.8}$$

The actual total-to-static pressure rise can then be obtained using the total-to-
static efficiency for the same hub-to-tip ratio calculated using equation 3.4.2:

$$\Delta p_{ts} = \Delta p_{tt,th} \eta_{ts} \tag{3.4.9}$$

Using equations 3.4.1, 3.4.2, 3.4.8 and 3.4.9 the total-to-static pressure rise
which corresponds to the maximum total-to-static efficiency can be calculated
for a given hub-to-tip ratio, under the prescribed conditions at the design flow
rate. The optimum hub-to-tip ratio will result in a total-to-static pressure rise
equal to that given in the design specifications (table 3.1).

3.5 Vortex Design

The vortex design method used in this study is based on the work of Von Back-
ström *et al.* (1996). This method, like the free vortex, assumes that flow across
the blade section is purely two dimensional as shown in figure 3.3 and aims to
optimise the outlet velocity profile in such a way as to minimise kinetic energy
flux at the fan exit. According to Von Backström *et al.* (1996) the minimi-
sation of exit kinetic energy flux should result in improved fan total-to-static
efficiency. This work was used by Van der Spuy (1997) to design a series of
low noise rotor-only axial flow fans. Both Van der Spuy (1997) and Von Back-
ström *et al.* (1996) found that the method tends to reduce blade twist when
compared to a free vortex based scheme. This has benefits in terms of sim-
plifying manufacturing as well as reducing blade angle at the hub, improving
stall margin.

   The assumptions made in this study are identical to those of Von Backström
et al. (1996), namely:

1. Uniform total pressure across the inlet cross section

2. Euler turbomachinery equation for incompressible flow is applicable

3. Simple radial equilibrium applies, therefore the flow has no radial com-
   ponent at the planes of interest (directly upstream and downstream of
   the rotor)
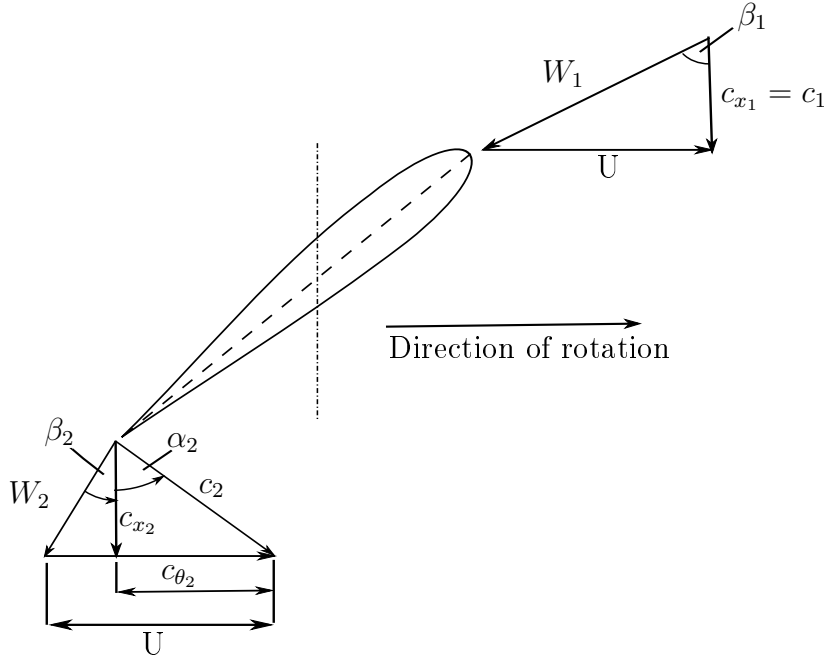
Figure 3.3: Velocity diagram for a rotor only fan blade

4. Flow is assumed to be incompressible, inviscid and loss free

Inputs to the procedure are the fan specifications and hub-to-tip ratio. For simplicity the fan volume flow rate and static pressure rise specifications are non-dimensionalised. The flow coefficient is calculated as follows.

$$\phi = \frac{c_{z,avg}}{U_c} \tag{3.5.1}$$

where

$$c_{z,avg} = \frac{\dot{V}}{A_f} \tag{3.5.2}$$

The static pressure coefficient is given by:

$$\psi_{ts} = \frac{p_{ts}}{0.5\rho_a U_c^2} \tag{3.5.3}$$

The optimisation process makes use of the total pressure coefficient, therefore it is necessary to convert the static pressure coefficient to a total pressure coefficient. This can be done using a relationship described by Von Backström *et al.* (2000), the equations required are listed below.

$$\psi = \frac{1 - \sqrt{1 - 4F_v(\psi_{ts} + \phi^2)}}{2F_v} \tag{3.5.4}$$

where

$$F_v = \frac{0.5 ln(x_h)}{x_h^2 - 1} \tag{3.5.5}$$

The calculation scheme is subject to three constraints in order to ensure that the designed flow field is viable (Von Backström *et al.* (1996)). Firstly $\psi < 2.2x_h\phi$ ensures that back flow does not occur at the hub. The constraint prevents back flow by limiting the absolute exit flow angle (α_2) to approximately 50 degrees. The second constraint $\psi < 2x_h\phi$ is referred to as the cascade limitation. This constraint arises as the maximum flow deflection in a blade cascade limits the static pressure rise that can be obtained from a certain number of blades. The constraint limits the absolute exit flow angle to approximately 45 degrees and thus overrides the first constraint as it is more stringent. The final limitation $\psi < 2x_h^2$ ensures that the fan rotor does not turn flow beyond the axial direction, effectively limiting the relative exit flow angle (β_2) to 0 degrees. As ϕ is a function of fixed design variables as shown in equation 3.5.1 it cannot be changed to ensure that limitations are met. It is apparent from equation 3.5.4 that the only parameter that can be adjusted to ensure design limitations are met is the-hub to-tip ratio. It should be noted that the hub to tip ratio cannot exceed unity and that a small hub is desirable.

Once a hub-to-tip ratio has been selected that fulfils the design limitations, the minimisation of kinetic energy flux can be carried out. The kinetic energy flux at the fan outlet is given by the following expression:

$$L = \pi\rho_a \int_{r_i}^{r_o} r c_{x_2}(c_{x_2}^2 + c_{\theta_2}^2)dr \tag{3.5.6}$$

In order to simplify equation 3.5.6 for ease of optimisation, the following non-dimensional substitutions are used:

$$t = \frac{r}{r_i} \tag{3.5.7}$$

$$a = \frac{r_o}{r_i} \tag{3.5.8}$$

$$u(t) = \frac{c_{\theta_2}(r_i t)}{r_i \omega_F} \tag{3.5.9}$$

$$v(t) = \frac{c_{x_2}(r_i t)}{r_i \omega_F} \tag{3.5.10}$$

Substitution of the non-dimensional terms shown above into equation 3.5.6 allows the minimisation problem to be formed as follows:
Find $u(t), v(t)$ where $t \in [1, a]$ in order to minimise

$$\int_1^a v(v^2 + u^2)t\,dt = F = \frac{L}{\pi\rho r_1^5 \omega_F^3} \tag{3.5.11}$$

The minimisation is subjected to the following constraints:

$$t\frac{du}{dt} + u = \frac{u^2}{t} + u\frac{du}{dt} + v\frac{dv}{dt} \tag{3.5.12}$$

$$\int_1^a t^2 uv dt = A = \frac{P}{2\pi\rho r_i^5 \omega_F^3} \tag{3.5.13}$$

$$\int_1^a tv dt = B = \frac{\dot{m}}{2\pi\rho r_i^3 \omega_F} \tag{3.5.14}$$

The constraints ensure that the optimised velocity profiles fulfil radial equilibrium (equation 3.5.12) as well as dimensionless work rate and dimensionless flow rate limitations as shown in equations 3.5.13 and 3.5.14 respectively. The values for A, B and a are calculated as follows:

$$a = \frac{1}{x_h} \tag{3.5.15}$$

$$A = \frac{\psi\phi(1 - x_h^2)}{4x_h^5} \tag{3.5.16}$$

$$B = \frac{\phi(1 - x_h)}{2x_h^3} \tag{3.5.17}$$

The minimisation process is carried out using Vanderplaats Research and Development DOT software. The software is directly called from the python script and makes of the Sequential Quadratic Programming (SQP) method of Powell (1978) with modifications based on the work of Vanderplaats and Sugimoto (1985). The studies of both Von Backström *et al.* (1996) and Van der Spuy (1997) also make use of the SQP optimisation algorithm. The SQP method is considered to be highly efficient for minimising highly constrained functions. It is also considered to be theoretically best, provided the optimisation problem is well conditioned. In order to solve the optimisation problem, the blade span needs to be divided into a number of discrete intervals as analytical solutions for the differential equation are not readily available. Discretisation allows for the problem to be solved using numerical techniques, greatly simplifying the optimisation process. The optimisation technique, including numerical methods used, is discussed in further detail in Appendix A.

The results of the optimisation process are the non-dimensional axial and swirl velocity distributions $v(t)$ and $u(t)$, where t is dimensionless radius. These parameters can easily be reverted into physical values for swirl and axial fan outlet velocities.

$$c_{x_2}(r) = v(t)r_i\omega_F \tag{3.5.18}$$

$$c_{\theta_2}(r) = u(t)r_i\omega_F \tag{3.5.19}$$

The remaining terms shown in figure 3.3 can now be calculated using equations B.1.11 to B.1.17 in Appendix B. Further it is also possible to calculate an estimate of fan power using equations B.1.20 to B.1.22 in Appendix B. The power estimate provides the designer with a value that is important when

assessing design quality as well as an indication of motor power that will be required to drive the fan.

Once the vortex design process is complete the key parameters are passed on to another PYTHON script which designs the fan blades. Other data from the vortex design process, such as the exit velocity profiles and power estimate are direct outputs of the overall design procedure and are saved to an output file.

3.6 Blading Design

The blading design technique used in this study is largely based on the work of Wallis (1983) which formed the backbone of the blading design methodologies of Van der Spuy (1997) and Bruneau (1994). The method however differs from previous work as an optimiser is integrated into the blade design process in order to produce better blading and to allow the designer to incorporate design constraints into the process more easily. The technique is once again implemented by means of a PYTHON script and the optimisation conducted using van der Plaats R&D DOT software that is called by the PYTHON script.

The inputs to the procedure are the design specifications as well as all data generated by previous calculations. These are listed below:

- Fan design specifications

- Hub-to-tip ratio

- Velocity triangle data generated by the vortex design procedure (as shown in figure 3.3)

- A reasonable range of C_L values, in this case 1.1 to 0.3

- A base aerofoil profile

The blading design procedure consists of two optimisation steps, firstly the chord length is optimised and secondly the aerofoil profile camber distribution is optimised. An estimate of the fans performance in terms of static efficiency as well as calculating all key physical specifications is also provide at this stage. These terms, as well as coordinate files that allow a 3D model of the fan to be generated, are the outputs of the procedure.

3.6.1 Blading Design - Chord length distribution

The first step of the blade design process is to determine the chord length distribution and other parameters such as the Reynolds number distribution. For this phase a reference aerofoil is used, in this case the NASA LS 0413 using the lift drag data of McGhee and Beasley (1976). The blading design

technique is based on the work of Wallis (1983). Bruneau (1994) used a similar approach when designing the B fans, showing that the techniques developed by Wallis (1983) are appropriate for the design of high efficiency fans.

The first stage is to calculate the mean flow velocities and angles base on the information generated in the vortex design procedure. The mean absolute axial flow velocity and mean flow angle are calculated as follows:

$$c_{x_m}(r) = \frac{1}{2}(c_{x_1} + c_{x_2}) \tag{3.6.1}$$

$$tan\beta_m(r) = tan\left(\frac{\beta_1 + \beta_2}{2}\right) \tag{3.6.2}$$

The mean relative velocity is defined as follows:

$$w_m(r) = \frac{c_{x_m}}{cos\beta_m} \tag{3.6.3}$$

Once the mean velocity components have been calculated it is possible to calculate the blade loading factor. The blade loading factor provides a correlation between the lift coefficient and solidity of the fan at every radius.

$$C_L\sigma(r) = 2\left(\frac{c_{\theta_2}}{c_{x_2}}\right)cos\beta_m \tag{3.6.4}$$

In equation 3.6.4 σ denotes blading solidity which is defined as follows:

$$\sigma(r) = \frac{n_b c_h}{2\pi r} \tag{3.6.5}$$

It is clear from equations 3.6.4 and 3.6.5 that chord length (c_h) is a function of the flow velocity components, radius, number of blades and the aerofoil lift coefficient. As the number of blades and flow velocity components are already known, the chord length distribution is essentially a function of the radial distribution of the lift coefficient. In order to optimise the lift coefficient distribution aerofoil data is needed. In this study the NASA LS 0413 aerofoil data of McGhee and Beasley (1976) was used. This data provides lift and drag data for the aerofoil for a range of angles of attack. This allows the fan static efficiency to be estimated.

Fan total-to-total and total-to-static efficiencies are defined by the following equations, as defined by Bruneau (1994):

$$\eta_{tt} = \frac{(\bar{p}_{t2} - \bar{p}_{t1})_{act}}{(\bar{p}_{t2} - \bar{p}_{t1})_{act} + \Delta p_{t_{loss}}} \tag{3.6.6}$$

$$\eta_{ts} = \frac{(\bar{p}_{s2} - \bar{p}_{t1})_{act}}{(\bar{p}_{t2} - \bar{p}_{t1})_{act} + \Delta p_{t_{loss}}} \tag{3.6.7}$$

where:

$$\Delta p_{t_{loss}} = \sum_{r_h}^{r_{tip}} \frac{1}{2} \rho_a K_r c_{x_m}^2 \frac{\dot{m}(r)}{\dot{m}_a} \tag{3.6.8}$$

where for each radial station:

$$K_r = \frac{K_t C_D \phi}{C_L cos^2 \beta_m} \tag{3.6.9}$$

where K_t and ϕ are defined in equations B.1.31 and B.1.33 in Appendix B and:

$$C_D = C_{D_{prof}} + C_{D_{sec}} \tag{3.6.10}$$

where according to Wallis (1983):

$$C_{D_{sec}} = 0.018 C_L^2 \tag{3.6.11}$$

3.6.2 Blading Design - Aerofoil Camber Optimisation

The final phase of the design of the fan blading is to optimise the aerofoil camber distribution. The aim of this optimisation was to optimise the lift to drag ratio along the span of the blade, improving efficiency and reducing the aerofoil angle of attack near the hub in order to improve stall margin. The modification of the aerofoil is carried out using the well known aerofoil design code XFOIL Drela (1989). XFOIL is also used to provide a prediction of the aerofoil lift and drag polars as a function of thickness, Reynolds number and camber. This lift and drag data is then used to estimate efficiency by means of equations 3.6.6 and 3.6.7. Reynolds number is based on the chord length and is calculated as follows:

$$Re = \frac{\rho_a w_m ch}{\mu} \tag{3.6.12}$$

XFOIL was selected as it is known to give a reasonable estimate of aerofoil lift and drag polars as well as having geometry manipulation functionality (Van der Spuy (2011); Carolus and Starzmann (2011*b*)). In the blading design process it was found that the average chord based Reynolds number is 2×10^6 with a minimum of 8.32×10^5 at the hub and a maximum of 3.14×10^6 at the tip. In order to validate the polar predictions of XFOIL, data generated using XFOIL is compared to experimental data for the NASA LS 0413 as presented by McGhee et al McGhee *et al.* (1977) in Appendix D. The results contained in Appendix D show that XFOIL is an appropriate and accurate method of generating aerofoil lift and drag data for the optimisation process performed here. It should be noted that in this study the N_{crit} value in XFOIL's boundary

layer parameters menu is set to 0.1. Larger values of N_{crit} were found to severely under predict drag relative to the data of McGhee et al. at the prescribed Reynolds numbers, which are significantly larger than those of the fan modelled by Carolus and Starzmann (2011b) who used the default value of $N_{crit} = 9$. According to Drela and Youngren (2001) setting a small N_{crit} can mimic the effect of flow transition mechanisms other than the growth of Tollmien-Schlichting waves via linear instability. Several of these mechanisms occur at higher Reynolds numbers as encountered here.

As mentioned, the base aerofoil is the NASA LS 0413 aerofoil. The NASA LS series was developed to have better performance than the commonly used and well documented NACA series (McGhee and Beasley (1973)) especially in terms of stall tolerance. McGhee et $al.$ (1977) measured data for the NASA LS 0413 section with both smooth and rough surfaces, at different Reynolds numbers. This data provides a means to validate XFOIL's polar predictions at different Reynolds numbers, as shown in Appendix D.

Optimisation is once again performed using the SQP method of Powell (1978) as it is well suited to constrained problems. The optimisation target, as with previous design steps, is maximum static efficiency. Maximum camber is allowed to vary between 3.5% and 0.5% of the chord length and the position of maximum camber and thickness are not adjusted. The nominal camber of the NASA LS 0413 aerofoil is 2% and thickness is 13%. These limits are chosen as they result in realistic aerofoil profiles that do not have excessive nose droop. The chosen maximum and minimum camber values also deviate minimally from the nominal camber, which is considered conservative. Thickness is varied linearly along the blade from 13% at the hub to 9% at the blade tip. An additional constraint is that the angle of attack at any point along the blade cannot be greater than 5°, which helps reduce blade twist, as angle of attack is added to the nominal blade twist, as well as allowing for a wider band of stall free performance.

Lift coefficient is a function of chord length, as shown in equation 3.6.4. In the previous section the chord length and lift coefficients were defined using data for the NASA LS 0413 aerofoil. As the chord length and ultimately the required lift coefficient are already known at each radial station along the blade this optimisation step aims to optimise the lift to drag ratio along the blade span. Different camber values are selected by the optimiser for each of the 20 radial stations. A line search is then performed through the XFOIL generated lift and drag data at each radial station to determine firstly the angle of attack and secondly the drag coefficient. Once these two parameters are known the optimiser checks whether the angle of attack values are in range and if fan total-to-static efficiency is at a maximum. The process to calculate efficiency is described in the previous sections (equations 3.6.7 and 3.6.6). Another important parameter calculated at this step is the stagger angle distribution

which describes blade twist:

$$\xi = \beta_1 - \alpha_{att} \tag{3.6.13}$$

Once the maximum is found the code saves the coordinate files for the aerofoil at each radial station, the stagger angle distribution, drag coefficient distribution and the final estimate of static efficiency. It should be noted at this stage that the aerofoils are stacked about their centroids and are cylindrically fitted along the blade span.

3.7   The M-Fan

The fan designed in this study is henceforth referred to as the M-fan and is depicted in fig. 3.4. The M-fan, as well as the design method developed in this chapter are the result of the concept development process detailed in Appendix C. The concept development process makes use of the actuator disk model described in the next chapter.

Key physical parameters and performance estimates are shown in table 3.2. The fan has a camber distribution of 3.5% at the hub and 0.8% at the blade tip. The blades have a very square shape and do not taper much between the hub and tip. This is due to the maximum chord length at the hub being constrained to 1 m as well as the linear chord distribution constraint of less than 1 m. This does however have the benefit of increasing the Reynolds numbers near the blade tip, reducing drag and improving fan static efficiency.
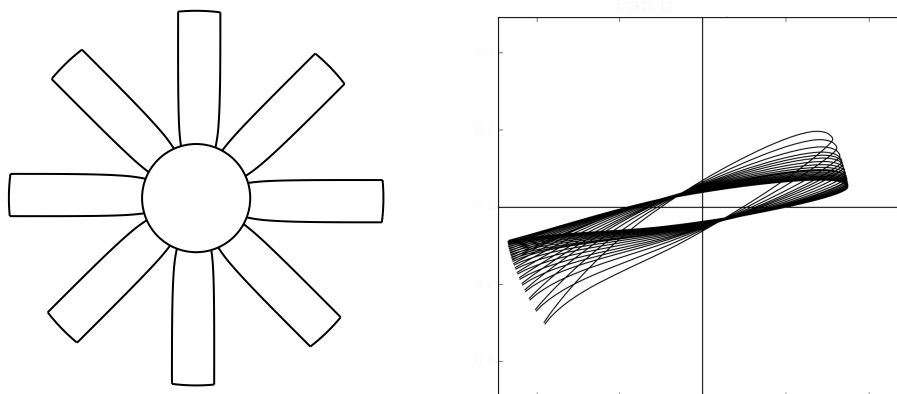
Figure 3.4: Font view (left) and stacking plan (right) of the M-fan

The stacking plan of the M-fan is shown in fig. 3.4. This demonstrates the blade twist. The root blade angle is 34 degrees and the angle of attack is 2.8 degrees at the hub, when operating at the design point. This should give the fan a reasonable stall tolerance at low flow rates. It should also be noted that the blade tip speed is 58 m/s, the maximum allowed by the design

Table 3.2: M-fan Characteristics

Diameter	24 ft [7.3152 m]
Number of blades	8
Hub-to-tip ratio	0.29
Fan rotational speed	151 RPM
Flow rate	333 m^3/s
Estimated fan static pressure	116.7 Pa
Estimated fan power	63 285.21 W
Estimated fan static efficiency	61.4 %

specifications. Lower speeds result in poor total-to-static efficiency. The fan as designed features a flat hub and blade root seals as shown in fig. 3.4.

Chapter 4

The Actuator Disk Model

Three dimensional modelling is computationally expensive, requiring high mesh densities in order to accurately model flow in the vicinity of the fan blading. The actuator disk model (ADM), originally conceived by Thiart and Von Backström (1993), aims to provide a reasonably accurate approximation of the flow field in the vicinity of the fan blades without the need to explicitly model the fan blades, thereby reducing both the computational time required to attain a solution and the required mesh density. This chapter provides details on the variants of the ADM used in this study as well as mesh details and solver settings.

4.1   Introduction

Various authors such as Meyer (2005), Louw (2015), Van der Spuy (2011) and Bonanni *et al.* (2016) have successfully used versions of the ADM to model axial flow fans. In this study two variants of the ADM are used, a standard version based on the ADM of Thiart and Von Backström (1993), which makes use of experimental aerofoil data at a single Reynolds number and a version that makes use of aerofoil polar data derived from XFOIL (Drela (1989)) which is used to model the M-fan, which takes into account aerofoil camber variation and Reynolds number distribution in the fan.

The aims of these models are to:

- **Compare the M-fan with concept designs** - Two versions of the ADM will be used to compare the M-fan with a free vortex design generated using the method of Bruneau (1994) as well as another concept design generated with the method in Chapter 3 that does not include camber optimisation . This will allow the designs to be compared over a selected range of flow rates. The designs will be compared in terms of performance and flow field.

- **Assess whether an ADM can be used as a design tool** - The numerical results from the ADM of the M-fan will be compared to the numerical results obtained from the periodic three dimensional model (P3DM). The results will be compared in terms of fan performance, as well as flow field parameters to determine whether the ADM could be used as a design tool.

- **Provide a simplified numerical model that can be used for modelling the full air-cooled heat exchanger** - The ADM developed for the M-fan aims to be suitable for use in full models of air-cooled heat exchanger systems. In order for this aim to be met the model must accurately predict the fan characteristic curve over a range of flow rates. The model can then be used in studies of a similar nature to Bredell *et al.* (2006) and Van der Spuy (2011).

All computational domains are developed using ANSYS Workbench 17.2 and all simulations are performed using the ANSYS FLUENT 17.2 solver. Simulations were performed on the Rhasatsha high performance computer (HPC) at Stellenbosch University. Simulations were run in parallel across 2 processing cores with 8 Gb of RAM. Convergence was usually attained within 6 to 12 hours.

This chapter details the underlying theory of the actuator disk model. The aerofoil polars used in the standard ADM as well as the XFOIL derived polars used to model the M-fan are discussed. The chapter goes on to detail the computational domains used as well as solver settings and mesh independence.

4.2   Actuator Disk Model Theory

The ADM makes use of blade element theory to calculate the momentum components induced into a flow field by a fan impeller. The fan blades are replaced with an annular disk, one cell wide, at the fan rotor plane. A user defined function (UDF) is implemented at the fan rotor plane in order to introduce the relevant momentum source terms at the cells in the rotor disk. The momentum equations, including source terms, in a cylindrical coordinate system are presented below (equations 4.2.1 to 4.2.3).

$$
\begin{aligned}
&\frac{F_r}{dV} - \frac{\delta p}{\delta r} + \mu \left(\frac{1}{r}\frac{\delta}{\delta r}\left(r\frac{\delta u_r}{\delta r} \right) + \frac{1}{r^2}\frac{\delta^2 u_r}{\delta \theta^2} + \frac{\delta^2 u_r}{\delta x^2} - \frac{2}{r^2}\frac{\delta u_\theta}{\delta \theta} - \frac{u_r}{r^2} \right) \\
&= \rho \left(\frac{\delta u_r}{\delta t} + u_r\frac{\delta u_r}{\delta r} + \frac{u_\theta}{r}\frac{\delta u_\theta}{\delta \theta} + u_x\frac{\delta u_x}{\delta x} - \frac{u_\theta^2}{r} \right)
\end{aligned}
\tag{4.2.1}
$$

$$\frac{F_\theta}{dV} - \frac{\delta p}{\delta \theta} + \mu \left(\frac{1}{r} \frac{\delta}{\delta r} \left(r \frac{\delta u_\theta}{\delta r} \right) + \frac{1}{r^2} \frac{\delta^2 u_\theta}{\delta \theta^2} + \frac{\delta^2 u_\theta}{\delta x^2} + \frac{2}{r^2} \frac{\delta u_r}{\delta \theta} - \frac{u_\theta}{r^2} \right)$$
$$= \rho \left(\frac{\delta u_\theta}{\delta t} + u_r \frac{\delta u_\theta}{\delta r} + \frac{u_\theta}{r} \frac{\delta u_\theta}{\delta \theta} + u_x \frac{\delta u_\theta}{\delta x} + \frac{u_\theta u_r}{r} \right) \tag{4.2.2}$$

$$\frac{F_x}{dV} - \frac{\delta p}{\delta x} + \mu \left(\frac{1}{r} \frac{\delta}{\delta r} \left(r \frac{\delta u_x}{\delta r} \right) + \frac{\delta^2 u_x}{\delta r^2} + \frac{1}{r^2} \frac{\delta^2 u_x}{\delta \theta^2} - \frac{\delta^2 u_x}{\delta x^2} \right)$$
$$= \rho \left(\frac{\delta u_x}{\delta t} + u_r \frac{\delta u_x}{\delta r} + \frac{u_\theta}{r} \frac{\delta u_x}{\delta \theta} + u_x \frac{\delta u_x}{\delta x} \right) \tag{4.2.3}$$

The time averaged momentum source terms, F_x, F_θ and F_r are used to introduce the forces applied by the fan at the rotor plane into the flow field. In order to calculate these source terms the fan is replaced by three disks as shown in figure 4.1, one at the rotor plane and an upstream and downstream disk placed at a distance of $x/ch_{avg} > 0.5$ from the rotor disk. Each disk is one computational cell thick in the axial direction and all three disks are made up of hexahedral mesh elements with identical cell distributions in the radial and tangential directions. Geometrically the disks are identical in thickness.
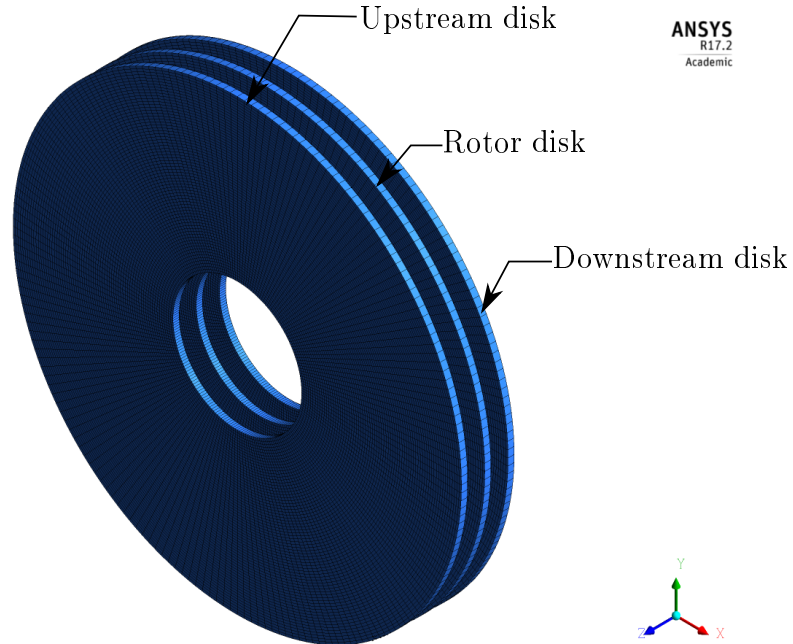
Figure 4.1: Disks used to implement ADM

In order to implement the UDF each cell in the rotor disk is linked with the corresponding two cells in the axial direction in the upstream and downstream disks. In the computational environment the average relative velocity vectors are obtained at the upstream and downstream disks. These vectors are then

used to obtain the angle of attack across a fan blade element. This allows the lift and drag forces generated by the blade to be calculated at radial increments and introduced at the rotor plane in the form of momentum source terms as previously mentioned.

According to Bruneau (1994) provided solidity is below 0.7, two-dimensional blade element theory is appropriate for calculating the forces exerted by the fan blades on the flow field. Although this is not true for the M-fan, close to the hub the majority of the blading has sufficiently low solidity so two-dimensional theory is applicable. With the angle of attack known from the relative velocity vector data extracted at the upstream and downstream disks, the lift and drag force applied at a given radius can be calculated using equations 4.2.4 and 4.2.5 with reference to figure 4.2.
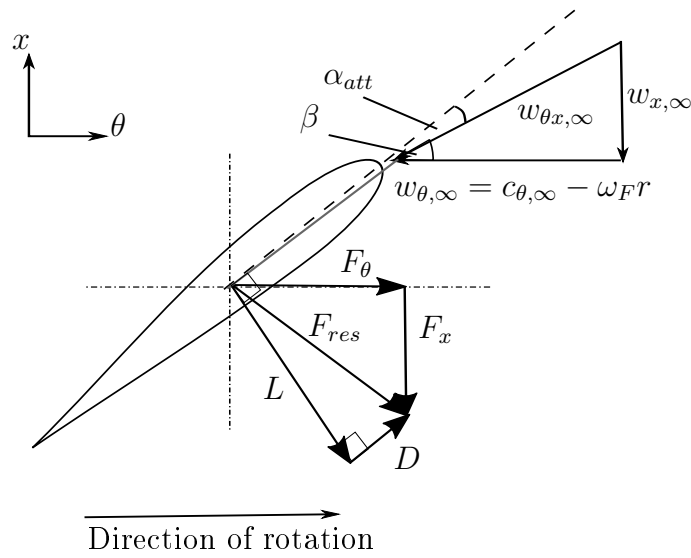
Figure 4.2: Force components acting on a two dimensional blade element

$$L = \frac{1}{2}\rho w_{\theta x,\infty}{}^2 C_L ch.\delta r \tag{4.2.4}$$

$$D = \frac{1}{2}\rho w_{\theta x,\infty}{}^2 C_D ch.\delta r \tag{4.2.5}$$

The lift and drag coefficients used in equations 4.2.4 and 4.2.5 are extracted from aerofoil data acquired from wind tunnel tests or numerical sources such as XFOIL or CFD. The term δr represents the differential thickness of the blade element. Once the lift and drag forces are known the axial and tangential forces actuated by the fan blade element can be calculated as follows:

$$F_x = Lcos\beta + Dsin\beta \tag{4.2.6}$$

$$F_\theta = Lsin\beta - Dcos\beta \tag{4.2.7}$$

The force values calculated in equations 4.2.6 and 4.2.7 can then be used to calculate the momentum source terms that are introduced at the rotor disk. It should be noted that the radial force term is assumed to be small and neglected (Thiart and Von Backström (1993)). The source terms are calculated as follows:

$$\frac{\sum F_x}{dV} = \frac{F_x}{\Delta x s_p} \tag{4.2.8}$$

$$\frac{\sum F_\theta}{dV} = \frac{F_\theta}{\Delta x s_p} \tag{4.2.9}$$

$$\frac{\sum F_r}{dV} = 0 \tag{4.2.10}$$

Where Δx is the disk cell thickness in the axial direction and s_p is the circumferential blade pitch.

The ADM is implemented into ANSYS FLUENT 17.2 by means of a user defined function (UDF) written in the C programming language. Inputs to the UDF include number of blades, spanwise chord length distribution, spanwise blade angle distribution, aerofoil C_L vs angle of attack data and aerofoil C_D vs angle of attack data. Once the UDF has been compiled into the flow domain it calculates the momentum source terms generated by the fan blading and introduces them at the rotor disk at each iteration, based on velocity data extracted at the upstream and downstream disks.

4.3   Aerofoil Polars

Aerofoil lift and drag data, also commonly referred to as aerofoil polars are key to the implementation of the ADM, as mentioned in the previous section. This data can be obtained from a variety of sources such as experimental data from wind tunnel tests, CFD simulations or other numerical techniques such as XFOIL (Drela (1989)). In this study two different sets of aerofoil data are used, one derived from experimental data for the NASA LS aerofoil series which is used to model early concepts and another derived from XFOIL, used to model the aerofoil profile variation incorporated into the M-fan. Both data sets are briefly discussed below. Appendix D contains an extensive study that was used to validate XFOIL as a source of aerofoil polar data as well as comparing XFOIL data to CFD and experimental data.

4.3.1   Standard Model

The standard actuator disk model, used in Appendix C, makes use of the aerofoil data for the NASA LS 0413 profile, as presented by McGhee *et al.* (1977). McGhee *et al.* (1977) tested the NASA LS 0413 at various Reynolds numbers

for angles of attack between -10 and 20 degrees. The data set for a Reynolds number of 2.1×10^6 is used in this study as this value is nearest the average Reynolds number in the given designs ($\approx 2.0 \times 10^6$). Thickness variation is not accounted for in this approach, instead it is assumed conservative to use aerofoil data for the maximum blade thickness across the entire blade span.

4.3.2   XFOIL Derived Model

The M-fan has varying aerofoil camber along its blade span, essentially creating a new aerofoil series for which there is no experimental data. As experimental aerofoil testing was not an option, aerofoil data is acquired using XFOIL (Drela (1989)). XFOIL allows for aerofoil camber, thickness and Reynolds number to be taken into account. XFOIL is used to calculated the aerofoil polars for the 21 radial stations used in the fan design process. The polars are generated for angles of attack between -10 degrees and 20 degrees, at the given Reynolds number at each radial station as calculated in the blading design procedure. Both the C_L and C_D values are plotted as a function of radius ratio (r/r_{tip}) and angle of attack, as shown in figure 4.3. Fifth order polynomial three dimensional curve fits are then applied to the data sets using MATLAB's curve fitting toolbox and these functions are then coded into the ADM UDF.
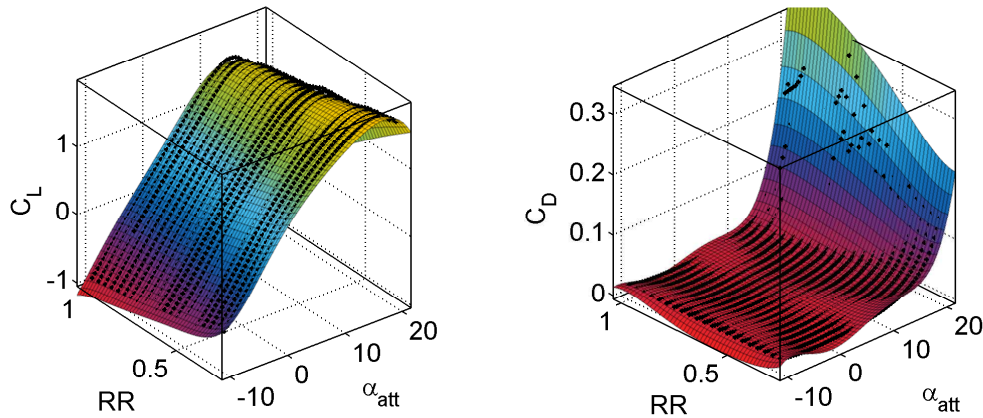
Figure 4.3: C_L (L) and C_D (R) distributions in the M-fan as a function of radius ratio and angle of attack

For values outside of the range of angles of attack used by XFOIL, flat plate lift drag characteristics are used. According to Hoerner and Borst (1975) and Hoerner (1965) these characteristics can be described by the following equations:

$$C_L = C_{D_{max}} sin(\alpha_{att})cos(\alpha_{att}) \qquad (4.3.1)$$

$$C_D = C_{D_{max}} sin^2(\alpha_{att}) \qquad (4.3.2)$$

where:

$$C_{D_{max}} = 1.98 \tag{4.3.3}$$

This allows the model to be used at low flow rates, where angles of attack may fall outside of the range for which XFOIL data is available.

4.4   Computational Domain

Two computational domains are used by the ADM, one with a geometry representing a scaled up version of the 1.5 m BS848 type A test fan test facility at Stellenbosch University and another consisting of an annular duct. Both domains model the fan at full scale (24 ft) The BS848 domain and relevant boundary conditions are shown in figure 4.4.
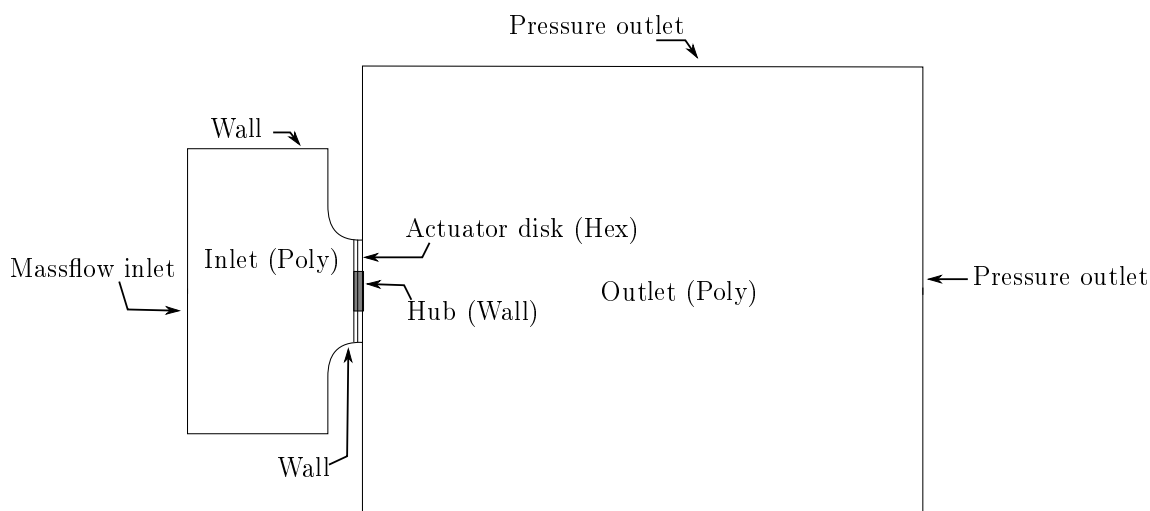
Figure 4.4: ADM computational domain and boundary conditions

The BS848 domain consists of three sub-domains, the inlet, disk section and outlet. The inlet and outlet sub-domains consist entirely out of polyhedral elements while the disks are made up of hexahedral elements.

The annular domain is also made up of three sub-domains, the inlet, disk section and outlet. These domains are meshed in the same manner as for the BS848 domain. The annular inlet and outlet sections are 4 m in length and have wall boundary conditions applied at both the inner and outer walls. The inlet and outlet boundary conditions are the same as for the BS 848 domain.

All walls have inflation applied in order to ensure that y+ values are in the range required by the selected turbulence model ($30 \leq y+ \leq 300$). The hub walls are specified to rotate at the fan rotational velocity in order to replicate operating conditions. The mass flow inlet is specified to have a desired flow rate (dependent on desired volume flow) in the axial direction with a turbulence

intensity of 3% and a length scale of 0.01. As with the P3DM this is due to the presence of a screen upstream of the fan. The pressure outlet boundaries are specified to have a gauge pressure of 0 Pa and a backflow turbulence identical to that of the mass flow inlet.

The final mesh consists of 3.1×10^6 cells, with 70 radial increments and 200 tangential increments in the three disks. Results of a mesh density study are shown in table 4.1. The results in table 4.1 show that this model is mesh independent beyond a density of 1.05×10^6 cells.

Table 4.1: ADM mesh independence

Mesh	Cells	Total-to-static pressure rise $[Pa]$
1	1.05E+06	110.9
2	2.75E+06	111.8
3	8.81E+06	111.2

4.5 Solver Settings

The realizable $k - \epsilon$ turbulence model of Shih *et al.* (1995) with standard wall functions is applied for the ADM. This is based on the recommendations of Louw (2015). This model has been shown to give results that correlate well with experimental fan test data (Wilkinson *et al.* (2016) and Louw (2015)). Additional solver settings are shown in table 4.2.

Table 4.2: ADM solver settings

Pressure - velocity coupling	SIMPLE
Pressure	PRESTO!
Gradient	Least squares cell based
Momentum	QUICK
Turbulent kinetic energy	QUICK
Turbulent dissipation rate	QUICK

In order to obtain convergence it is important to under relax momentum to 0.3 and body force terms to 0.0001. This aids solution stability as body force terms introduced by the UDF at the rotor disk plane tend to be large early in the simulation. After the first 100 iterations the body force term under relaxation can be set back to 1, in order to reduce the number of iterations required. Simulations are started with first order discretisation schemes for momentum and turbulence before being switched to QUICK for more accurate

results. This provides better stability early on in the simulation. All other under relaxation factors are set to the default values provided by ANSYS FLUENT 17.2. Convergence levels obtained are in the range of 10^{-4}.

Chapter 5

Periodic Three-dimensional Numerical Model

In order to validate the design of the M-fan as well as the design methodology used, an accurate numerical model is required. This is even more important as no experimental testing forms part of this study. Additionally simplified models such as the actuator disk model (ADM) need to be validated against either experimental or accurate numerical data in order to validate assumptions made. Owing to the computational challenges posed by the sheer size of the M-fan, a one eighth segment containing a single blade is modelled. Simple one eighth annular segments adjoin the rotor up and downstream of the blade in order to aid convergence, whilst eliminating the computational elements required to model a free inlet free outlet scenario with a bellmouth and hub plate. These simplifications mean that the M-fan can be successfully modelled using the available computational resources. In addition the simplified inlet means that the inflow conditions are directly comparable with the assumptions made in the design technique, meaning that the flow field data obtained from the periodic three dimensional model (P3DM) is directly comparable with the designed flow field.

5.1   Introduction

The P3DM assumes that flow is periodic with respect to the blade pitch, which may not be true should effects such as rotating stall be present. However on a similar model Louw (2015) found that the results obtained in terms of fan performance and blade surface pressure distributions compared well to experimental data. Louw (2015) also states that effects such as rotating stall are most prevalent at low flow rates which are not considered by this study.

The numerical data provided by the P3DM serves to:

- **Validate the fan design algorithm** - Numerical fan characteristic and flow field data will be compared to the values calculated in the design

method presented in Chapter 3. These results will be used to assess the validity of the design method as well as the assumptions made. A model with zero tip gap will be used as the design algorithm does not take tip effects into account.

- **Provide an estimate of fan performance over a limited range of flow rates** - The performance of the M-fan will be modelled at selected flow rates $(265\,\text{m}^3/\text{s} \leq \dot{V} \leq 385\,\text{m}^3/\text{s})$ in order to determine its suitability for purpose and performance at off design flow rates. Very low flow rates where transient modelling is required are not considered by this study.

- **Provide insight into the effect of tip clearance on the M-fan design** - Versions of the P3DM with 3 different tip gaps will be run at the selected flow rates. The results obtained will be used to analyse the effect of tip gap on fan performance as well as the flow field in the vicinity of the blades. This data will be used to recommend whether the tip gap should be reduced from the design value.

- **Validate the actuator disk model** - As the M-fan has variable aerofoil camber with respect to blade span, a new iteration of the ADM is to be developed in order to take this into account. Data from the P3DM will be used to validate this model both in terms of its prediction of fan performance as well as the flow field upstream and downstream of the fan blading.

The blade geometry and computational domain are developed using ANSYS Workbench 17.2 and the flow was solved using ANSYS FLUENT 17.2. All simulations were, unless otherwise stated, performed on the Rhasatsha high performance computer (HPC) at Stellenbosch University. Simulations were run in parallel across 32 processing cores with 64 Gb of RAM. Convergence was usually attained within 36 to 48 hours.

The remainder of this chapter provides further details on the P3DM such as the computational domain and boundary conditions. This is followed by a discussion of turbulence models as well as other desecretisation models and solver settings used. A detailed mesh sensitivity study is also presented in Appendix E containing information on mesh size and boundary proximity.

5.2 Computational Domain

The P3DM computational domain consists of three elements, the rotor sub-domain and the upstream and downstream sub-domains. The construction of the overall domain as well as relevant mesh boundary conditions is shown in figure 5.1. The domain is orientated such that the negative z direction is the positive axial flow direction. The mesh sensitivity analysis used to determine the mesh densities and inlet and outlet lengths can be viewed in Appendix E.

As the rotor domain is the most complex of the three, this will be discussed first, followed by the inlet and outlet domains. Finally the mesh boundary conditions and interfaces will be explained in detail.
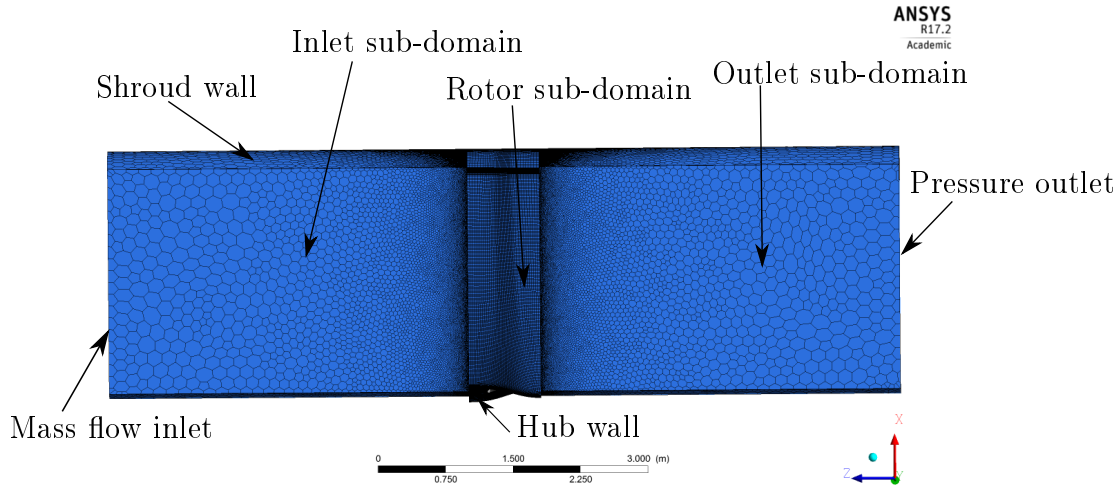
Figure 5.1: P3DM computational domain and boundary conditions

5.2.1 Rotor Sub-Domain

In order to construct the rotor sub-domain a three dimensional CAD model of the M-fan blade is generated in Autodesk Inventor 2013 using the coordinate files generated by the design algorithm presented in Chapter 3. The blade is then imported into ANSYS Workbench 17.2 in IGES format and meshed using ANSYS Turbogrid. Three different versions of the rotor sub-domain are created, one with zero tip gap, one with the design tip gap (0.0293 m) and one with half of the design tip gap (0.0146 m). All meshes are identical aside from the tip gap and the sub-domain has an axial length of 0.8 m. The zero tip rotor sub-domain is shown in figure 5.2.

The rotor sub-domains consist entirely of hexahedral elements as shown in figure 5.2. ANSYS Turbogrid is specifically developed for meshing turbomachinary blading, thus the mesh is optimised to smoothly fit around the blade. Mesh elements are orientated in the flow direction over the majority of the blade surface. Towards the blade tip many elements further away from the blade are not well aligned with the flow direction. This is a potential source of error however this is hard to quantify without experimental data. Analyses performed in Appendix E shows that misaligned elements do affect the pressure difference across the fan, however this difference is small. The cells on the blade surface are constructed in such a way that for the majority of cells the $y+$ values are between $1 \leq y+ \leq 5$. The blade surface mesh is also biased
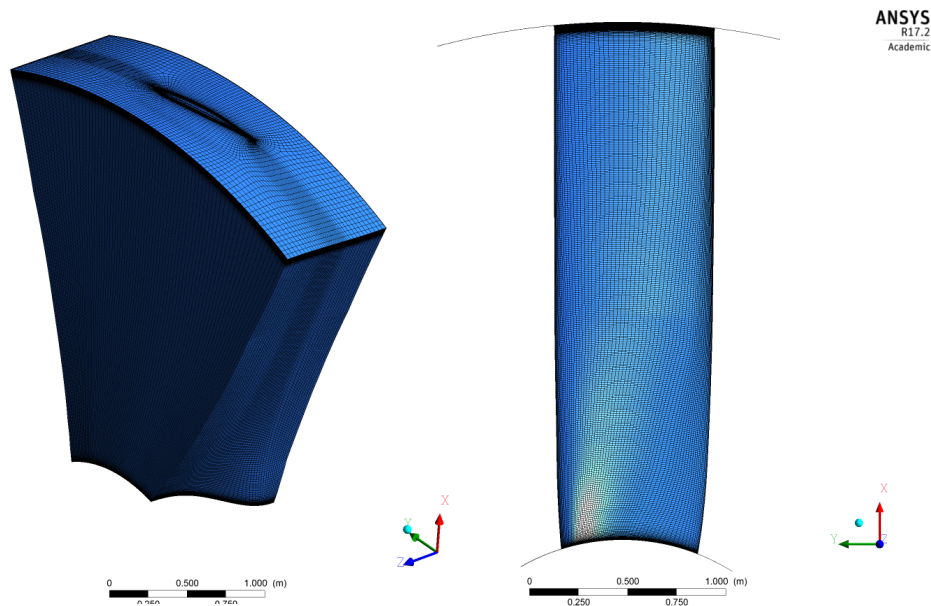
Figure 5.2: Rotor sub-domain (L) and blade surface mesh (R)

towards the hub and shroud to account for wall effects in these regions, as shown in figure 5.2. Due to the length of the blade and the large difference in Reynolds number between the hub and tip some elements in the tip region fall outside this constraint. In order to account for this most simulations are run with enhanced wall functions. According to the mesh sensitivity analysis presented in Appendix E a mesh density of 6×10^5 elements is sufficient for convergence provided that the mesh quality is reasonable. In order to provide better resolution of the flow and account for the reduction in mesh quality when adding a tip gap, all rotor sub domains have a mesh density of 1.8×10^6 elements or greater.

Both the design tip gap and reduced tip gap meshes contain 40 elements between the blade tip and shroud. This value is reasonable as determined in Appendix E.

5.2.2   Inlet and Outlet Sub-Domains

Inlet and outlet boundary proximity tests performed in Appendix E show that $4\,\mathrm{m}$ is an acceptable length for both inlet and outlet sub-domains. For this reason and the sake of convenience, the two domains are mirror images of one another. Both domains are constructed in the ANSYS Meshing environment within ANSYS Workbench 17.2. The domains are $1/8th$ sections of an annular duct, as shown in figure 5.3. The same domains are used for all three variants of the rotor sub-domain.
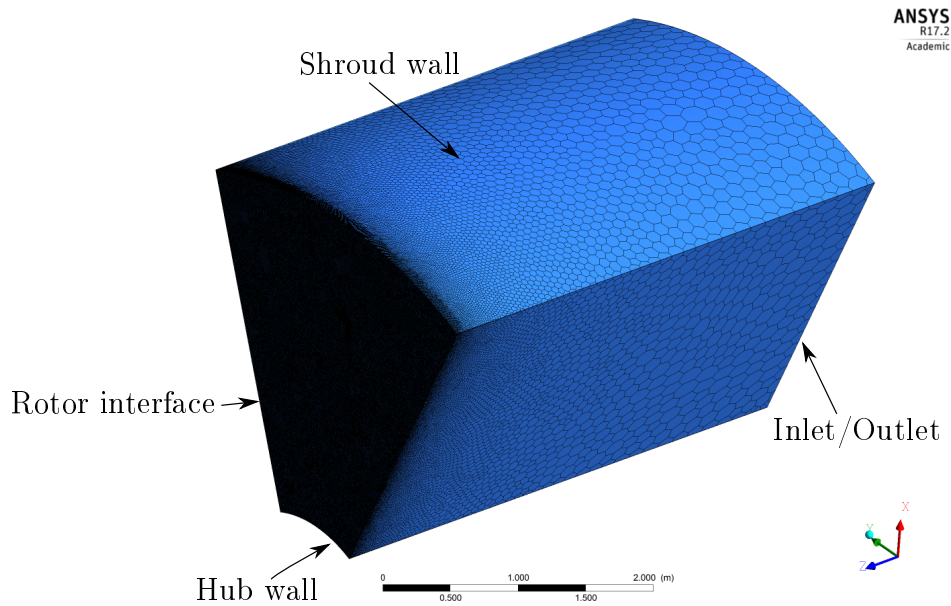
Figure 5.3: Inlet/outlet sub-domain

The inlet and outlet sub-domains consist entirely of polyhedral mesh in order to reduce mesh size and improve accuracy. The faces adjoining the rotor sub-domain are specified to have an element size of 0.005 m. This ensures that the mesh density is adequate for the use of non-conformal mesh boundaries. The mesh is then inflated away from the face adjoining the rotor sub-domain. Mesh density tests performed in Appendix E confirm that a mesh size of 8.7×10^6 elements in each domain is sufficient. The sub-domains are used in conjunction with all three rotor sub-domains in order to build three separate meshes. The inlet and outlet sub-domains have mesh inflation applied at the walls of the annular section in order to ensure that the wall $y+$ values are within the specified range ($1 \leq y+ \leq 5$)

5.2.3   Boundary Conditions and Mesh Interfaces

The P3DM model consists of a one eight segment of the M-fan. In order to implement the pairs of periodic boundary conditions, a 45° angular separation are placed along the symmetry plane of the fan. Owing to the construction of the domain there is one periodic pair per sub-domain, as shown in figure 5.4. These periodic pairs allow flow that exits one periodic boundary to re-enter the domain at the corresponding periodic boundary.

In order to assemble the sub-domains into a single computational domain, non-conformal mesh interfaces are required. To implement these interfaces the inlet and outlet sub-domains must be correctly orientated so that the interface faces of each domain meet. Two periodic repeat non-conformal mesh interfaces are used to join the rotor sub-domain to the inlet and outlet. This

type of interface is used as it can take into account flow that passes through periodic boundary pairs on either side of the interface. This type of interface is specifically recommended by the ANSYS user guide for situations of the type portrayed in figure 5.4. The interface applies an interpolation scheme that allows all relevant properties to be transferred from one sub-domain to the next.
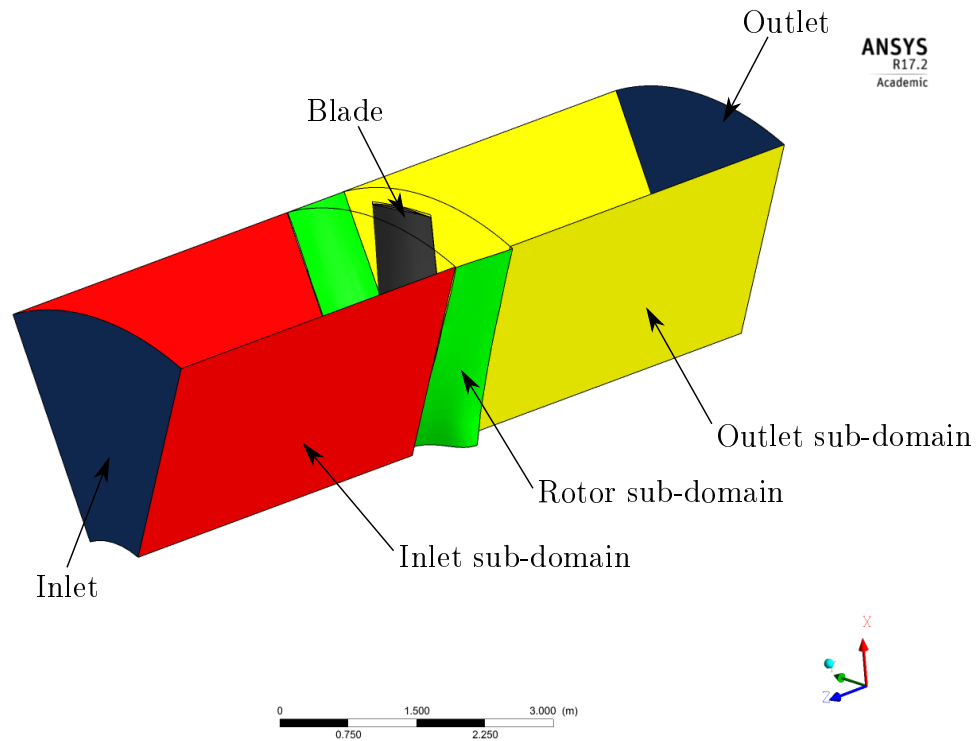
Figure 5.4: Full P3DM computational domain with periodic pairs denoted in red, green and yellow

Owing to the meshing scheme applied by Turbogrid when developing the blade mesh, there is a mismatch between the meshing at the blade tip for the meshes where a tip gap is included. Turbogrid automatically creates two surfaces in the tip gap at the plane where the mismatch occurs. These surfaces are used to create a standard non-conformal mesh interface where fluid properties are interpolated between the two surfaces, allowing properties to be transported across the tip gap.

The inlet is specified to be a mass-flow inlet, with flow entering the domain at a specified mass-flow rate in the negative z direction. The flow is specified to enter with a turbulence intensity of 3% and a length scale of 0.01. These values are lower that what one would expect for free stream turbulence as fans of this type are typically fitted with a mesh screen directly upstream of the fan in order to prevent the ingestion of debris, these screens also have the effect of reducing the fan inlet turbulence. It should be noted that the above values

are assumed and should be cross checked once details of the final fan set up and experimental fan test data become available. The outlet boundary is set to be a pressure outlet with a gauge pressure of 0 Pa. The backflow direction is specified as normal to the boundary and backflow turbulence is specified to be the same as inlet turbulence.

All sub-domains are set to rotate about the positive z axis at the fan rotational speed (15.8 rad/s) in the relative coordinate scheme. The fan blade and hub surfaces are set to be stationary as in this frame of reference they would be stationary relative to the flow. Both the hub and fan blade surfaces are set to be no slip wall boundaries. The shroud, inlet and outlet duct walls are set to have a rotational speed of 15.8 rad/s about the positive z axis in the absolute frame of reference as these surfaces are moving in this direction from the point of view of the blade and hub. Likewise the above mentioned surfaces are set to be zero slip walls.

5.3   Turbulence Modelling and Solver Settings

In Chapter 2 it was concluded that the majority of literature concerning this type of fan model made use of a variant of the $k - \epsilon$ model of Launder and Spalding (1974). Louw (2015) made use of the Realizable $k - \epsilon$ model of Shih *et al.* (1995), which is better suited to the flow conditions encountered in turbomachinery. For the sake of completeness the standard $k - \epsilon$, realizable $k - \epsilon$ and transitional SST turbulence models are compared at the design flow rate (333 m^3/s) in table 5.1. The turbulence models are compared on the zero tip gap mesh. Additionally two types of wall function are compared for the two variants of the $k - \epsilon$ model, standard wall functions and enhanced wall functions. Standard wall functions approximate the boundary layer at the wall using the law of the wall, whereas enhanced wall functions are capable of solving the boundary layer explicitly, provided the wall $y+$ is in the range of $1 \leq y+ \leq 5$. For areas where the wall $y+$ is higher than 5 an enhanced wall function is applied. In order to simulate with standard wall functions the domain is adjusted so that the majority of cells at the walls have a $y+$ value between 30 and 300. For enhanced wall functions as well as the Transitional SST model the mesh is refined so that $1 \leq y+ \leq 5$ in the majority of cells. Table 5.1 shows that all variants of the $k - \epsilon$ model give similar results in terms of fan total-to-static pressure rise and total-to-static efficiency. The transitional SST model predicts a higher efficiency and total-to-static pressure rise, indicating that transition may be present on the blade surface. However as no experimental data is available for the M-fan at present it is decided to be conservative and use a variant of the $k - \epsilon$ model, in accordance with the vast majority of literature. As expected the realizable $k - \epsilon$ model of Shih *et al.* (1995) is more optimistic, as it is better conditioned to rotating flow. The realizable $k - \epsilon$ model also attained convergence in a shorter time span than the

Table 5.1: P3DM result at the design flow rate ($333\,\mathrm{m}^3/\mathrm{s}$) obtained with different turbulence models

Model	ΔP_{ts} [Pa]	η_{ts}
Realizable $k - \epsilon$ (Std wall fns)	112.90	0.58
Realizable $k - \epsilon$ (En wall fns)	114.66	0.59
Standard $k - \epsilon$ (Std wall fns)	111.32	0.58
Standard $k - \epsilon$ (En wall fns)	110.28	0.57
Transitional SST	120.11	0.62

standard $k - \epsilon$ model, for both types of wall function. Standard wall functions result in faster convergence than enhanced wall functions, however the result is less certain as fewer cells conform to the wall $y+$ requirements stipulated than for the enhanced wall function case, owing to spanwise Reynolds number variation on the blade as well as mesh quality requirements. In addition to the wall $y+$ values being being better constrained in the enhanced case, the enhanced wall functions are better suited to coping with cells with $y+$ values greater than 5. Thus the Realizable $k - \epsilon$ model with enhanced wall functions is selected for use in the remainder of P3DM simulations in this study.

Table 5.2: P3DM solver settings

Pressure - velocity coupling	SIMPLE
Pressure	PRESTO!
Gradient	Least squares cell based
Momentum	QUICK
Turbulent kinetic energy	QUICK
Turbulent dissipation rate	QUICK

The remaining discretisation schemes and solver settings are shown in table 5.2. These are selected based on the recommendations of Louw (2015) as well as the ANSYS user guide. In order to solve the flow the momentum and turbulence dicretisation schemes are initially set to first order upwind and the flow is simulated to convergence before the schemes are switched to second order upwind and finally QUICK in order to give more accurate results.

Finally all under-relaxation factors are set to the default values proposed by FLUENT. Convergence levels attained for all simulations conducted in this study are in the region of 10^{-5}.

Chapter 6

Results and Discussion

Several sets of results are presented and discussed in order to assess to what extent the aims of this study have been met. This includes results that validate the design procedure and analyse the performance of the M-fan under different conditions. The M-fan is then modelled with zero tip gap by the periodic three dimensional model (P3DM) over a range of flow rates. The results are compared to those of the XFOIL actuator disk model (ADM) for the M-fan, in both the BS848 and annular domains, in order to validate the XFOIL ADM. These results are then compared to certain data sets extracted from the design procedure in order to validate assumptions as well as assess the accuracy of the procedure. Finally a detailed performance analysis is performed using all three variants of the P3DM in order to determine the effect of tip gap on performance as well as investigate the flow field in the vicinity of the blades. It is hoped that this information can be used to improve future designs by providing data on the impact of tip gap on the fan vortex distribution.

6.1 Actuator Disk Model and Design Procedure Validation

The ADM used to model the M-fan and the design procedure presented in Chapter 3 have several features and assumptions in common. Both assume that the radial flow component is negligible and do not account for tip gap related effects. The ADM also makes use of the aerofoil data generated by XFOIL during the camber optimisation process. As the design procedure and ADM make use of similar assumptions and data sets it is important to validate them against a more accurate CFD model such as the P3DM or experimental data. In this case they are validated against a zero tip gap variant of the P3DM, which explicitly models the fan blading within the flow field under the same conditions assumed by the design code, namely uniform inflow and no tip gap. The annular ADM should have inflow conditions identical to those seen by the fan in the P3DM whereas the inflow conditions experienced by

the fan in the BS848 domain are more representative of the fan in its intended operating environment. The models and design code are compared in terms of fan performance and flow field in the vicinity of the fan blading, with the aim of validating the design code as well as the performance and flow field predictions of the ADM.

6.1.1 Fan Performance

The fan performance results for the M-fan across a selected range of flow rates (265-385 m^3/s) are shown in figures 6.1, 6.2 and 6.3. In each figure the results of the BS848 ADM, annular ADM and P3DM with zero tip gap are compared to one another as well as the design code estimate of performance, at the operating point of the fan.
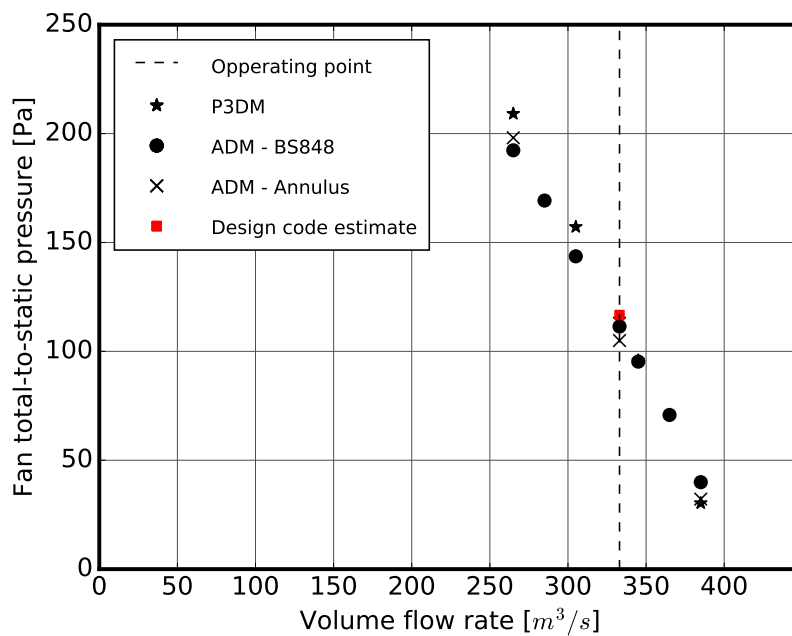
Figure 6.1: Fan total-to-static pressure characteristics as estimated by the ADM, P3DM and design code

The fan total-to-static pressure characteristics predicted by the ADM and P3DM are shown in figure 6.1. It can be seen that the pressure characteristics estimated by all three models correlate reasonably well with one another. There is a visible difference in the gradients of the pressure characteristics predicted by the annular and BS848 ADM simulations. This could be due to the differences in inflow conditions between the two models owing to the different computational domains. The P3DM predicts a steeper total-to-static pressure characteristic than both ADM simulations. Both the P3DM and BS848 ADM
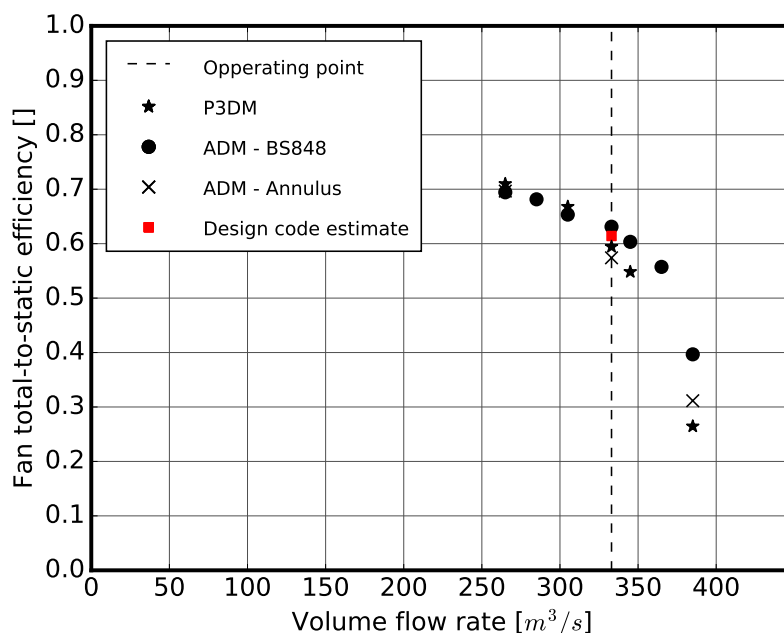
Figure 6.2: Fan total-to-static efficiency characteristics as estimated by the ADM, P3DM and design code

models correlate well with the design code estimate of total-to-static pressure at the operating point. Total-to-static pressure at the operating point is shown to be 4.5% lower than the design specified value by the BS848 ADM and 1.7% lower by the P3DM. The correlation between the total-to-static pressure characteristics predicted by the P3DM and ADM validates the ADM used to model the M-fan. This in turn shows the XFOIL derived polar data used in the design procedure as well as this version of the ADM to be relatively accurate. Additionally this provides additional backing for the findings made in Appendix C. All three numerical models also predict a steep pressure rise characteristic indicating that the M-fan will be suited for use in an air-cooled heat exchanger, based on findings in literature presented in Chapter 2.

The fan total-to-static efficiency characteristics are depicted in figure 6.2. It can be seen that the BS 848 ADM does not correlate well with the P3DM across the full range of flow rates. The annular ADM correlates better with the results of the P3DM and both ADM models provide a reasonable efficiency estimate relative to the P3DM at lower flow rates. For flow rates beyond $305\,\mathrm{m}^3/\mathrm{s}$ the BS848 ADM overestimates total-to-static efficiency by an increasingly large margin. The error in pressure prediction for flow rates between $305\,\mathrm{m}^3/\mathrm{s}$ and $365\,\mathrm{m}^3/\mathrm{s}$ is too small to explain this, however as shown in figure 6.3 the BS848 ADM tends to under predict fan power consumption at all flow rates presented here. This, along with the slightly shallower pressure characteristic explain why the ADM tends to under predict efficiency at low flow rates and over

predict efficiency at high flow rates. At the operating point the BS848 ADM shows that the efficiency of the M-fan will exceed the design code estimate, while the P3DM and annular ADM show that neither the design code estimate nor the specified target of 60% will be met.
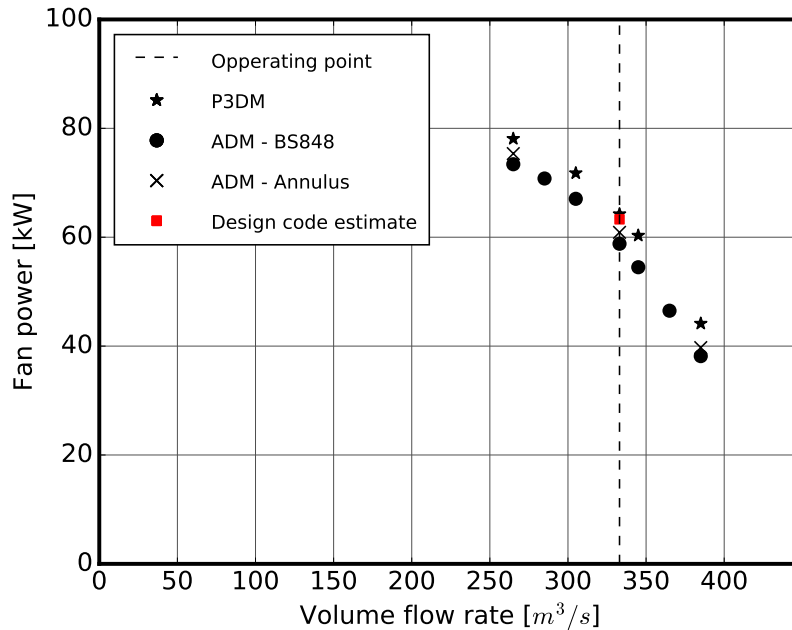
Figure 6.3: Fan power characteristics as estimated by the ADM, P3DM and design code

The power characteristic curves shown in figure 6.3 show that the BS 848 ADM under predicts power relative to the P3DM. This result is consistent with findings in literature that indicate that the actuator disk model does not accurately predict fan power. Wilkinson *et al.* (2016) found that the ADM tended to over predict power whereas Meyer and Kröger (2001) found that it tended to under predict power. Both studies were carried out on the B-fan, however the computational domains, as well as solvers used, differ. This should be further investigated as poor power prediction leads to inaccurate predictions of fan total-to-static efficiency. The annular ADM shows improved power estimation, indicating that inflow conditions may have an impact on fan power consumption.

Table 6.1 provides a direct comparison between the operating point performance characteristics estimated by the design code and the results of the three numerical models. With regards to fan total-to-static pressure at the operating point it can be seen that all values are within $11.7\,\mathrm{Pa}$ of one another. The error in pressure when compared to the design specification is 4.5% for the BS848

Table 6.1: Comparison of M-fan performance characteristics at the operating point ($333\,\mathrm{m^3/s}$)

	Design code	ADM - BS848	ADM - Ann	P3DM
$\Delta\mathrm{p}_{ts}$	116.7 Pa	111.4 Pa	105 Pa	114.7 Pa
η_{ts}	61.4%	63.1%	57.4%	59.4%
P_F	63285.2 W	58797.7 W	60888.1 W	64241.1 W

ADM, 10% for the annular ADM and 1.7% for the P3DM. These results indicate that the pressure rise requirement specified in the design specification has been met by the M-fan. In terms of total-to-static efficiency it can be seen that the values predicted by both the design code and the BS 848 ADM are optimistic relative to the P3DM value, where as the efficiency predicted by the annular ADM is lower. These discrepancies indicate that some losses may not be accounted for by the design code. It is also clear from the differences between the BS848 and annular ADM results that the inlet conditions have an impact on fan performance. In terms of power the design code estimate and P3DM result are within $1000\,\mathrm{W}$ of one another, however as previously mentioned the ADM predicts a far lower power. The small error between the P3DM and design code in terms of pressure, power and efficiency indicate that the assumptions made and methods applied in the design code are valid.

6.1.2   Operating Point Flow Field Analysis

In order to validate the flow field predicted by the ADM simulations, the flow field predictions of the BS848 ADM and annular ADM are compared to results from the P3DM. Additionally the downstream axial and tangential velocity distributions calculated by the vortex design procedure for the M-fan are also compared to the numerically obtained data. Figure 6.5 shows the inlet and outlet non-dimensionalised axial, tangential and radial velocity distributions predicted by the BS848 ADM, annular ADM and the P3DM at the operating point ($333\,\mathrm{m^3/s}$). Design velocity distributions are displayed for the outlet tangential and axial distributions.

Flow field data is extracted from the numerical models by taking circumferential averages of the various velocity components of the planes at the locations shown in figure 6.4. Although this is some distance away from the fan blading, meshing does not allow the planes to be moved any closer. In both cases the upstream and downstream planes are within a straight duct section, meaning that the velocities and angles should not differ significantly from those at the blade leading and trailing edges.

Considering figure 6.5, it is clear that the BS848 ADM predicted inlet velocity distributions differ from those predicted by the P3DM and annular ADM. This is as a result of the differing geometry in the two computational
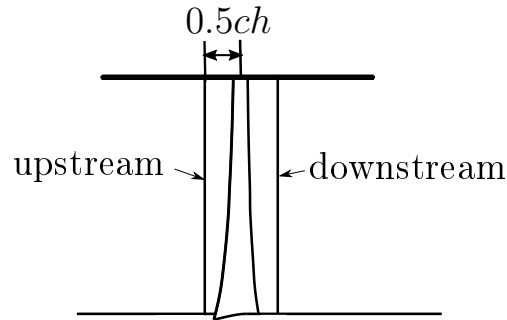
Figure 6.4: Measurement locations for velocity data in the P3DM

domains. The BS848 ADM is used to model the M-fan in a straight duct with a box hub and bellmouth inlet, whereas due to mesh size constraints the P3DM models the fan blading within a simple annular duct. The presence of the box hub in the BS848 ADM results in flow separation occurring off the edge of the hub, upstream of the 3 disks used to represent the fan. This is clearly shown in figure 6.5 (c) which shows increased radial flow at the hub upstream of the fan blading. Results from the P3DM and annular ADM demonstrate negligible radial flow in this region as a result of lacking a hub. The radial flow patterns predicted by the P3DM and annular ADM conform with the design assumption of negligible radial flow upstream of the fan. Aside from radial velocity, there is good correlation between the flow field predictions of the BS848 ADM, annular ADM and P3DM upstream of the fan in terms of axial and tangential velocities (figures 6.5 (a) and (e)). Some small deviations between the predicted flow fields are evident at the hub for the same reasons as earlier discussed. Importantly all models predict zero tangential velocity across the majority of the blade span as well as a near uniform axial velocity profile upstream of the fan. This validates the design assumptions made in Chapter 3.

Downstream of the fan the P3DM predicts no radial velocity across the majority of the blade span, as shown in figure 6.5 (d). The small radial velocity present near the hub could be the result of the design technique used in Chapter 3 being non-free vortex, or a local flow disturbance. This will be further investigated later on. In general, however the lack of radial flow validates the design assumption of negligible radial flow occurring in the fan blading. The annular ADM and BS848 ADM also predict near zero radial flow at the same plane. Given the radial flow shown upstream of the fan by the BS848 ADM (figure 6.5 (c)), this is highly unlikely and highlights the inability of the ADM to predict radial flow. This is of concern when considering the ADM as a design tool as radial flow and the energy it introduces into the flow field will not be accounted for. This failing of the ADM is well documented and authors such as Louw (2015) and Van der Spuy (2011) have attempted to address this issue,

with limited success. The annular ADM does however provide more certainty in this regard as it is subjected to the same inflow conditions as the P3DM. In terms of downstream axial and tangential velocities, the results from all three models correlate reasonably well with the designed flow field, as can be seen in figures 6.5 (b) and (f). The difference between the axial velocity profile predicted by the BS848 ADM and the design values is largely explained by the distorted inlet axial velocity profile shown in figure 6.5 (a). All models predict lower than design values for axial velocity near the blade tip. This may be as a result of wall effects, or inaccuracies in the aerofoil data used in Chapter 3 at the Reynolds numbers present in this region.

Figure 6.5 (f) shows that all models predict slightly higher than designed tangential velocities, especially near the blade tip. In the case of the BS848 ADM this is likely as a result of inflow conditions, as the aerofoil data used in the design method and ADM is the same. The discrepancies between the tangential velocity predicted by the annular ADN and P3DM and the design data indicates that the aerofoil data used by the ADM and design method may be inaccurate, as the P3DM and annular ADM inflow conditions closely match the design assumptions. In general, however the downstream axial and tangential velocities predicted by the three numerical models correlate strongly enough with the design values to consider the design method presented in Chapter 3 valid.

Figure 6.6 shows inlet and outlet flow angles predicted by the BS848 ADM, annular ADM and P3DM compared to the designed inflow and outflow angles. The angles shown correspond with those shown in figure 3.3 and are calculated by means of trigonometric relations derived from the velocity triangles shown in figure 3.3. Additionally a comparison of aerofoil angle of attack distribution is shown, as well as a comparison of Euler specific work distributions. In this case Euler specific work is defined as:

$$W_{Euler}(r) = \omega(r_2 c_{\theta 2}(r) - r_1 c_{\theta 1}(r)) \quad [J/kg] \tag{6.1.1}$$

For purposes of this study it is assumed that radial flow is negligible resulting in equation 6.1.1 simplifying to:

$$W_{Euler}(r) = \omega r(c_{\theta 2}(r) - c_{\theta 1}(r)) \quad [J/kg] \tag{6.1.2}$$

The relative flow angles β_1 and β_2 predicted by the numerical models correlate strongly with the designed relative flow angles, as shown in figure 6.6 (a) and (b). This indicates that the relationship between inlet and outlet relative velocities is correct, as well as indicating a good correlation between design and numerical relative velocity vectors. Additionally these results show that the numerical simulations predict similar blade loading to the designed blade loading, further validating the design procedure.

The inlet absolute flow angle (α_1) distributions predicted by the numerical models are compared to the design distribution of α_1 in figure 6.6 (c). It can
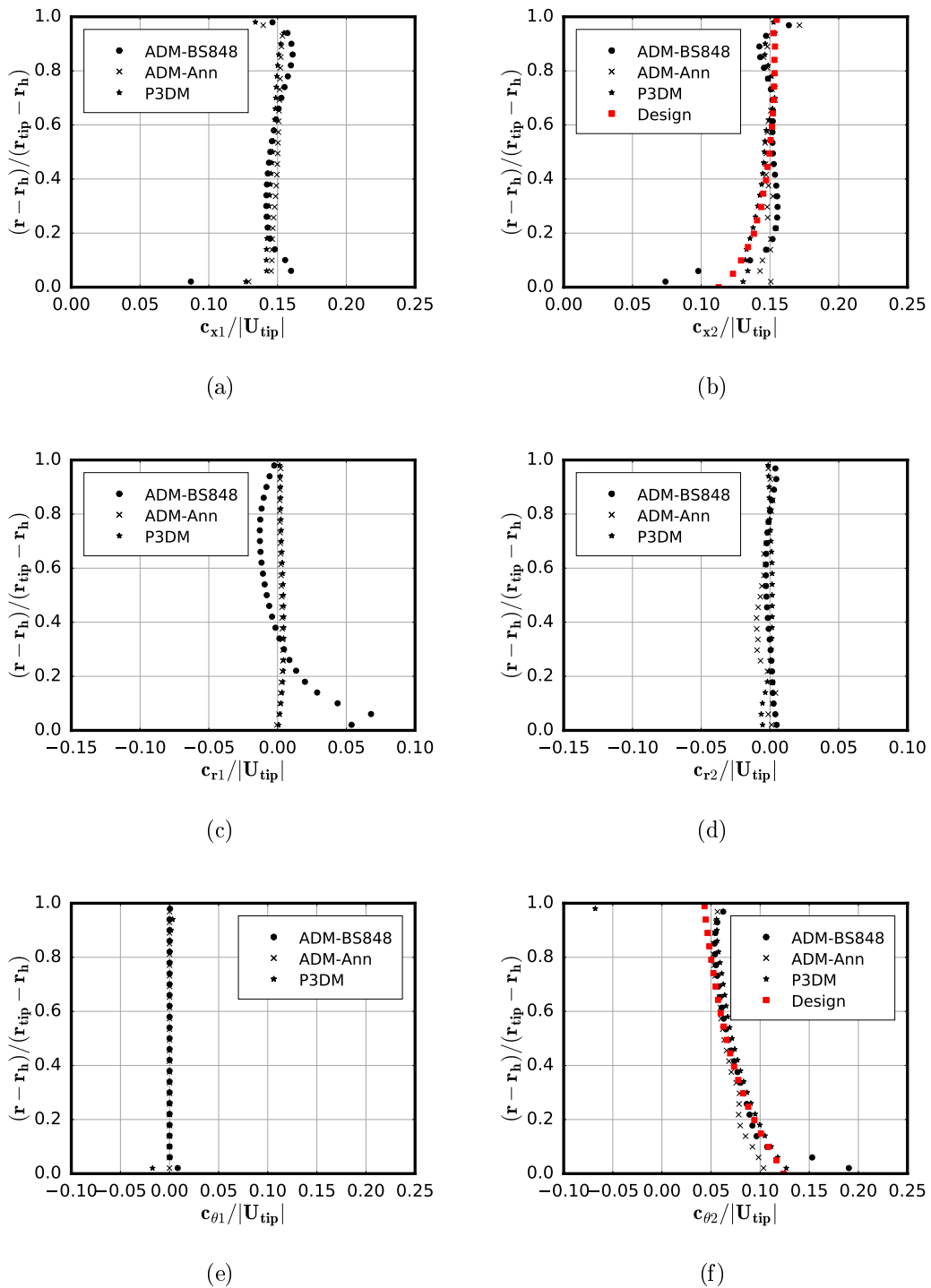
(a)

(b)

(c)

(d)

(e)

(f)

Figure 6.5: Comparison of velocity data between ADM and P3DM results at the inlet (L) and outlet (R) ($333\,\mathrm{m}^3/\mathrm{s}$)

be seen that the numerically produces data sets correlate excellently with the design data. This indicates that there is little to no swirl upstream of the fan across the majority of the blade span, in line with design assumptions. The numerically predicted outlet absolute flow angles (α_2) differ significantly from the design values, especially towards the blade tip, as shown in figure 6.6 (d). In general the values predicted by the BS848 ADM and P3DM are higher than the design values. This is as a result of the deviation in outlet tangential velocity from the designed vortex, as previously discussed and shown in figure 6.5 (f), as well as differences in outlet axial velocity profiles (figure 6.5 (b)). It can be seen that the outlet absolute flow angle predicted by the annular ADM is significantly lower than the design angle at the blade root, again as a result of deviations in tangential velocity at the outlet.

Figure 6.6(e) shows the designed angle of attack distribution compared to the angle of attack distributions obtained from the ADM models and P3DM. It can be seen that the numerical data correlates well with the design data. The designed angle of attack distribution is not as smooth as the numerically predicted distributions. This is as a result of the optimisation processes using 21 individual blade sections for camber optimisation. This differs from reality where the fan is one continuous blade section. The BS848 ADM under predicts angle of attack near the blade root and the annular ADM over predicts angle of attack in the same region. This is as a result of inflow distortions, as shown in figure 6.5 (a)

The Euler specific work distributions shown in figure 6.6 show that the numerical simulations both predict more work being done by the blade, especially in the tip half of the blade, than the design Euler specific work distribution. Equation 6.1.2 shows that Euler specific work is a function of tangential velocity distribution, and blade velocity distribution. As blade velocity increases along the blade span ($u(r) = \omega_F r$), tangential velocity distribution has a more significant impact on specific work at larger radii. Although both numerical models predict zero tangential velocity at the inlet, both higher than design tangential velocities at the outlet, especially towards the blade tip (see figure 6.5 (f)).The difference between the design and numerically predicted tangential velocities is small, however the increase in blade velocity with radius results in a significant increase in numerically predicted specific work done by the blade. The reduced outlet tangential velocity produced by the annular ADM results in lower specific work at the blade root. This is likely the cause of the lower fan total-to-static pressure estimate provided by this model.

The results presented in this section show that the design method presented in Chapter 3 and the assumptions therein are valid, both in terms of fan performance and flow field. It has also been shown that the ADM used to model the M-fan is valid for the range of flow rates considered. The ADM is also demonstrated to be capable of predicting the flow field in the vicinity of the M-fan blading with reasonable accuracy, and thus would be appropriate for further use in modelling the M-fan.
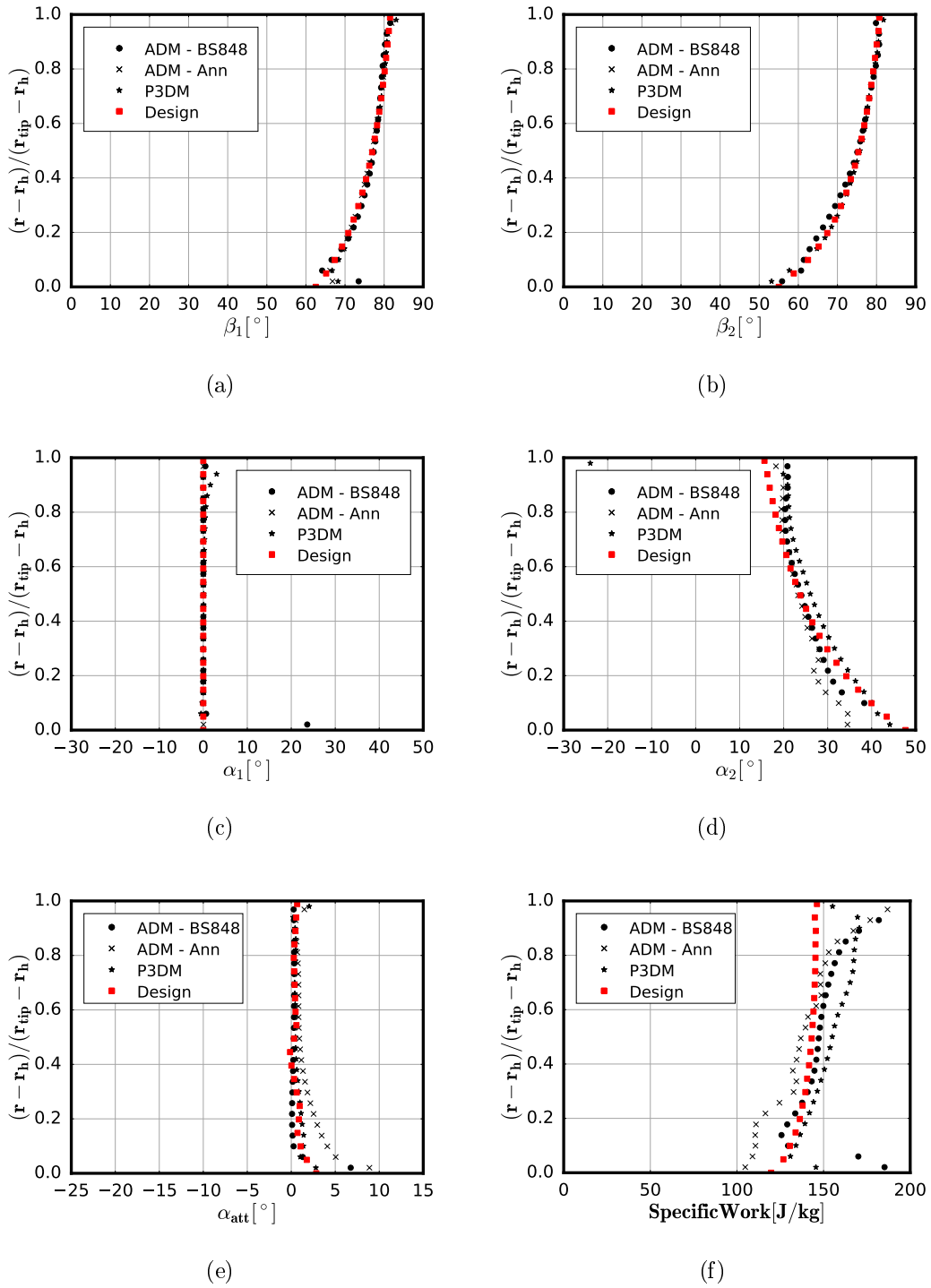
Figure 6.6: Comparison of flow angle and work data between ADM and P3DM results and the designed flow field for relative flow angles β_1 (a) and β_2 (b), absolute flow angles α_1 (c) and α_2 (d), angle of attack (e) and Euler specific work (f) at the operating point $(333\,\text{m}^3/\text{s})$

6.2   M-Fan Performance Analysis

The results presented so far consider the M-fan operating under theoretical conditions, with no tip gap. In reality the M-fan will have to be run with a tip gap, which according to literature will result in a loss in fan performance and alter the flow field in the vicinity of the blades. Additionally the flow field up until now has only been modelled at the design flow rate, $333\,\mathrm{m^3/s}$. Literature presented in Chapter 2 indicates that off design performance is of importance in fans used in air-cooled heat exchangers. In this section two additional versions of the P3DM are used to generate fan performance and flow field data at two different tip clearances. One models the M-fan with the tip gap recommended by the design specifications, $0.03\,\mathrm{m}$, and the other models the M-fan with a reduced tip gap of $0.015\,\mathrm{m}$. The results from these two models are compared to results generated using the zero tip gap P3DM at a selected range of flow rates, $265\,\mathrm{m^3/s}$ to $385\,\mathrm{m^3/s}$, both in terms of fan performance and flow field. This aims to quantify the performance loss due to tip clearance, as well as understanding the flow mechanisms behind these losses. These steps aim to critically assess the performance of the M-fan under various conditions, as well as providing potential remedial steps to improve the design process in the future.

6.2.1   M-fan Performance Characteristics

It has already been shown in the previous section that the M-fan meets design specifications in terms of total-to-static pressure and efficiency, with no tip gap. It has also been shown that the M-fan has a steep enough total-to-static pressure characteristic to be considered suitable for its desired application in air-cooled heat exchangers. Literature surveyed in Chapter 2 indicates that fan performance in terms of total-to-static pressure and efficiency as well as fan power is reduced with increasing tip gap. This section aims to gauge these performance losses, as well as the effect of reducing tip gap on the performance of the M-fan.

Figure 6.7 shows the fan total-to-static pressure characteristics for the M-fan operating, with no tip gap, the design tip gap and a reduced tip gap. It can be seen that increasing the tip gap significantly reduces the total-to-static pressure rise across all flow rates surveyed, in line with literature. At the design flow rate ($333\,\mathrm{m^3/s}$) the performance of the M-fan is reduced by 20% compared to the zero tip gap model when it is modelled with the tip gap recommended by the design specifications, $0.03\,\mathrm{m}$. Reducing the tip gap to $0.015\,\mathrm{m}$ reduces this loss in pressure to 9.2%. These losses remain fairly constant throughout the range of flow rates modelled, in line with the findings of Venter and Kröger (1992) and Wilkinson and Van der Spuy (2015). It is also important to note that the introduction of a tip gap does not affect the gradient of the pressure characteristic curves. The losses incurred in total-to-static pressure are largely
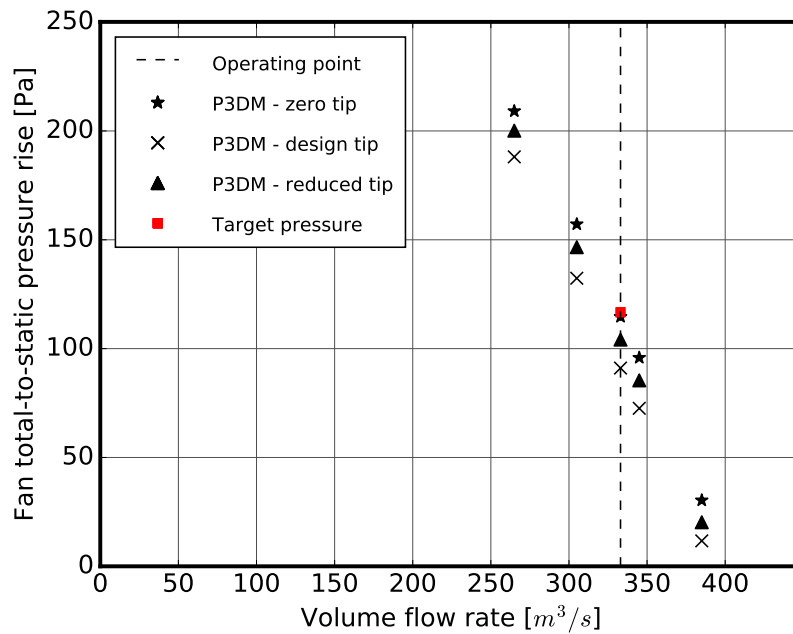
Figure 6.7: Fan total-to-static pressure vs volume flow rate for the M-fan with varying tip gaps

due to tip leakage flow, and its effect on the flow through the fan blading. This will be investigated later in the next sections of this chapter. A similar trend can be observed in terms of fan total-to-static efficiency, as shown in figure 6.8. Efficiencies obtained at all flow rates are reduced with increasing tip gap. Unlike the reductions in total-to-static pressure with tip gap, as seen in figure 6.7, the reduction in total-to-static efficiency is not constant across the flow rates surveyed. At the design flow rate, with the tip gap of 0.03 m the M-fan attains a total-to-static efficiency 7.9 % lower than without a tip gap. With a reduced tip gap the loss in efficiency is lowered to 3.6 %. It can be seen in figure 6.8 that this loss in efficiency decreases at lower flow rates and increases at higher flow rates.

The non-constant reduction in total-to-static efficiency due to tip gap for the flow rates surveyed can be attributed to fan power losses, depicted in figure 6.9. Again fan power is seen to decrease with increasing tip gap. The reduction in fan power becomes more severe at higher flow rates. This is in line with findings in literature and can be explained by the tip leakage effect earlier mentioned.

It is clear from the results presented in figures 6.7, 6.8 and 6.9 that tip clearance has a significant, negative impact on fan performance. With the tip clearance recommended by the design specification (0.03 m) the M-fan attains a total-to-static pressure rise of 91 Pa and a total-to-static efficiency of 51.5 %. These values are well below the specified values of 116.7 Pa and 60 %. It
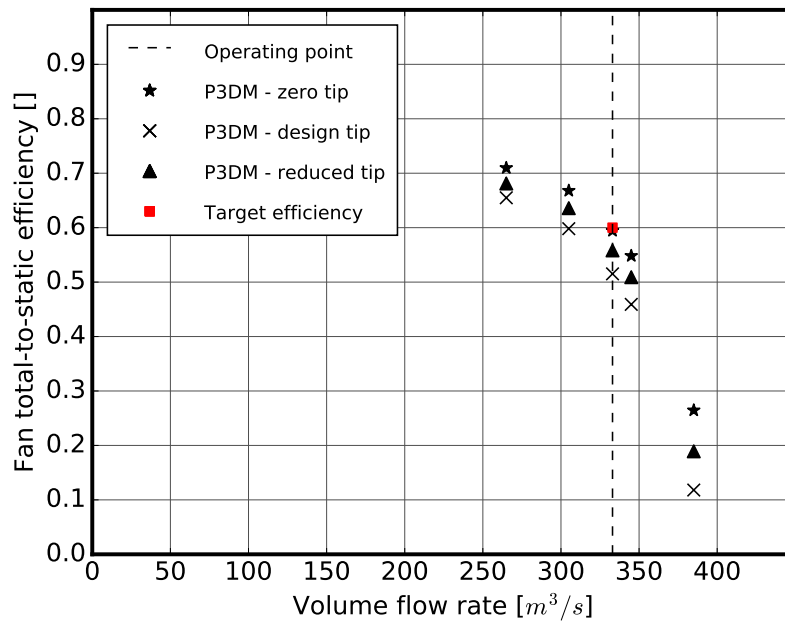
Figure 6.8: Fan total-to-static efficiency vs volume flow rate for the M-fan with varying tip gaps
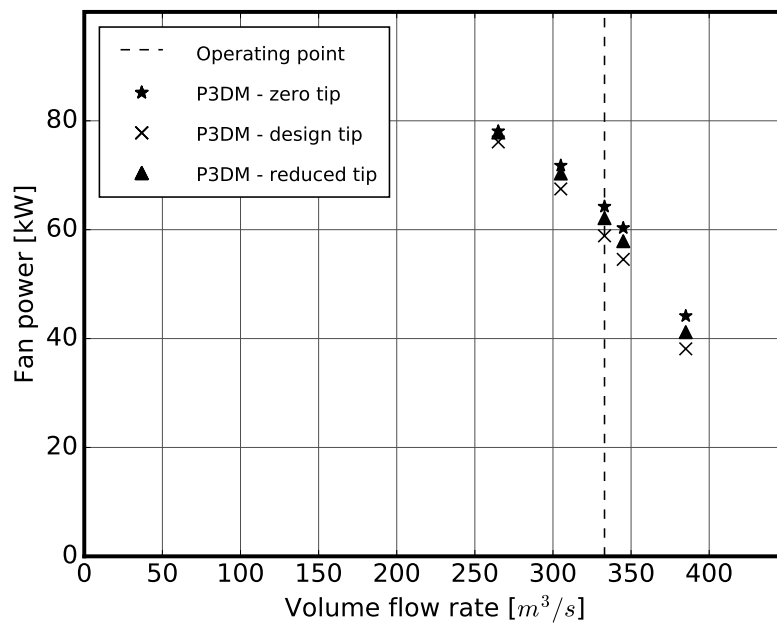

Figure 6.9: Fan power vs volume flow rate for the M-fan with varying tip gaps

is also clear that reducing tip clearance improves fan performance, moving all characteristic curves nearer the theoretical zero tip gap curves. For this reason

it is recommended that the tip gap specification in Chapter 3 be reduced by at least half, to a tip gap of 0.015 m (as shown here) or less. The flow mechanisms responsible for the losses incurred due to tip clearance will be explored in the remaining sections and other potential solutions recommended.

6.2.2 M-fan Spanwise Flow Field Characteristics

The relative inlet and outlet velocities, relative flow angles and absolute flow angles as defined in figure 3.3 are presented for flow rates of $265\,\mathrm{m^3/s}$, $333\,\mathrm{m^3/s}$ and $385\,\mathrm{m^3/s}$. Additionally angle of attack and Euler specific work distributions, as defined in equation 6.1.2, are also presented. In each case data generated by the P3DM with zero tip gap is compared to the reduced tip gap and design tip gap cases in order to ascertain whether the inclusion of a tip gap has an effect on spanwise flow field characteristics. These results also aim to demonstrate how the flow field in the vicinity of the M-fan changes with flow rate. The data presented here is extracted from the same points described in figure 6.4.

Figures 6.10, 6.11 and 6.12 depict the average axial, radial and tangential flow components of the M-fan upstream and downstream of the blading for flow rates of $265\,\mathrm{m^3/s}$, $333\,\mathrm{m^3/s}$ and $385\,\mathrm{m^3/s}$. Considering these three figures at a glance a few general trends are apparent. Axial velocity increases with flow rate, while outlet tangential velocity decreases. This is in line with expectation as axial velocity is associated with volume flow rate and change in tangential velocity is associated with total-to-static pressure rise. It can be seen that at each flow rate the inlet tangential velocity is zero for the majority of the blade span, in line with design assumptions. The shape of the outlet tangential velocity profile is observed to be similar for all flow rates, as a result of the blade twist and lift coefficient distributions developed in Chapter 3. It is also observed that at each flow rate the inlet axial velocity profile is uniform. Both inlet and outlet radial velocity are observed to increase with decreasing flow rate, in line with literature such as the work of Louw (2015). Figures 6.10, 6.11 and 6.12 (b) and (f) show that increasing tip gap decreases tangential velocity across the majority of the blade span and increases axial velocity in the same areas. The outlet tangential velocity is decreased by an average of 5 % for a reduced tip gap of 0.015 m and 10 % for the design tip gap of 0.03 m across all flow rates. A decrease in outlet tangential velocity explains in part the performance loses encountered when increasing the tip gap.

Considering the outlet velocity components at a flow rate of $265\,\mathrm{m^3/s}$, shown in figure 6.10 (b), (d) and (c) it is clear that the flow has been disturbed near the blade root. The outlet axial velocity component shown in figure 6.10(b) is severely reduced at the blade root, with a small amount of back flow occurring near the hub. Radial and tangential velocity components also experience sharp reductions in magnitude near the hub, as seen in figure 6.10 (d) and (f). These reductions in velocity indicate that flow separation is likely

to have occurred, creating a low velocity region downstream of the blade in this region. Flow separation from the fan surface often occurs as a result of stall. Stall occurs when the angle of attack seen by a part of the fan blading exceeds the angle of attack which yields maximum lift, resulting in flow separation from the suction side of the aerofoil surface. This effect is described in more detail in Chapter 2 and illustrated in figure 2.4. According to literature presented in Chapter 2, stall usually first occurs near the hub, propagating radially along the blade with decreasing volume flow rate. This is in line with what can be seen in figure 6.10 (b), (d) and (f). Another possible reason for flow separation could be flow separating from part of the aerofoil section used near the blade root due to the geometry of the aerofoil. The aerofoil section used at the hub of the M-fan is an aerofoil based on the NASA LS 0413 section, however the aerofoil is modified to have a camber of 3.5 %. This results in the the suction side of the aerofoil having more curvature that the unmodified profile, leading to the possibility of the flow separating from the trailing edge at higher angles of attack. It is also noted that tip gap has an influence on the severity of this flow separation, with larger tip gaps resulting in less dramatic decreases in velocity magnitude, as shown in figure 6.10 (b), (d) and (f).

The influence of tip gap on the spanwise flow fields upstream and downstream is most obvious in the blade tip region. This is especially apparent in terms of the axial velocity component, where the axial velocity magnitude in the tip region upstream and downstream of the fan is reduced with increasing tip gap. This effect is visible in figures 6.10, 6.11 and 6.12 (a) and (b). A reduction in axial velocity at the tip leads to the the earlier mentioned increased axial velocity across the rest of the blade span, in order to satisfy continuity. A similar effect can also be seen in the outlet tangential velocity component, where the outlet tangential velocity reduces with increasing tip gap across all flow rates (see figures 6.10, 6.11 and 6.12 (f)). This is as a result of the tip leakage effect, where flow is drawn through the tip gap from the high pressure region on the pressure side of the blade to the low pressure region on the suction side. This effect is also evident in terms of radial flow as outward radial flow increases towards the tip gap at the blade outlet with increasing tip gap. Similarly inward radial flow increases at the inlet. It is also evident that the magnitude of radial flow near the blade tip increases with tip gap and decreasing flow rate, as shown in figures 6.10, 6.11 and 6.12 (c) and (d). These leakage effects result in a pressure loss being incurred at the blade tip. This loss coupled with the earlier mentioned spanwise reduction in tangential velocity accounts for the deterioration in total-to-static pressure rise, as shown in figure 6.7.

Figure 6.13 compares the relative and absolute flow angles defined in figure 3.3 at volume flow rates of $265\,\mathrm{m^3/s}$, $333\,\mathrm{m^3/s}$ and $385\,\mathrm{m^3/s}$. Considering inlet and outlet relative flow angles β_1 and β_2, it is evident that the spanwise distribution of β_2 remains relatively constant across the flow rates shown. The relative flow angle β_1 increases with decreasing flow rate, especially near the

Figure 6.10: Comparison of M-fan velocity data with zero tip gap (ZT), design tip gap (DT) of $0.03\,\mathrm{m}$ and reduced tip gap (RT) of $0.015\,\mathrm{m}$ at the inlet (L) and outlet (R) at $265\,\mathrm{m}^3/\mathrm{s}$

Figure 6.11: Comparison of M-fan velocity data with zero tip gap (ZT), design tip gap (DT) of $0.03\,\mathrm{m}$ and reduced tip gap (RT) of $0.015\,\mathrm{m}$ at the inlet (L) and outlet (R) at $333\,\mathrm{m^3/s}$

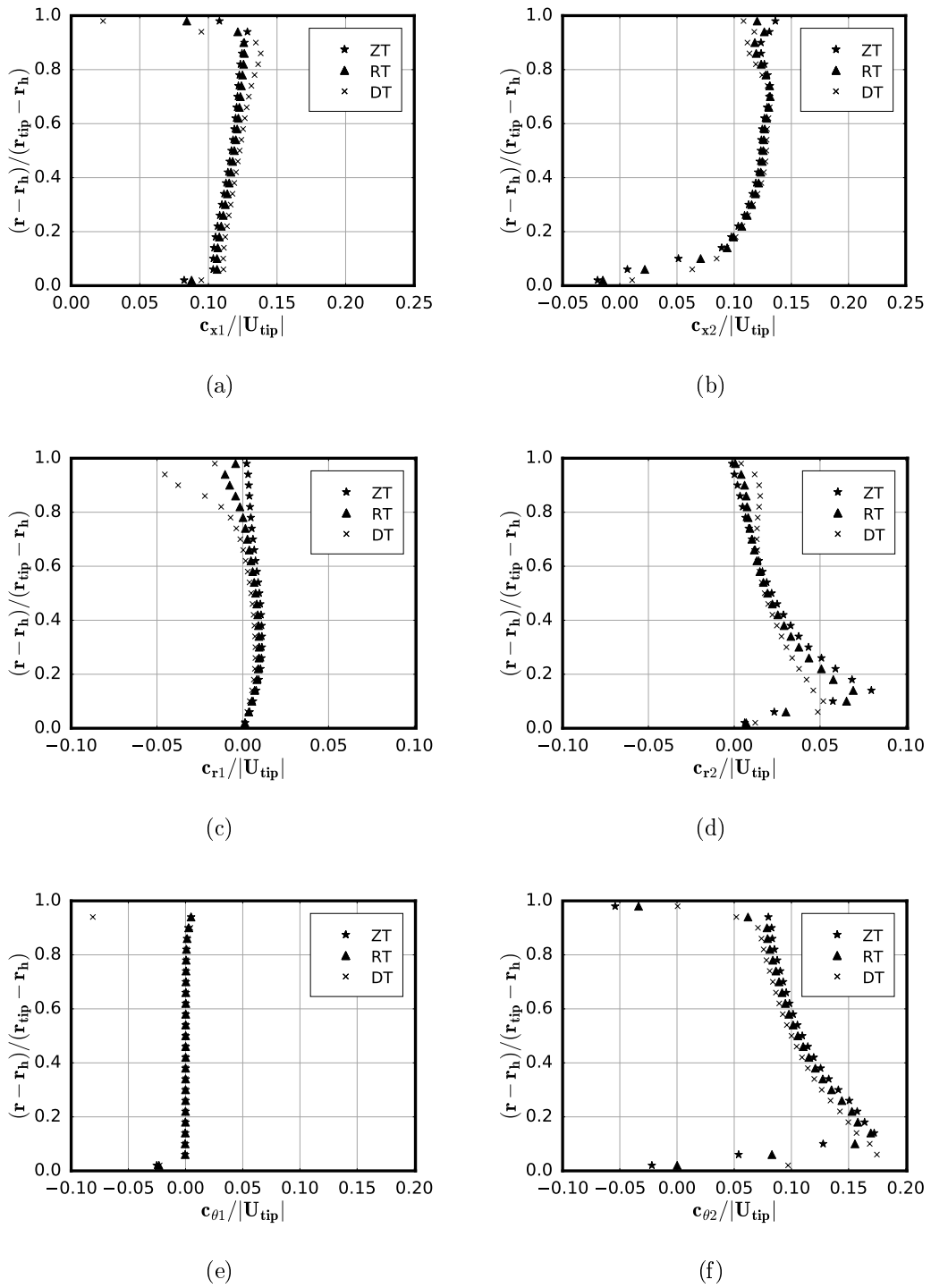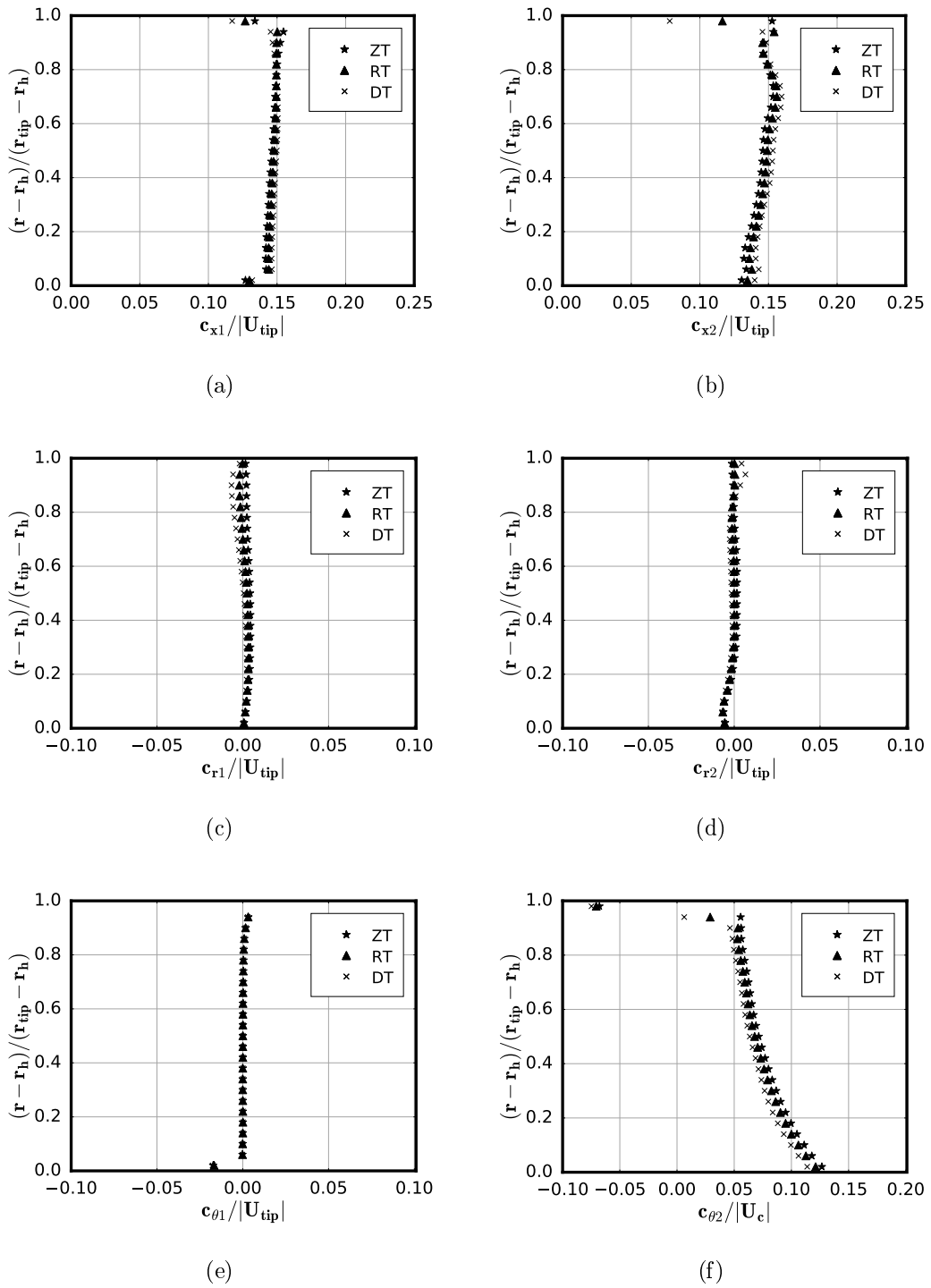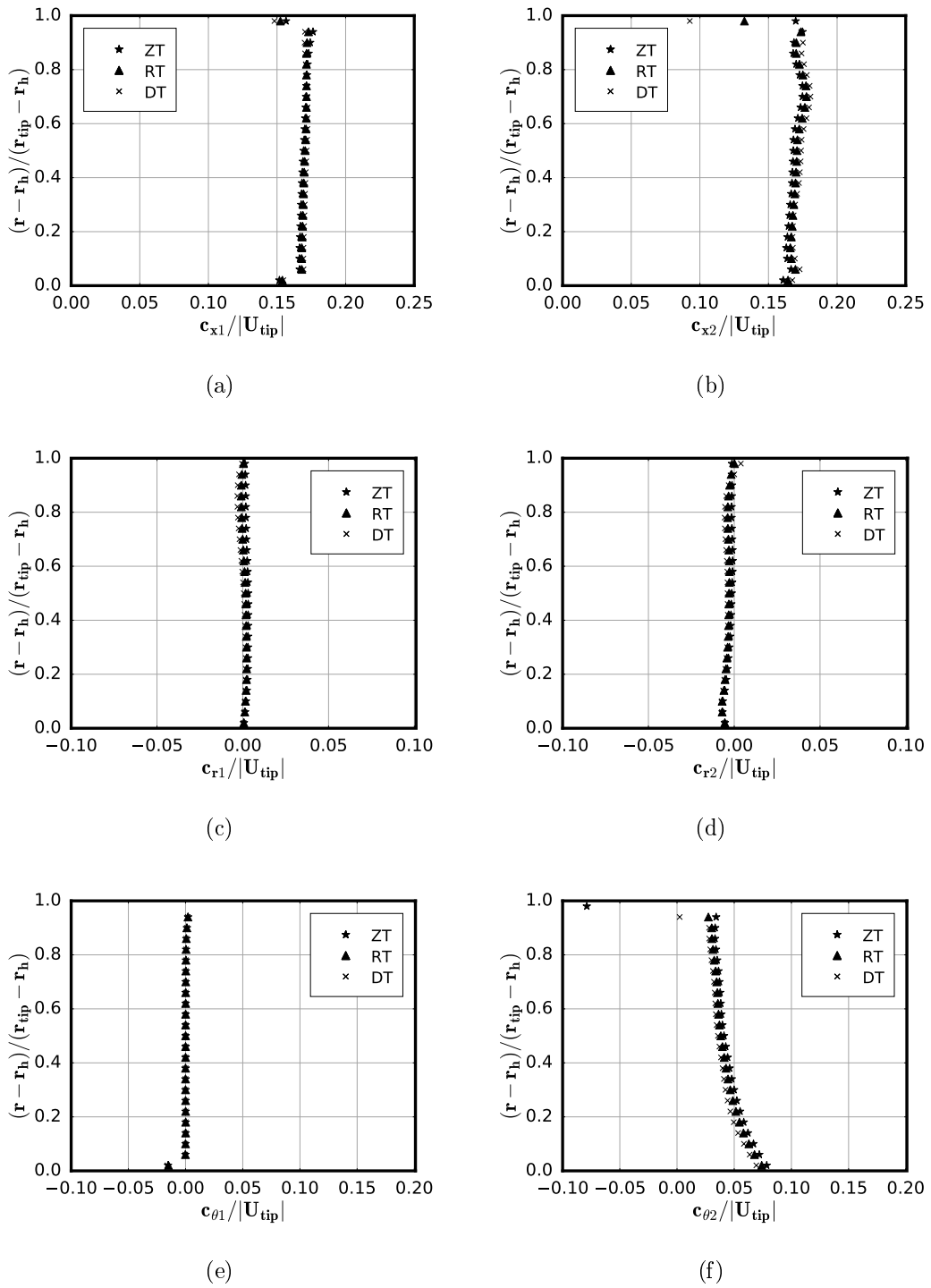Figure 6.12: Comparison of M-fan velocity data with zero tip gap (ZT), design tip gap (DT) of $0.03\,\mathrm{m}$ and reduced tip gap (RT) of $0.015\,\mathrm{m}$ at the inlet (L) and outlet (R) at $385\,\mathrm{m^3/s}$

blade root. Figure 6.13 also shows that the difference between β_1 and β_2 is very small nearer the blade tip, indicating that the blade is lightly loaded in this region at the flow rates depicted. The difference between β_1 and β_2 increases towards the hub indicating higher blade loading. It is also clear that the more of the blade becomes loaded at lower flow rates, due to changing inflow conditions resulting in a larger flow turning angle across more of the blade span. The flow separation effect visible in figure 6.10 is also evident in 6.13 (a), where near the hub there is a sharp increase in angle β_2. It can be seen that values of β_2 exceed the β_1 angles at this point, indicating that little to no work is being done here.

The effect of tip clearance on relative flow angles appears to be negligible for the majority of the blade span for the three flow rates considered in figure 6.13. Tip gap appears to have a small effect on β_2 at the blade tip, increasing the angle with increasing tip gap. Tip gap also appears to have an influence on β_2 where flow separation occurs. Figure 6.13 (a) shows that for larger tip gaps, the increase in β_2 is smaller, likely due to the higher axial velocities observed for larger tip gaps.

Considering the absolute flow angles α_1 and α_2 depicted in figure 6.13, it is clear that α_1 remains relatively constant, whilst α_2 decreases with increasing flow rate. For the majority of the blade span at the flow rates shown $\alpha_1 = 0°$ in line with the design assumption of no inlet swirl. However α_1 near the blade tip increases slightly with decreasing flow rate. Angle α_1 appears to be unaffected by the tip gap. Contrary to this, the tip gap has an influence on α_2, decreasing the angle with increasing tip gap. This is due to the effect of the tip gap on outlet tangential velocity, as earlier discussed. The design tip gap results in an average reduction in α_2 of 2.75° and the reduced tip gap results in the angle being 1.7° smaller than for the M-fan with no tip gap, at a volume flow rate of $385\,\mathrm{m}^3/\mathrm{s}$. At a lower volume flow rate of $265\,\mathrm{m}^3/\mathrm{s}$ the average reduction is angle increases to 3.8° and 1.8° respectively, for the M-fan running at with the design tip gap and reduced tip gap.

The spanwise angle of attack and Euler specific work distributions for the M-fan are depicted in figure 6.14. A sharp increase in angle of attack as well as the sharp decrease in specific work for the blade root seen in figure 6.14 (a) indicates that this portion of the blade is indeed stalled. The angle of attack seen by this portion of the blade exceeds the critical angle of attack ($\approx 13°$). This means that at volume flow rates lower than $265\,\mathrm{m}^3/\mathrm{s}$ stall will occur across an increasing part of the blade span, reducing total-to-static efficiency. It is also evident in figure 6.14 that increasing flow rate decreases both specific work and angle of attack.

Tip gap effects are evident for both the angle of attack and specific work distributions shown in figure 6.14. For angle of attack increasing the tip gap increases the angle of attack seen at the blade tip. Angle of attack reduces with increasing tip gap for the rest of the blade span, although for the flow rates considered this reduction is never more than 0.5° from the zero tip gap values.
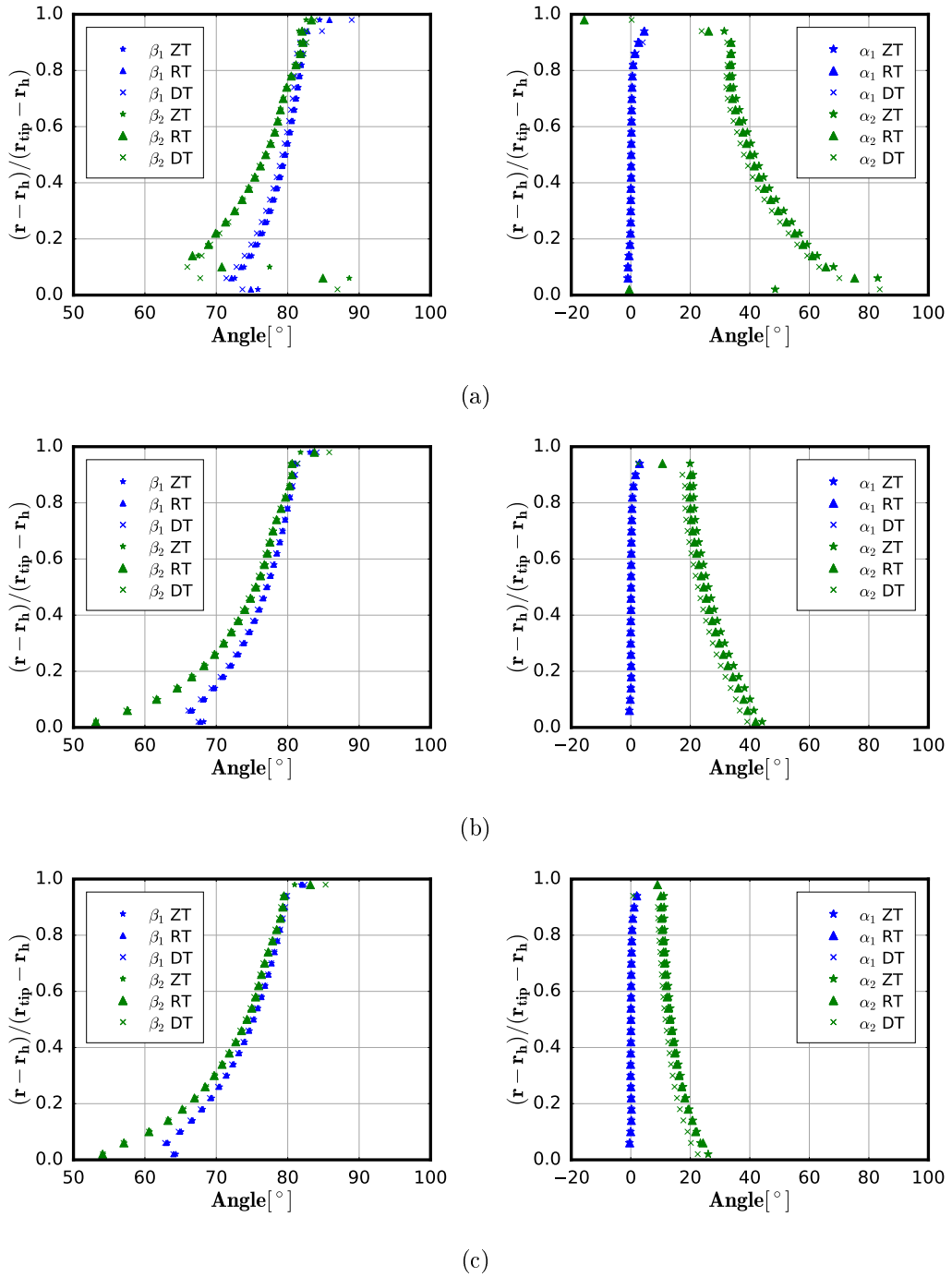
Figure 6.13: Comparisons of relative flow angles β_1 and β_2 (L) and absolute flow angles α_1 and α_2 for the M-fan with zero tip gap (ZT), design tip gap (DT) of $0.03\,\mathrm{m}$ and reduced tip gap (RT) of $0.015\,\mathrm{m}$ at flow rates of $265\,\mathrm{m^3/s}$ (a), $333\,\mathrm{m^3/s}$ (b) and $385\,\mathrm{m^3/s}$ (c).
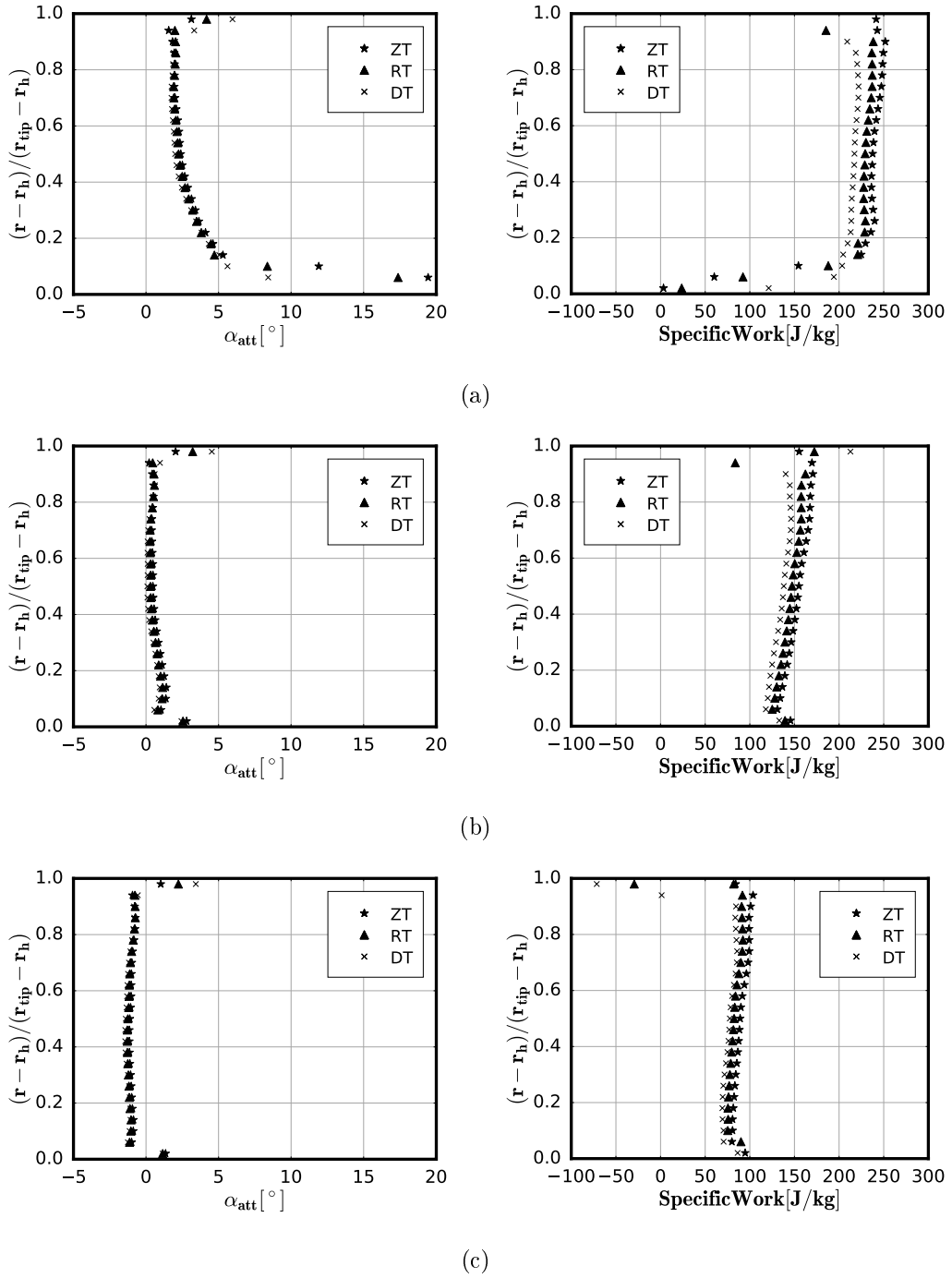
Figure 6.14: Comparisons of angle of attack (L) and Euler specific work distri-bution for the M-fan at flow rates of $265\,\mathrm{m^3/s}$ (a), $333\,\mathrm{m^3/s}$ (b) and $385\,\mathrm{m^3/s}$ (c).

The Euler specific work distribution is strongly effected by increasing the tip gap. Figure 6.14 shows that specific work across the blade span decreases with increasing tip gap at the flow rates considered. The magnitude of this reduction in specific work increases with decreasing volume flow rate. In all cases the magnitude of specific work at the blade tip decreases with increasing tip gap, to the point of becoming negative and therefore constituting a loss. In the case of figure 6.14 (a)and (b) these loses are too large to be shown on the plots without the rest of the data losing some of its meaning. Reducing the tip gap, however,is shown to reduce the losses encountered here.

The results obtained here indicate that tip gap effects have an influence on the flow structure over the entire blade span, with a loss in total-to-static pressure resulting from a reduction in outlet tangential velocity. A potential solution is to increase the blade angle until the correct total-to-static pressure rise is obtained at the design volume flow rate. While effective, this solution would also increase angle of attack, reducing stall margin. A more scientific approach would be to account for the increase in through flow velocity and decrease in outlet tangential velocity, as a result of tip loses, at the design stage. Features such as end plates could also be incorporated to mitigate these losses, in line with findings in literature.

6.2.3 M-fan Tip Gap Flow Field

In order to provide more insight into the tip leakage effect figure 6.15 depicts the velocity relative to the M-fan blade at the blade tip span and at a span halfway between the blade tip and shroud at the design flow rate $(333\,\mathrm{m^3/s})$ for both the design tip gap $(0.03\,\mathrm{m})$ and reduced tip gap $(0.015\,\mathrm{m})$. Figure 6.15 also includes pathlines in order to depict the flow structures at these two spans. Considering the design tip gap and reduced tip gap at the blade tip span, it is apparent that the flow structures are similar for both cases. The relative velocity magnitudes up and downstream of the fan blade are near identical, with velocity magnitude downstream decreasing. There is evidence of tip leakage flow in both cases, with flow leaking over the rear two thirds of the blade tip with a tip gap of $0.03\,\mathrm{m}$ and over the rear half of the blade with a tip gap of $0.015\,\mathrm{m}$. In both cases a tip leakage vortex structure is visible, initiating on the suction side of the blade, with the larger tip gap producing a larger tip vortex, indicating higher losses.

In the case of the mid-span between the blade tip and the shroud, the vortex structure observed for the larger tip gap depicted in figure 6.15 (a) is larger than that for the smaller tip gap shown in figure 6.15 (b). The boundary layer on the blade tip is also evident in the reduced tip gap case as a low velocity region. Although the pathlines indicate that flow does cross this region, the leakage is not as severe as that depicted for the design tip gap case. The velocity difference at the mid span of the tip gap in the design tip gap case is also smaller than in the reduced tip gap case, indicating that reducing the tip
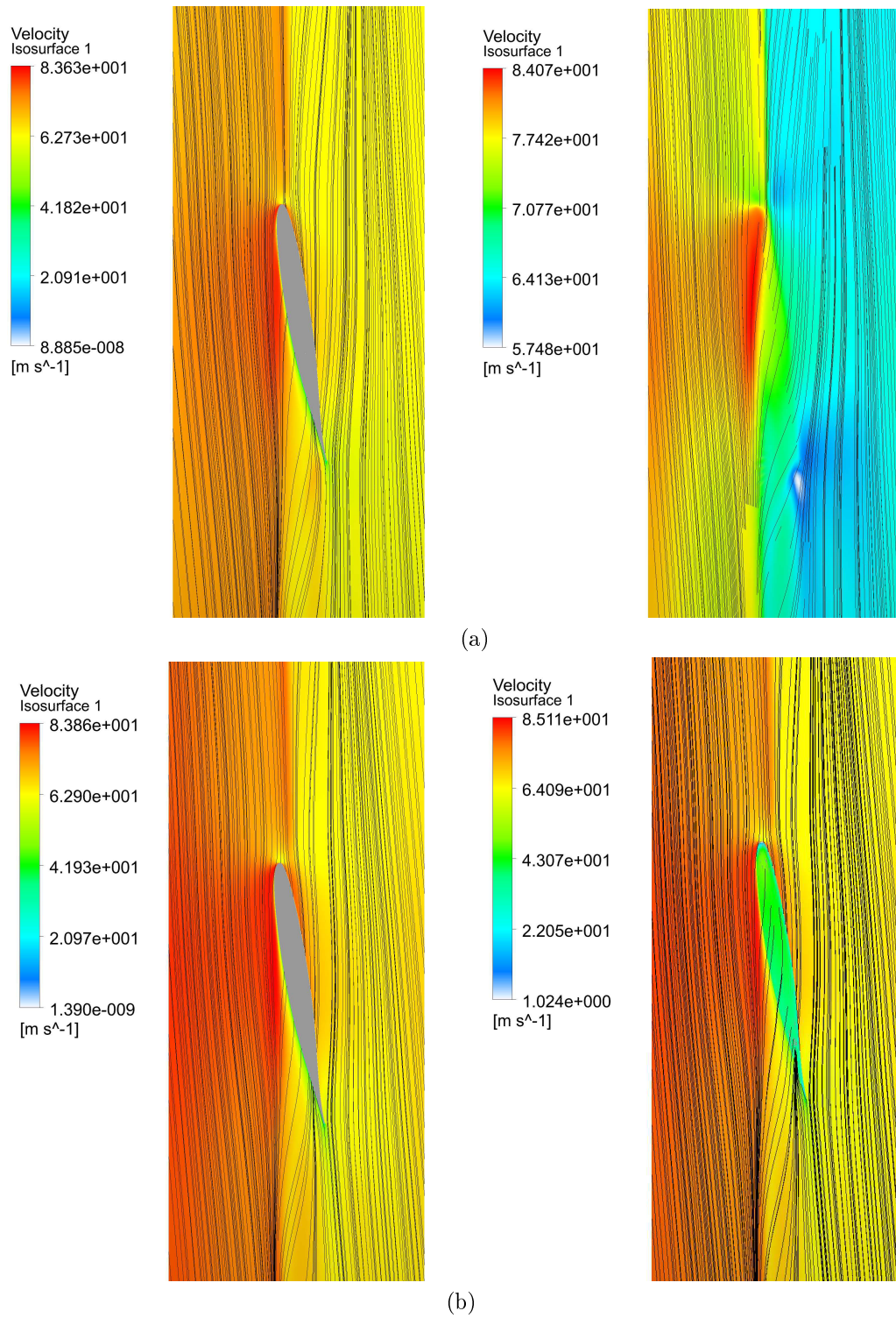
Figure 6.15: Contours of velocity relative to the fan blade with path lines shown for radial surfaces at the blade tip (L) and for the middle of the tip gap (R) for the M-fan with the design specified tip gap of 0.03 m (a) and a reduced tip gap of 0.015 m (b).

gap lowers the pressure loss incurred due to tip effects, in line with the results shown in figure 6.7.

These results show that reducing tip clearance impacts leakage flow by extending the influence of the blade tip boundary layer across more of the tip gap. While not eliminating tip losses, the losses are reduced. Significantly the tip leakage vortex size and intensity is also reduced. Literature such as the study of Corsini *et al.* (2007) suggests that the leakage vortex is a significant noise source, there reducing this vortex should have a positive impact on fan noise. Based on these results it is possible to conclude that the tip gap specified for the M-fan in Chapter 3 is too large, and that the tip gap should be reduced in order to improve fan performance. Tip modifications may also be considered in order to mitigate these effects.

6.2.4   M-fan Blade Surface Flow Characteristics

Blade surface streamlines are shown in figure 6.16 for the M-fan running with a tip clearance of 0.015 m. The stream lines presented in figure 6.16 correspond with volume flow rates of $265 \, \text{m}^3/\text{s}$ (a), $333 \, \text{m}^3/\text{s}$ (b) and $385 \, \text{m}^3/\text{s}$ (c). In all three cases there is radial flow present on the suction side of the blade, near the trailing edge at the hub. This flow becomes more severe as the volume flow rate reduces. This is of particular concern at the design flow rate shown in figure 6.16 (b) and the higher flow rate depicted in figure 6.16 (c), as the flow should move circumferentially across the blade surface as it does at the midspan. In both cases angle of attack data (see figure 6.14) indicates that the blade is not in stall at any point along the blade span. Similar radial flow can be observed in the same region on the pressure side of the blade in figure 6.16 (b) and (c). The likely cause of this flow effect is the camber optimisation, which results in more aerofoil camber at the blade root. This results in more curvature on the suction side of the fan blade, especially near the blade root. The results shown here indicate that the curvature of the aerofoil suction side surface near the blade root, results in a small amount of flow separation at this region and radial flow above it.

A similar effect can be observed on the pressure side of the M-fan blade at a flow rate of $265 \, \text{m}^3/\text{s}$ (figure 6.16(a)). Here flow propagates radially away from the hub, before clearing the trailing edge where both the camber and twist are reduced as shown in figure 3.4. The aerofoil section used near the hub has a concave shape near the trailing edge. This creates a channel which appears to funnel the flow upwards at this flow rate.

Both of the flow patterns discussed so far are undesirable as they are likely to result in pressure losses in this region of the blade, leading to a loss in fan performance. This calls into question the suitability of the NASA LS 0413 profile for the camber optimisation carried out in Chapter 3. Future work should consider the possibility of using a different aerofoil section for the lower third of the blade, if not the whole blade. Ideally the suction surface needs

(a)

(b)

(c)
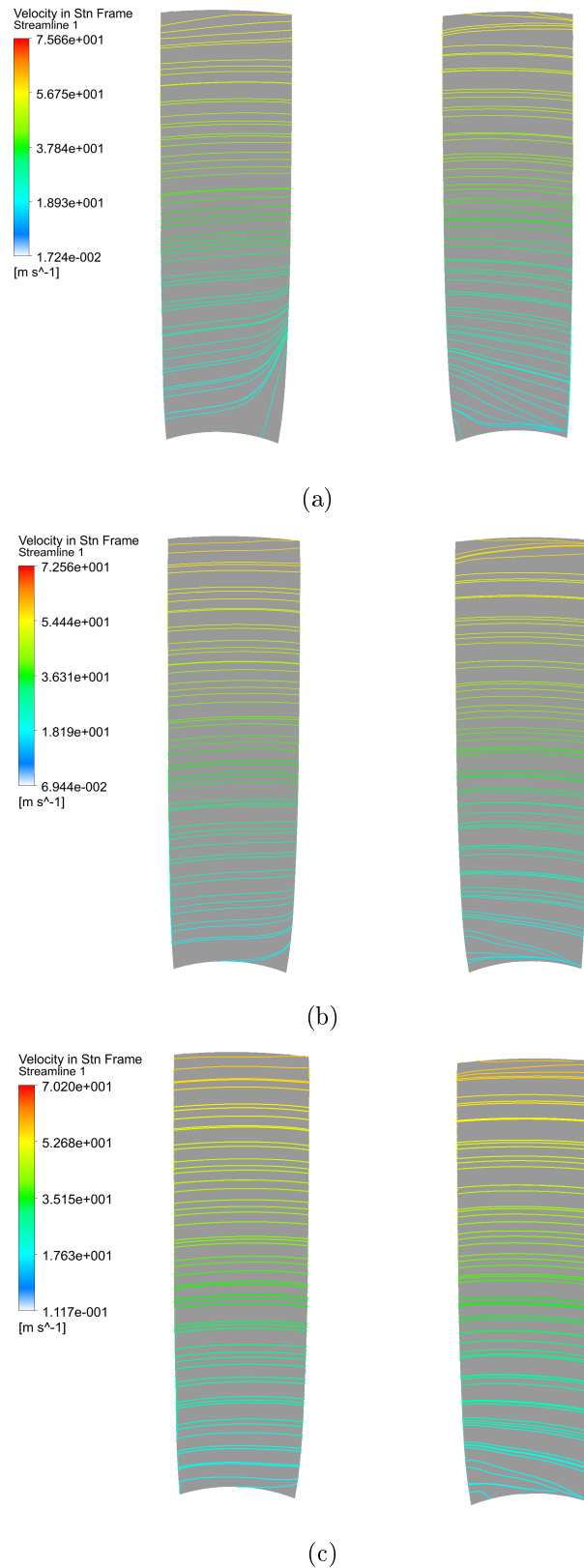
Figure 6.16: Surface streamlines on the pressure side (L) and suction side (R) of the M-fan running with a reduced tip gap of $0.015\,\mathrm{m}$ at $265\,\mathrm{m^3/s}$ (a), $333\,\mathrm{m^3/s}$ (b) and $385\,\mathrm{m^3/s}$ (c).

to be less curved than at present and the concave section of the pressure side near the trailing edge should be eliminated. This will help ensure that the flow remains attached and ordered at the blade root, improving stall margin and fan performance. There is also some indication in literature presented in Chapter 2 that stall margin can be improved by applying forward sweep to the fan blade. This should be investigated in the future.

Chapter 7

Conclusion and Recommendations

A design procedure aimed at designing an axial flow fan for air-cooled heat exchanger applications has been developed. The method incorporates aerofoil camber optimisation in order to optimise the lift-to-drag ratio along the blade span. This procedure has been used to design the M-fan, a fan designed to the requirements of the MinWaterCSP project. The development of the design procedure was aided by use of the actuator disk model (ADM), in order to model concept designs (Appendix C). In order to validate the design method and ADM, the M-fan has been modelled by means of a periodic three dimensional CFD model (P3DM). Results from the P3DM show that the design assumptions made in Chapter 3 are valid in terms of the flow field directly upstream and downstream of blades and that the design meets performance requirements specified. The ADM used to model the M-fan, which incorporates XFOIL derived aerofoil polar data in order to account for variations in geometry and Reynolds number, has also been shown to be valid. The ADM is capable of predicting the flow field in the vicinity of the fan satisfactorily in two different domains, as well as predicting fan performance characteristics sufficient accuracy to be used in the context of modelling large air-cooled heat exchanger systems and potentially future design studies. The ADM has been shown to predict total-to-static pressure rise accurately enough to determine whether the fan meets the pressure rise required by the design specification. Additionally the pressure prediction is accurate enough to assess the gradient of the total-to-static pressure characteristic in the operating region, which is important for the application considered in this study.

Further modelling of the M-fan by means of the P3DM assesses the performance of the M-fan under more realistic conditions, with the inclusion of a tip gap. The tip gap is shown to have an influence on the performance of the M-fan, considerably reducing total-to-static pressure rise and total-to-static efficiency. Further results suggest that this effect can be mitigated to an extent, by reducing the tip gap. A smaller tip gap is shown to reduce the size of the tip leakage vortex as well as extending the effect of the blade tip boundary layer, reducing leakage flow. Literature indicates that reducing the size of the

tip vortex has the possible benefit of reducing fan noise.

Additional P3DM data shows that the tip gap has an impact on the flow field across the entire blade span, reducing the outlet tangential velocity and increasing the axial velocity component. These alterations to the flow field account, at least in part, for the loss in total-to-static pressure. While reducing tip gap is shown to mitigate these alterations to the flow field to an extent, it is suggested that these loses should be accounted for in the design method in the future. Additional measures such as tip treatments should also be considered.

Stall occurs in the M-fan at a volume flow rate of $265\,\mathrm{m^3/s}$. While this stall margin is acceptable, analysis of the flow across the blade surface shows that the stall margin may be improved by altering the aerofoil section at the blade root. Based on this result future studies should consider using a different base aerofoil to the NASA LS 0413 section. Other aerofoil optimisation techniques, such as aerofoil blending should be considered.

7.1   Recommendations

Based on the findings of this thesis the following recommendations and proposals for future work are made:

1. The M-fan should be operated with as small a tip gap as reasonably possible. The tip gap recommended in the design specifications results in unacceptable high fan performance losses.

2. Tip treatments such as those proposed by Corsini *et al.* (2007) and Wilkinson and Van der Spuy (2015) should be considered for the M-fan. A tip treatment may eliminate the need to reduce the tip gap.

3. Extensive experimental validation including fan characteristic testing and flow field measurements should be undertaken in order to properly validate the M-fan design and the numerical models used here.

4. A different aerofoil optimisation scheme should be considered in order to eliminate the issues encountered at the blade root in this study. Literature presented in Chapter 2 indicates several possible avenues for this. At the very least a different base aerofoil section should be used at the blade root.

5. A method should be developed to account for flow field alterations associated with a tip gap at the design stage. It is proposed that this method should be incorporated into the design method used in this thesis. This will develop a more versatile and precise design method, producing more efficient fans.

List of References

ANSYS inc. (2015). Ansys fluent user's guide, release 16.2.

Augustyn, O.P., Van der Spuy, S.J. and Von Backström, T.W. (2016). Numerical and experimental investigation into the accuracy of the fan scaling laws applied to large diameter axial flow fans. *Proceedings of the Institution of Mechanical Engineers, Part A: Journal of Power and Energy*, vol. 230, no. 5, pp. 477–486.

Bamberger, K. and Carolus, T. (2012). Optimization of axial fans with highly swept blades with respect to losses and noise reduction. *Noise Control Engineering Journal*, vol. 60, no. 6, pp. 716–725.

Bamberger, K. and Carolus, T. (2015*a*). Achievable total-to-static efficiencies of low-pressure axial fans. In: *Proceedings of the Fan 2015 Conference*.

Bamberger, K. and Carolus, T. (2015*b*). Analysis of the flow field in optimized axial fans. In: *ASME Turbo Expo 2015: Turbine Technical Conference and Exposition*, pp. V001T09A013–V001T09A013. American Society of Mechanical Engineers.

Beiler, M. and Carolus, T. (1999). Computation and measurement of the flow in axial flow fans with skewed blades. *Transactions-American Society OF MECHANICAL Engineers Journal of Turbomachinary*, vol. 121, pp. 59–66.

Bonanni, T., Cardillo, L., Corsini, A., Delibra, G., Sheard, A.G. and Volponi, D. (2016). Derivative design of axial fan range: From academia to industry. In: *ASME Turbo Expo 2016: Turbomachinery Technical Conference and Exposition*, pp. V006T07A006–V006T07A006. American Society of Mechanical Engineers.

Bredell, J.R., Kröger, D. and Thiart, G. (2006). Numerical investigation of fan performance in a forced draft air-cooled steam condenser. *Applied Thermal Engineering*, vol. 26, no. 8, pp. 846–852.

Bruneau, P.R.P. (1994). *The design of a single rotor axial flow fan for a cooling tower application*. Master's thesis, Stellenbosch: University of Stellenbosch.

BSI Group (2007). BS EN ISO 5801:2008, BS 848-1:2007 Industrial fans. - performance testing using standardized airways.

Carolus, T.H. and Starzmann, R. (2011*a*). An aerodynamic design methodology for low pressure axial fans with integrated airfoil polar prediction. In: *ASME 2011 Turbo Expo: Turbine Technical Conference and Exposition*, pp. 335–342. American Society of Mechanical Engineers.

Carolus, T.H. and Starzmann, R. (2011*b*). An aerodynamic design methodology for low pressure axial fans with integrated airfoil polar prediction. In: *ASME 2011 Turbo Expo: Turbine Technical Conference and Exposition*, pp. 335–342. American Society of Mechanical Engineers.

Cencelli, N.A. (2006). *Aerodynamic optimisation of a small-scale wind turbine blade for low windspeed conditions*. Master's thesis, Stellenbosch: Stellenbosch University.

Corsini, A., Delibra, G. and Sheard, A.G. (2013). A critical review of computational methods and their application in industrial fan design. *ISRN Mechanical Engineering*, vol. 2013.

Corsini, A. and Rispoli, F. (2004). Using sweep to extend the stall-free operational range in axial fan rotors. *Proceedings of the Institution of Mechanical Engineers, Part A: Journal of Power and Energy*, vol. 218, no. 3, pp. 129–139.

Corsini, A., Rispoli, F. and Sheard, A. (2010). Shaping of tip end-plate to control leakage vortex swirl in axial flow fans. *Journal of Turbomachinery*, vol. 132, no. 3, p. 031005.

Corsini, A., Rispoli, F. and Sheard, A.G. (2007). Development of improved blade tip endplate concepts for low-noise operation in industrial fans. *Proceedings of the Institution of Mechanical Engineers, Part A: Journal of Power and Energy*, vol. 221, no. 5, pp. 669–681.

Dixon, S.L. (1978). *Fluid mechanics-thermodynamics of turbomachinery*. 3rd edn. William Clowes (Beccles) Ltd.

Downie, R., Thompson, M. and Wallis, R. (1993). An engineering approach to blade designs for low to medium pressure rise rotor-only axial fans. *Experimental thermal and fluid science*, vol. 6, no. 4, pp. 376–401.

Drela, M. (1989). Xfoil: An analysis and design system for low reynolds number airfoils. In: *Low Reynolds number aerodynamics*, pp. 1–12. Springer.

Drela, M. and Youngren, H. (2001). Xfoil 6.94 user guide.

Dugao, Z. and Jiang, Z. (1996). Optimization design of an axial-flow fan used for mining local-ventilation. *Computers & industrial engineering*, vol. 31, no. 3, pp. 691–696.

EPRI (2004). Comparison of alternate cooling technologies for u.s. power plants: economic, environmental and other trade-offs. Tech. Rep., EPRI, Palo Alto, CA.

European Commission (2011). Commission Regulation (EU) No. 327/2011. *Official Journal of the European Union*, pp. 8–21. L90.

Fukano, T., Takamatsu, Y. and Kodama, Y. (1986). The effects of tip clearance on the noise of low pressure axial and mixed flow fans. *Journal of Sound and Vibration*, vol. 105, no. 2, pp. 291–308.

Gur, O. and Rosen, A. (2005). Propeller performance at low advance ratio. *Journal of Aircraft*, vol. 42, no. 2, pp. 435–441.

Himmelskamp, H. (1947). *Profile investigations on a rotating airscrew*. Ph.D. thesis, University of Göttingen.

Hoerner, S.F. (1965). *Fluid-dynamic drag: practical information on aerodynamic drag and hydrodynamic resistance*. Hoerner Fluid Dynamics.

Hoerner, S.F. and Borst, H.V. (1975). Fluid-dynamic lift: Practical information on aerodynamic and hydrodynamic lift. *NASA STI/Recon Technical Report A*, vol. 76, p. 32167.

Horlock, J.H. (1958). *Axial flow compressors: fluid mechanics and thermodynamics*. Butterworths scientific publications.

Kröger, D.G. (2004). *Air-cooled heat exchangers and cooling towers*, vol. 1. PennWell Books.

Launder, B.E. and Spalding, D.B. (1974). The numerical computation of turbulent flows. *Computer methods in applied mechanics and engineering*, vol. 3, no. 2, pp. 269–289.

Lee, K.-S., Kim, K.-Y. and Samad, A. (2008). Design optimization of low-speed axial flow fan blade with three-dimensional rans analysis. *Journal of mechanical science and technology*, vol. 22, no. 10, pp. 1864–1869.

Lewis, R. and Hill, J. (1971). The influence of sweep and dihedral in turbomachinery blade rows. *Journal of Mechanical Engineering Science*, vol. 13, no. 4, pp. 266–285.

Lien, F.-S. and Leschziner, M. (1994). Assessment of turbulence-transport models including non-linear rng eddy-viscosity formulation and second-moment closure for flow over a backward-facing step. *Computers & Fluids*, vol. 23, no. 8, pp. 983–1004.

Liu, S.H., Huang, R.F. and Lin, C.A. (2010). Computational and experimental investigations of performance curve of an axial flow fan using downstream flow resistance method. *Experimental Thermal and Fluid Science*, vol. 34, no. 7, pp. 827–837.

Louw, F.G. (2011). *Performance Trends of a Large Air-Cooled Steam Condenser During Windy Conditions*. Master's thesis, Department of Mechanical and Mechatronic Engineering, University of Stellenbosch.

Louw, F.G. (2015). *Investigation of the flow field in the vicinity of an axial flow fan during low flow rates*. Ph.D. thesis, Stellenbosch University.

Louw, F.G., Bruneau, P.R., Von Backström, T.W. and Van der Spuy, S.J. (2012). The design of an axial flow fan for application in large air-cooled heat exchangers. In: *ASME Turbo Expo 2012: Turbine Technical Conference and Exposition*, pp. 771–785. American Society of Mechanical Engineers.

Louw, F.G., von Backström, T.W. and Van der Spuy, S.J. (2015). Lift and drag characteristics of an air-cooled heat exchanger axial flow fan. *Journal of Fluids Engineering*, vol. 137, no. 8, p. 081101.

Masi, M. and Lazzaretto, A. (2015). A simplified theory to justify forward sweep in low hub-to-tip ratio axial fan. In: *ASME Turbo Expo 2015: turbine technical conference and exposition*, pp. V001T09A011–V001T09A011. American Society of Mechanical Engineers.

McGhee, R.J. and Beasley, W.D. (1973). *Low-Speed Aerodynamic Characteristics of a 17-Percent-Thick Airfoil Section Designed for General Aviation Applications*. Langley Research Center.

McGhee, R.J. and Beasley, W.D. (1976). Effects of thickness on the aerodynamic characteristics of an initial low-speed family of airfoils for general aviation applications.

McGhee, R.J., Beasley, W.D. and Somers, D.M. (1977). *Low-Speed Aerodynamic Characteristics of a 13-Percent-Thick Airfoil Section Designed for General Aviation Applications*. Langley Research Center.

Menter, F. (1993). Zonal two equation kw turbulence models for aerodynamic flows. In: *23rd fluid dynamics, plasmadynamics, and lasers conference*, p. 2906.

Meyer, C. (2005). Numerical investigation of the effect of inlet flow distortions on forced draught air-cooled heat exchanger performance. *Applied Thermal Engineering*, vol. 25, no. 11, pp. 1634–1649.

Meyer, C. and Kröger, D. (2001). Numerical simulation of the flow field in the vicinity of an axial flow fan. *International Journal for Numerical Methods in Fluids*, vol. 36, no. 8, pp. 947–969.

MinWaterCSP (2017). MinWaterCSP Project.
Available at: `http://www.minwatercsp.eu/`

Owen, M.T.F. (2010). *A numerical investigation of air-cooled steam condenser performance under windy conditions*. Ph.D. thesis, University of Stellenbosch.

Pericleous, K.A., Patel, M. *et al.* (1987). The modelling of tangential and axial agitators in chemical reactors. *Physicochemical hydrodynamics*, vol. 8, no. 2, pp. 105–123.

Powell, M.J. (1978). Algorithms for nonlinear constraints that use lagrangian functions. *Mathematical programming*, vol. 14, no. 1, pp. 224–248.

Salta, C. and Kröger, D. (1995). Effect of inlet flow distortions on fan performance in forced draught air-cooled heat exchangers. *Heat recovery systems and CHP*, vol. 15, no. 6, pp. 555–561.

Shih, T.-H., Liou, W.W., Shabbir, A., Yang, Z. and Zhu, J. (1995). A new $k - \epsilon$ eddy viscosity model for high reynolds number turbulent flows. *Computers & Fluids*, vol. 24, no. 3, pp. 227–238.

Snyman, J. (2005). *Practical mathematical optimization: an introduction to basic optimization theory and classical and new gradient-based algorithms*, vol. 97. Springer Science & Business Media.

Sorensen, D., Thompson, M. and Sorensen, J. (2000). Toward improved rotor-only axial fans part ii: Design optimization for maximum efficiency. *Journal of fluids engineering*, vol. 122, no. 2, pp. 324–329.

Sørensen, D.N. (2001). Minimizing the trailing edge noise from rotor-only axial fans using design optimization. *Journal of sound and vibration*, vol. 247, no. 2, pp. 305–323.

Spalart, P. and Allmaras, S. (1992). A one-equation turbulence model for aerodynamic flows. In: *30th aerospace sciences meeting and exhibit*, p. 439.

Stinnes, W. and Von Backström, T. (2002). Effect of cross-flow on the performance of air-cooled heat exchanger fans. *Applied Thermal Engineering*, vol. 22, no. 12, pp. 1403–1415.

Thiart, G. and Von Backström, T. (1993). Numerical simulation of the flow field near an axial flow fan operating under distorted inflow conditions. *Journal of wind engineering and industrial aerodynamics*, vol. 45, no. 2, pp. 189–214.

Vad, J. (2008). Aerodynamic effects of blade sweep and skew in low-speed axial flow rotors at the design flow rate: an overview. *Proceedings of the Institution of Mechanical Engineers, Part A: Journal of Power and Energy*, vol. 222, no. 1, pp. 69–85.

Vad, J. and Bencze, F. (1998). Three-dimensional flow in axial flow fans of non-free vortex design. *International journal of heat and fluid flow*, vol. 19, no. 6, pp. 601–607.

Vad, J. and Horváth, C. (2008). The impact of the vortex design method on the stall behavior of axial flow fan and compressor rotors. In: *ASME Turbo Expo 2008: Power for Land, Sea, and Air*, pp. 229–238. American Society of Mechanical Engineers.

Van der Spuy, S.J. (1997). *The Design of a Low-noise Rotor-only Axial Flow Fan Series*. Master's thesis, University of Stellenbosch.

Van der Spuy, S.J. (2011). *Perimeter fan performance in forced draught air-cooled steam condensers*. Ph.D. thesis, Stellenbosch: Stellenbosch University.

Van Niekerk, C. (1958). Ducted fan design theory. *J. appl. Mech*, vol. 25, no. 3, pp. 325–331.

Van Rossum, G. and Drake, F.L. (2010). *The python language reference.* Python Software Foundation Amsterdam, Netherlands.

Vanderplaats, G.N. and Sugimoto, H. (1985). Application of variable metric methods to structural synthesis. *Engineering computations*, vol. 2, no. 2, pp. 96–100.

Vanderplaats Research & Development Inc (2001). User's manual version 5.0., dot design optimization tools.

Venter, S.J. (1990). *The effectiveness of axial flow fans in A-frame plenums.* Ph.D. thesis, Stellenbosch: University of Stellenbosch.

Venter, S.J. and Kröger, D.G. (1992). The effect of tip clearance on the performance of an axial flow fan. *Energy conversion and management*, vol. 33, no. 2, pp. 89–97.

Von Backström, T.W., Buys, J.D. and Stinnes, W.H. (1996). Minimization of the exit loss of a rotor-only axial fan. *Engineering Optimization+ A35*, vol. 26, no. 1, pp. 25–33.

Von Backström, T.W., Van der Spuy, S.J. and Stinnes, W.H. (2000). The limiting efficiency of rotor-only axial fans and turbines. *SACAM 2000- InternationalConference on Applied Mechanics, Durban, South Africa*, pp. 647–652.

Wallis, R.A. (1983). *Axial flow fans and ducts.* John Wiley.

Wessels, F.J., Venter, G. and Von Backström, T. (2012). An efficient scheme for describing airfoils using non-uniform rational b-splines. In: *ASME Turbo Expo 2012: Turbine Technical Conference and Exposition*, pp. 969–977. American Society of Mechanical Engineers.

Wilkinson, M.B., Louw, F.G., Van der Spuy, S.J. and Von Backström, T.W. (2016). A comparison of actuator disc models for axial flow fans in large air-cooled heat exchangers. In: *ASME Turbo Expo 2016: Turbomachinery Technical Conference and Exposition*, pp. V001T09A003–V001T09A003. American Society of Mechanical Engineers.

Wilkinson, M.B. and Van der Spuy, S.J. (2015). The effect of fan tip configuration on air-cooled condenser axial flow fan performance. In: *Fan2015*, pp. 1–12. Lyon, France.

Yang, L., Hua, O. and Zhao-Hui, D. (2007). Optimization design and experimental study of low-pressure axial fan with forward-skewed blades. *International Journal of Rotating Machinery*, vol. 2007.

Appendices

Appendix A

Optimisation

Optimisation is extensively used in the design of the M-fan in order to find the best possible flow and blading configurations given the constraints on this study. There as several forms of mathematical optimisation that aim to minimise or maximise a design function subject to certain conditions. According to Snyman (2005) the general form of an optimisation problem can be given as follows:

$$minimise \quad F(x) \quad where \quad x = [x_1, x_2, ..., x_n]^T$$

Subject to constraints:

$$g_j(x) \leq 0, \quad j = 1, 2, ..., m \qquad h_i(x) \leq 0, \quad i = 1, 2, ..., r \tag{A.0.1}$$

where $f(x)$, $g_j(x)$ and all functions of x. The individual components of $x = [x_1, x_2...]^T$ are referred to a design variables, $f(x)$ is referred to the objective function and $g_j(x)$ and $h_i(x)$ are the equality and inequality constraint functions (Snyman (2005)). In addition to this general formulation, side constraints may be placed on individual design variables as follows:

$$x_i^L \leq x_i \leq x_i^U \quad i = 1, 2, ..., n \tag{A.0.2}$$

These side constraints are usually imposed to prevent the optimisation method from finding an optimum value for the design variable vector x where some design variable values in the vector may not be feasible. According to Vanderplaats Research & Development Inc (2001) a common example would be to ensure non-zero values for certain design variables, such as thickness for a mechanical part. The aim of any optimisation procedure is to find the vector x^* for which $f(x^*)$ is a minimised within the given constraints.

Broadly speaking there are two types of optimisation problems, constrained problems and unconstrained problems. All of the optimisation problems encountered in this study are of the constrained type. While there are several methods for solving constrained optimisation problems, the method chosen for this study is the Sequential Quadratic Programming (SQP) method of Powell

(1978) with modifications by Vanderplaats and Sugimoto (1985). According to Snyman (2005) SQP methods are currently considered the best gradient based approach to solving constrained optimisation problems. The SQP method is used extensively in the design procedure (Chapter 3) to optimise the fan flow field and blading. This Appendix aims to provide a brief overview of the SQP method used, as well as detailing other numerical techniques used in the optimisation procedures.

A.1   The Sequential Quadratic Programming (SQP) Algorithm

The Sequential Quadratic Programming (SQP) method of Powell (1978) with modifications by Vanderplaats and Sugimoto (1985) as used in this study, is implemented by means of the Van der Plaats Research and Development DOT software package (Vanderplaats Research & Development Inc (2001)). DOT is a FORTRAN based optimisation program which can easily be integrated into an application program such as the PYTHON script that implements the fan design method in Chapter 3. DOT provides tools to solve linear and non-linear non-linear optimisation problems with or without constraint. According to Vanderplaats Research & Development Inc (2001), DOT solves optimisation problems iteratively in order to maximise solution speed, while the software should provide a good solution, it is unlikely to be the precise mathematical optimum.

In the SQP algorithm used by DOT only inequality constraints are considered. According to Vanderplaats Research & Development Inc (2001) equality constraints should be represented as two sets of inequality constraints as demonstrated below:

$$h_i(x) = 0 \tag{A.1.1}$$

becomes

$$h_i(x) \leq 0 \tag{A.1.2}$$

$$h_i(x) \geq 0 \tag{A.1.3}$$

If the conditions in equations A.1.3 and A.1.2 are met, the equality constraint in equation A.1.1 will be met. DOT also considers side constraints of the form given in equation A.0.2. Although these side constraints could be reformulated as inequality constraints, they are kept separate. According to Vanderplaats and Sugimoto (1985) this is to ensure that design variables outside of the side constraints are never considered, which is essential for the solution of many engineering problems. With this in mind the optimisation problem considered by DOT should be cast in the following form:

$$minimise \quad F(x) \quad where \quad x = [x_1, x_2, ..., x_n]^T \tag{A.1.4}$$

Subject to constraints:

$$g_j(x) \leq 0, \quad j = 1, 2, ..., m$$
$$x_i^L \leq x_i \leq x_i^U \quad i = 1, 2, ..., n \tag{A.1.5}$$

According to Vanderplaats and Sugimoto (1985) the optimisation process proceeds by finding a search direction, S and then performing a line search to find the maximum design improvement, as demonstrated by equation A.1.6.

$$x^q = x^{q-1} + \alpha^* S^q \tag{A.1.6}$$

In order implement the procedure given in equation A.1.6, the problem statement must be cast into a Lagrangian function of the form given in equation A.1.7.

$$L(x, \lambda) = f(x) + \sum_m^{j=1} \lambda_i g_j(x) \tag{A.1.7}$$

With the problem statement cast into Lagrangian form it is now possible to define a set of conditions an optimal point. According to Snyman (2005) the KKT conditions, defined in equation A.1.8, constitute the necessary set of conditions that must be satisfied at the solution x^* to the problem statement defined in equation A.1.7. A formal proof of these conditions is given by Snyman (2005).

$$\frac{\delta f}{\delta x_i}(x) + \sum_{j=1}^m \lambda - j \frac{\delta g_j}{\delta x_i}(x) = 0 \quad i = 1, 2, ..., n$$
$$g_j(x) \leq 0 \quad j = 1, 2, .., m \tag{A.1.8}$$
$$\lambda_j g_j(x) = 0 \quad j = 1, 2, ..., m$$
$$\lambda_j \geq 0 \quad j = 1, 2, ..., m$$

The version of the SQP algorithm used by DOT is based on the fact that by satisfying the KKT conditions, a minimum of the original problem is found (Vanderplaats and Sugimoto (1985)). Noting that the first criteria listed in equation A.1.8 is a set of linear equations, should the Lagrangian be quadratic this condition could be used to easily optimise the function. This forms the quadratic programming (QP) problem, which is an important sub-problem in the SQP algorithm (Snyman (2005)). DOT solves the QP problem in order to find the direction of improving design and relies on a one-dimensional search algorithm to determine the design changes at each iteration (Vanderplaats and Sugimoto (1985)). In order to solve the QP sub-problem and find the search direction an objective function is formulated which is a combination of a linearised version of the original objective function and the quadratic terms form the approximation of the Lagrangian (Vanderplaats and Sugimoto (1985)).

The constraints to the objective function are a linearised approximation of the original constraints. This results in a problem statement of the following form:

At iteration q, find the components of S that:

$$minimise \quad Q(S) = F(x^q) + \nabla f(x^q)S + \frac{1}{2}S^T BS \qquad (A.1.9)$$

Subject to the following constraint:

$$\nabla g_j(x^q)S + \delta_j g_j(x^q) \leq 0 \quad j = 1, 2, ..., m \qquad (A.1.10)$$

According to Vanderplaats and Sugimoto (1985) the matrix B is a positive definite matrix which approximates the Hessian of the Lagrangian and parameters δ and $\bar{\delta}$ are chosen to ensure that the QP problem has a feasible solution. The value of δ is defined as:

$$\delta_j = \begin{cases} 1 & \text{if } g_j(x^q) < 0 \\ \bar{\delta} & \text{if } g_j(x^q) \geq 0 \end{cases} \qquad (A.1.11)$$

where $0.9 \leq \bar{\delta} \leq 0.95$.

Once the QP sub problem has been solved, DOT calculates the Lagrange multipiers, $\lambda_j \ j = 1, 2, ..., m$, at the optimum point of Function Q (Vanderplaats Research & Development Inc (2001)) With the search direction S known, a one-dimensional search is performed to update the design parameters. The search makes use of the approximate Lagrangian function and takes the form:

Find α to minimise:

$$\phi = f(x) + \sum_{u=1}^{m} u_j(max[0, g_j(x)]) \qquad (A.1.12)$$

where:

$x = x^{q-1} + \alpha S$

$$u_j = \begin{cases} \lambda_j \quad j = 1, 2, ..., m & \text{first iteration} \\ max[\lambda_j, 0.5(u_j' + \lambda_j)] \quad j = 1, 2, ..., m & \text{subsequent iterations} \end{cases} \qquad (A.1.13)$$

where u_j' is equal to u_j from the previous iteration. According to Vanderplaats and Sugimoto (1985) this problem is well conditioned and $\alpha = 1$ is a good initial estimate of α^*. Vanderplaats Research & Development Inc (2001) states that in DOT the components of Φ are approximated as this function is smooth, but has discontinuous derivatives at the constraint boundaries.

Once the line search is complete the B matrix is updated using the Broyden-Fletcher-Gold- farb-Shanno (BFGS) method (Vanderplaats Research & Development Inc (2001)). According to Snyman (2005) the BFGS method is a

state of the art quasi-Newton method for updating the B matrix. The BFGS method is detailed below in equations A.1.14 to A.1.19, where B^* replaces B for the next iteration, $q + 1$.

$$B^* = B - \frac{Bpp^T B}{p^T Bp} + \frac{\eta\eta^T}{p^T \eta} \tag{A.1.14}$$

where:

$$p = x^q - x^{q-1} \tag{A.1.15}$$

$$\eta = \theta y + (1 - \theta)Bp \tag{A.1.16}$$

$$y = \nabla_x \Phi^q - \nabla_x \Phi^{q-1} \tag{A.1.17}$$

$$\Phi = f(x) + \sum_{j=1}^{m} \lambda_j g_j(x) \tag{A.1.18}$$

$$\theta = \begin{cases} 1 & \text{if } p^T y \geq 0.2p^t Bp \\ \frac{0.8p^T Bp}{p^T Bp - p^T y} & \text{if } p^T y < 0.2p^T Bp \end{cases} \tag{A.1.19}$$

A.2   Additional Numerical Techniques

In the vortex design method presented in Chapter 3 it is necessary to approximate integrals and derivatives. In order to do this the bounded area between the fan hub and blade tip is discretised radially into n discrete intervals of length h. Integration of a given function $f(x)$ is then approximated by the trapezoid rule:

$$\int_1^a f(x)dx \approx \frac{h}{2}f(x_0) + h\sum_{i=1}^{n-1} f(x_i) + \frac{h}{2}f(x_n) \tag{A.2.1}$$

where the terms a, h, x_i and i are defined as:

$$a = 1/x_h \tag{A.2.2}$$

$$h = \frac{a - 1}{n} \tag{A.2.3}$$

$$x_i = 1 + ih \tag{A.2.4}$$

$$i = 0, 1, 2, 3, ..., n \tag{A.2.5}$$

Higher order approximation is used to calculate derivative terms where necessary. The same definitions stated as follows:

$$i = 0 : f'(x_i) \approx \frac{-25f(x_0) + 48f(x_1) - 36f(x_2) + 16f(x_3) - 3f(x_4)}{12h}$$

$$i = 1 : f'(x_i) \approx \frac{-3f(x_0) - 10f(x_1) + 18f(x_2) - 6f(x_3) + f(x_4)}{12h}$$

$$1 < i < n - 1 : f'(x_i) \approx \frac{f(x_{i-2}) - 8f(x_{i-1}) + 8f(x_{i+1}) - f(x_{i=2})}{12h}$$

$$i = n - 1 : f'(x_i) \approx \frac{-f(x_{n-4}) + 6f(x_{n-3}) - 18f(x_{n-2}) + 10f(x_{n-1}) + 3f(x_n)}{12h}$$

$$i = n : f'(x_i) \approx \frac{3f(x_{n-4}) - 16f(xn - 3) + 36f(x_{n-2}) - 48f(x_{n-1}) + 25f(x_n)}{12h}$$

$$(\text{A.2.6})$$

The above listed techniques are identical to those used by Von Backström *et al.* (1996). It was decided to make use of the same methods owing to the simplicity and robustness of these methods, as well as the fact that they have been proven to be effective in this application by Van der Spuy (1997). Additionally these numerical techniques are very computationally efficient as they provide reasonable answers with out the need for iterative procedures or more complex mathematical operations.

Appendix B

Free Vortex Design

The free vortex assumption is at the centre of many classical fan design techniques in literature. It is regarded to be a simple, reliable method to design an efficient flow field for an axial flow fan. As demonstrated in Chapter 2 the method often results in highly efficient fans that are reasonably suited to operating requirements. For this reason a free vortex method was used to design early concepts that acted as a benchmark in this study, as detailed in Appendix C. The free vortex based method of Bruneau (1994) was used to design the initial concepts as this method was applied to the B-fans. The B-fans, especially the B2 variant, have been extensively studied in the context of operation in an air-cooled heat exchanger environment. For this reason it was decided to apply the same method to the design specifications provided for this study.

The method is used in conjunction with the hub-tip ratio selection method of Van Niekerk (1958), as presented in Chapter 3. The method presented here is derived from the work of Bruneau (1994) and is also described by Louw *et al.* (2012).

B.1   Vortex Design - Bruneau

The calculations described in this section are implemented by means of a PYTHON script in order to calculate the velocity components up and down stream of the fan blades, as shown in figure B.1. The inputs to the calculation scheme are the fan specifications as well as the desired hub to tip ratio.

Central to this method is the well known free vortex assumption, which indicates that swirl velocity is inversely proportional to radius as shown in equation B.1.1 where $k = $ constant.

$$c_\theta = \frac{k}{r} \tag{B.1.1}$$

This assumption has several simplifying benefits as mentioned in Chapter 2, one benefit being that there is no radial flow component ie. $c_r = 0$. Other
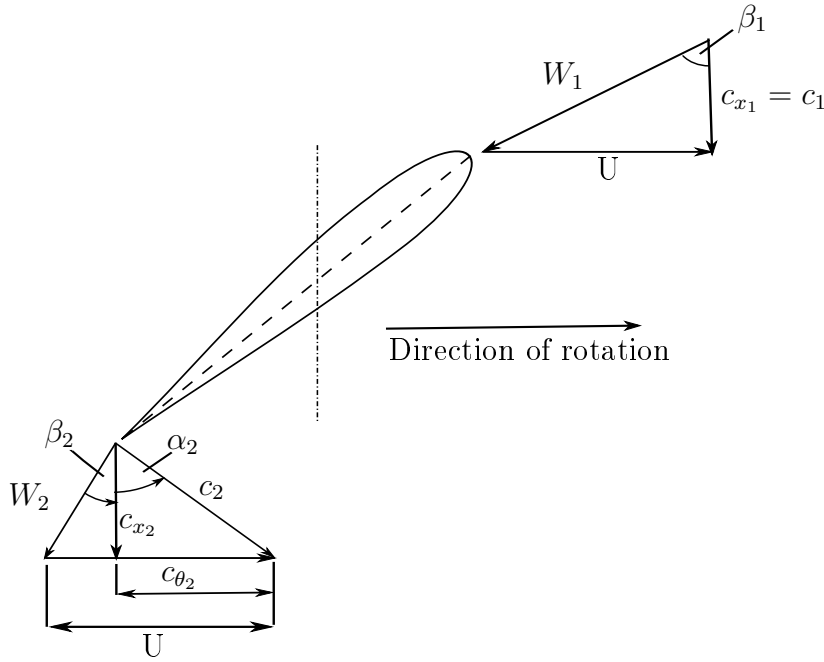
Figure B.1: Velocity diagram for a rotor only fan blade

benefits are that the axial velocity through the blade row is constant both radially and axially and work and total pressure distributions along the blade span are also constant. The use of the free vortex is also indicated to produce fan designs with the highest efficiency by several authors including Wallis (1983). High efficiency was a requirement for the fan of Bruneau (1994) as well as for fans developed by the present study. Bruneau (1994) made use of a power law swirl distribution in order to allow velocity profiles to deviate from the free vortex. This distribution is shown in the following equation:

$$c_\theta(r) = ar^n \tag{B.1.2}$$

In the above equation a is a constant and n is a constant value referred to as the swirl coefficient, where $n = -1$ gives the free vortex swirl distribution. The swirl coefficient allows the designer to alter the swirl distribution in the fan, however the free vortex assumption remains central to the calculation scheme.

The second piece of theory used by Bruneau (1994) is that of radial equilibrium. A simple approach to analysis of flow in an axial flow turbomachine is to assume that the flow conditions at the mean blade radius are representative of the flow conditions along the entire blade span. Radial flow within an axial turbomachine is caused by an imbalance between the radial and centrifugal forces within the machine. This means that the radial force resulting from the swirl component of velocity in the fan must be maintained by a radial pressure force in the opposite direction. The balance of these forces acting on a fluid element is referred to as radial equilibrium. In order to account for this Bruneau (1994) made use of a simplified radial equilibrium equation (SREE)

derived by Dixon (1978) shown below.

$$\frac{1}{\rho_a}\frac{dp_o(r)}{dr} = \frac{c_\theta(r)}{r}\frac{d}{dr}(rc_\theta(r)) + c_x(r)\frac{dc_x(r)}{dr} \tag{B.1.3}$$

Where axial and swirl velocities are functions of r, the spanwise fan radius. Equation B.1.3 is used to ensure radial equilibrium is enforced in the design procedure as well as to calculate the exit axial velocity.

With the above theory in mind it is clear that the blade span must be descretised into a number of points along its radius in order to ensure radial equilibrium is enforced along the entire blade span. The first step of the design procedure is to calculate the inlet axial velocity c_{x_1}. As there is assumed to be no inlet swirl velocity the inlet axial velocity is constant with radius and can be calculated as follows.

$$c_{x1} = \frac{\dot{V}}{A_f} \tag{B.1.4}$$

Where $\dot{V}$ is the volumetric flow rate given in the design specification and A_f is the fan annulus area. Once c_{x_1} is known, one can solve iteratively for c_{x2} and c_{θ_2}. The outlet swirl velocity component can be solved using equation B.1.2 where the constant term a can be calculated as follows:

$$c_{\theta_{2_h}} = \epsilon_h c_{x_1} \tag{B.1.5}$$

where

$$\epsilon(r) = \frac{c_\theta(r)}{c_x(r)} \tag{B.1.6}$$

Where ϵ_h is the hub swirl coefficient, which is given an initial value then updated iteratively.

$$a = \frac{c_{\theta_{2_h}}}{r_h^n} \tag{B.1.7}$$

Once a is known the outlet swirl velocity distribution can easily be calculated by the general swirl distribution, equation B.1.2.

In order to calculate the axial component of the fan exit velocity field the SREE equation (B.1.3) is integrated with respect to radius between the hub radius r_h and blade tip radius r_t where the general vortex expression (equation B.1.2) is substituted for $c_\theta(r)$. This results in the following expression:

$$c_{x_2}(r) = \sqrt{2a\omega_F(r^{n+1} - r_h^{n+1}) - R(r)a^2(n+1) + c_{x_2}^2(r_h)} \tag{B.1.8}$$

where R(r) is given by:

$$R(r) = ln\left(\frac{r}{r_h}\right)^2 \quad for \quad n = 0 \tag{B.1.9}$$

$$R(r) = \frac{r^{2n} - r_h^{2n}}{n} \quad for \quad n \neq 0 \tag{B.1.10}$$

Initially the value of outlet axial velocity c_{x_2} set to that of the inlet axial velocity, c_{x_1} and solved iteratively along with the swirl velocity components. The solution is subjected to two constraints:

1. $c_{x_2} > 0$

2. $\epsilon_h < 1.15$

Constraint 1 ensures that there is no backflow through the fan. Backflow tends to occur near the hub, therefore in the design procedure if backflow is detected near the hub the hub is enlarged until the constraint is met. This constraint does not however apply in the free vortex case as $c_{x1} = c_{x2}$ and is included for more general cases, where $n \neq 1$ in equation B.1.2. The second constraint is aimed at ensuring that blade twist is kept within reasonable limits as suggested by Wallis (1983). This ensures that the blade stagger angle at the hub is within a reasonable range as highly twisted blades are complex to manufacture. Excessive twist can also cause stall at off design flow rates, greatly reducing fan performance.

Once the axial and tangential outlet velocity distributions c_{x_2} and c_{θ_2} are known, the other parameters shown in figure 3.3 can be simply calculated across the entire blade span from trigonometric and geometric relationships.

$$u(r) = \omega_F r \tag{B.1.11}$$

$$w1(r) = \sqrt{u(r)^2 + c_{x_1}^2} \tag{B.1.12}$$

$$c_2(r) = \sqrt{c_{\theta_2}(r)^2 + c_{x_2}(r)^2} \tag{B.1.13}$$

$$w_2(r) = \sqrt{(u(r) - c_{\theta_2}(r))^2 + c_{x_2}(r)^2} \tag{B.1.14}$$

The relative inlet and outlet flow angles β_1 and β_2 as well as the absolute outlet flow angle α can be calculated by the following equations:

$$\beta_1(r) = arctan\left(\frac{u(r)}{c_{x_1}}\right) \tag{B.1.15}$$

$$\beta_2(r) = arctan\left(\frac{u(r) - c_{\theta_2}(r)}{c_{x_2}(r)}\right) \tag{B.1.16}$$

$$\alpha_2(r) = arctan(\frac{c_{\theta_2}(r)}{c_{x_2}(r)}) \tag{B.1.17}$$

The relative and absolute flow angles calculated in equations B.1.15, B.1.16 and B.1.17 are key outputs of the calculation scheme. Along with the outlet velocity profile swirl and radial distributions c_{x_2} and c_{θ_2}, these angles will be used to calculate the fan blade shape in the next stage of the design process.

At this point it is also possible to estimate the power imparted by the fan blades into the flow field and thus the fan's shaft power requirement. Fan power is one of the characteristics that is used as a standard to quantify fan performance, therefore an estimate of fan power provides the designer with some feedback about the quality of the design. First it is important to calculate the mass flow distribution through the fan, mass flow rate is computed as follows:

$$\dot{m_a} = \rho_a \dot{V} \tag{B.1.18}$$

The radial mass flow distribution is defined as:

$$\dot{m}(r) = \rho_a c_{x_2}(r) A(r) \tag{B.1.19}$$

where is the area of the differential radial element at a given radius. Fan power can be computed by means of the Euler work distribution as shown below.

$$W(r) = u(r) c_{\theta_2}(r) \tag{B.1.20}$$

Power distribution in the fan can be can be calculated as follows:

$$P(r) = W(r)\dot{m}(r) \tag{B.1.21}$$

Where $\dot{m}(r)$ is the radial mass flow distribution. Fan power can be found by taking the sum of equation B.1.21 between the hub and tip radius.

$$P = \sum P(r) \tag{B.1.22}$$

Finally it is important to check that the vortex designed meets the design fan static pressure. It is also necessary to calculate the fan static and total pressure loss coefficients. The pressure loss coefficients will be used later in the design procedure to estimate the fan static and total efficiencies. In order to calculate these parameters it is essential to find the total, static and dynamic pressure distributions at the fan outlet. It is assumed that the total pressure far upstream of the fan is equivalent to atmospheric pressure.

$$p_{t_1} = p_{atm} \tag{B.1.23}$$

The total and dynamic pressure distributions can then be calculated as follows:

$$p_{t_2}(r) = p_{t_1} + \rho_a u(r) c_{\theta_2}(r) \tag{B.1.24}$$

$$p_{d_2}(r) = \frac{1}{2}\rho_a(c_{\theta_2}(r)^2 + c_{x_2}(r)^2) \tag{B.1.25}$$

Static pressure by definition is total pressure minus dynamic pressure ie:

$$p_{s_2}(r) = p_{t_2} - p_{d_2} \tag{B.1.26}$$

In order to fine the total and static pressure differences, the mass weighted average total and static pressures must be found.

$$p_{t_{2avg}} = \sum \frac{p_{t_2}(r)\dot{m}(r)}{\dot{m}_a} \tag{B.1.27}$$

$$p_{s_{2avg}} = \sum \frac{p_{s_2}(r)\dot{m}(r)}{\dot{m}_a} \tag{B.1.28}$$

The total and static pressure differences across the fan can now be calculated by subtracting p_{t_1} from equations B.1.27 and B.1.28.

$$\Delta p_{tt} = p_{t_{2avg}} - p_{t_1} \tag{B.1.29}$$

$$\Delta p_{ts} = p_{s_{2avg}} - p_{t_1} \tag{B.1.30}$$

Finally the total and static pressure loss values can be calculated by the following expressions.

$$K_t = \frac{\Delta p_{tt}}{0.5\rho_a c_{x_1}^2} \tag{B.1.31}$$

$$K_s = \frac{\Delta p_{ts}}{0.5\rho_a c_{x_1}^2} \tag{B.1.32}$$

The flow factor can be calculated for each radius by:

$$\phi = \frac{c_{x_2}}{\omega_F r} \tag{B.1.33}$$

The values generated by these equations are then fed into a blade profile generation script which generates the blade shape in order to create the desired turning angles in the flow field. Key parameters considered by the blade generation code are the pressure loss coefficients and the velocity triangle vectors and angles as shown in figure 3.3. Other data such as the power estimate and exit velocity profiles serve as outputs for the overall design procedure, these are saved to a file for later use.

B.2   Blading Design -Bruneau

The blading design technique used to design the Concept 1 fan in Appendix C shares the same theoretical basis as the work presented in Chapter 3, Section 3.4. and makes use of the same equations. The major differences between the methods presented there and the methods use by Bruneau (1994) and applied in this study is that no chord length or aerofoil optimisation is carried out. Instead hub and tip lift coefficients are manually selected and chord lengths at these two locations are calculated using equations 3.6.4 and 3.6.5. The aerofoil section used is the NASA LS 0413 profile of McGhee *et al.* (1977).

Experimentally obtained lift and drag data published by McGhee *et al.* (1977) is used in order to estimate fan efficiency as well as calculating aerofoil angle of attack requirements. The data used is obtained at a Reynolds number of 2.1×10^6, which is close to the average Reynolds number for both the Concept 1 and Concept 2 designs presented in Appendix C.

Appendix C

M-fan Development

The design procedure described in Chapter 3 aims to address the needs of the design specifications in table 3.1 while adhering to the constraints described in Section 3.1. While the M-fan is the final product of the design procedure, two concept designs were carried out that aided in the development of the M-fan. The details of the two concepts are described below:

- **Concept 1** - Concept 1 is designed using the fan design method of Bruneau (1994), as used to design the B-fans (Bruneau (1994),Louw *et al.* (2012)). This method applies a free vortex flow distribution method, as described in Appendix B. The design applies the hub-tip ratio selection method of Van Niekerk (1958), as described in Chapter 3. The blading is also designed in a similar manner to the method presented in Chapter 3, however the chord distribution is not optimised. Rather hub and tip lift coefficients which fit the design constraints are selected defining the hub and tip chord lengths. A linear interpolation between these two points then describes the blade. This concept aims to provide a baseline based on historical research for later concepts to improve on.

- **Concept 2** - Concept 2 is designed using the technique presented in Chapter 3, aside from the camber optimisation step. This means that like concept one the NASA LS 0413 aerofoil section is used along the entire blade span. The vortex design method of Von Backström *et al.* (1996) is used and the chord distribution is optimised as described in Chapter 3. This design aims to improve on concept one both in terms of meeting performance requirements as well as geometric constraints.

The two concepts presented above are compared with the final M-fan design both in terms of geometry and performance. This aims to demonstrate the rationale behind the M-fan design. The performance characteristics of the three fans are compared numerically by means of the actuator disk model (ADM). This was done as the ADM is quicker to set up and run than the periodic three dimensional model (P3DM) allowing designs to be compared

relatively easily. Numerical modelling of the two concept designs was carried out by means of the standard actuator disk model, as both concepts make use of the NASA LS 0413 profile. Numerical modelling of the M-fan is conducted using the XFOIL actuator disk model, in order to account for the aerofoil camber variation along the blade span. The standard ADM has been extensively validated against experimental data for other fans such as the B-fan in studies such as those of Wilkinson *et al.* (2016) and Louw (2015). The XFOIL ADM is validated against the P3DM later in this study.

C.1　Geometric Considerations

The design specifications for this study contain several geometric constraints in order to ensure the ease of manufacturing and installation of the fan. These constraints are presented in Chapter 3, Section 3.1. A successful design must meet these constraints, as well as providing the best possible performance characteristics. The geometries of the three fans are shown in figure C.1, comparing the chord distributions and twist patterns of each fan.

It has to be noted that the three designs presented in figure C.1 all meet the minimum geometric requirements specified in Chapter 3. Performance considerations were the main reasons for the evolutions in the design process that lead to the M-fan, however these evolutions also lead to improvements in the satisfaction of the geometric requirements. The stacking profiles shown in figure C.1 demonstrate a reduction in blade twist between the first concept design and the other two fans. The root setting angle for Concept 1 is 39°, compared to 37° and 34° for Concept 2 and the M-fan respectively. The change between Concept 1 and 2 is due to the different vortex design methods used. The free vortex method requires a higher axial velocity at the blade root, where as the technique of Von Backström *et al.* (1996) results in an exit flow profile where a lower axial velocity is required, reducing the required blade twist at the root. The reduction in twist between Concept 2 and the M-fan is explained by the camber optimisation procedure, which results in a smaller aerofoil angle of attack bring required at the hub (6° for Concept 2 and 3° for the M-fan), further reducing blade twist.

The other apparent difference between Concept 1 and the other designs shown in figure C.1, is in chord distribution. This is due to the change in blading design technique. The chord length distribution of Concept 2 and the M-fan is optimised in order to properly distribute lift properties while meeting design constraints, whereas the chord distribution of Concept 1 is the result of selecting hub and tip lift coefficient values that resulted in a reasonable design, with a linear interpolation used to calculate the chord lengths between these two points. The hub and tip chord lengths of the Concept 1 fan are 0.96 m and 0.35 m compared to 0.85 m and 0.83 m for the Concept 2 and M fans. The reduction in chord length at the hub, coupled with the aforementioned
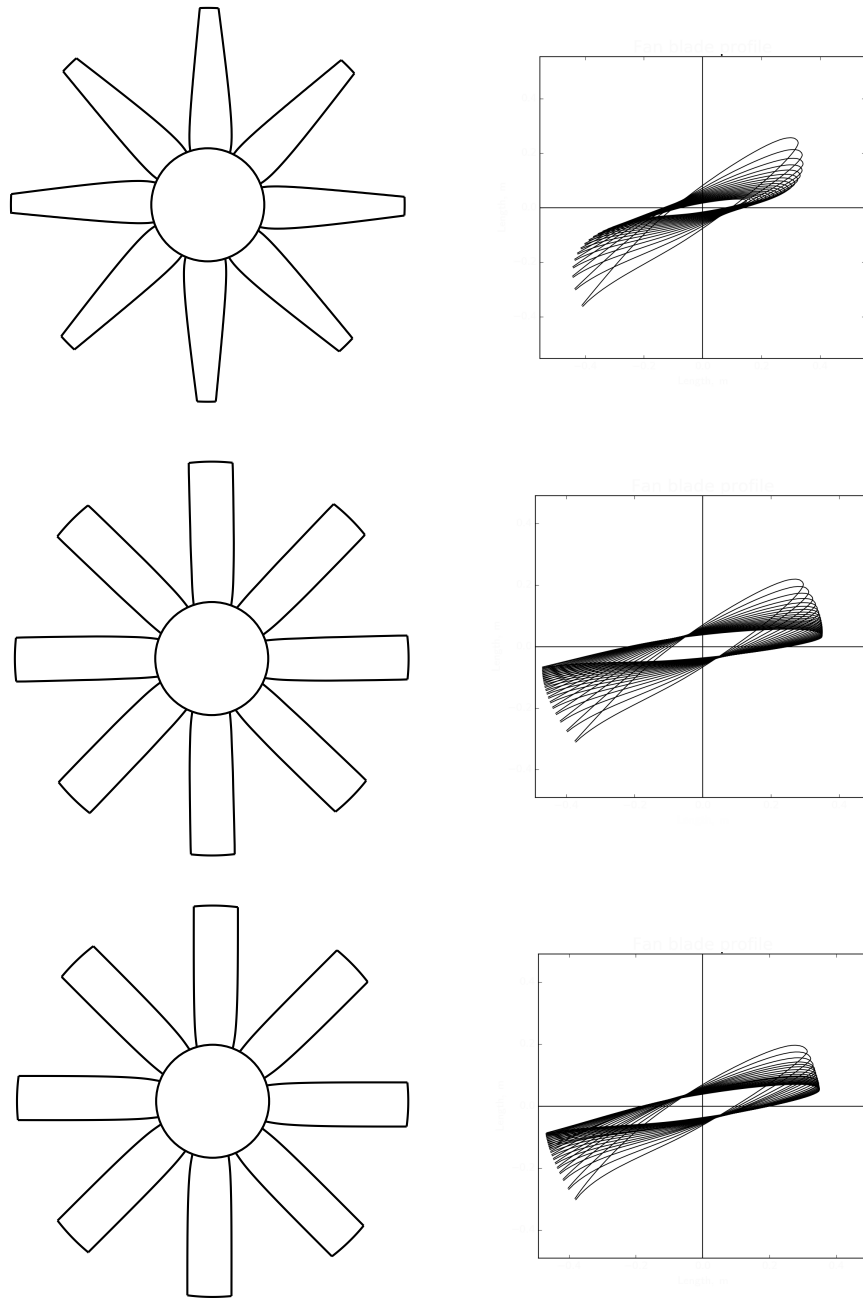
Figure C.1: Front view and stacking profiles of Concept 1 (top), Concept 2 (middle) and the M-fan (bottom)

reduction in blade twist results in a reduction in the axial length of the fan from 630 mm (Concept 1) to 500 mm (M-fan), half of the maximum axial length specified.

Figure C.1 also demonstrates that each of the designs has the same hub-tip

ratio, as determined by the method of Van Niekerk (1958). It was decided not to alter this as the method has been well proven in various studies undertaken on the B-fan to be very effective.

C.2 Performance Considerations

The main performance considerations involved in this study are meeting the fan performance specifications detailed in table 3.1 and Section 3.1, as well as designing a fan that is fit for purpose, namely operation in a forced-draft air-cooled heat exchanger. In order to assess the suitability of a design, it is modelled using an appropriate ADM to predict the performance of the design over a range of flow rates. This allows for the efficiency and power values estimated by the design code to be checked, as well providing an estimate of fan performance at off design conditions. As mentioned in Chapter 2 off design performance is an important consideration for fans of this application and an effective fan for an air cooled heat exchanger should have a steep pressure gradient.

The two most important performance considerations for this study are fan total-to-static efficiency and fan total-to-static pressure rise. The fan should as far as possible reach the efficiency and pressure specifications laid out in Section 3.1, while being fit for purpose based on the findings in Chapter 2. Figure C.2 shows the fan total-to-static efficiency and pressure rises over a selected range of flow rates.

In terms of fan total-to-static pressure rise figure C.2 demonstrates that all three designs match the operating point pressure of 116.7 Pa reasonably well. Concept 1 attains an operating point pressure rise of 111 Pa, Concept 2 attains 117.1 Pa and the M-fan attains 111.4 Pa. All designs thus attain operating point total-to-static pressure rises within 5% of the specified value. Figure C.2 shows that the total-to-static pressure vs. volume flow rate curve of the Concept 1 fan is shallower than those of the other two fans. This demonstrates that the fans designed using the vortex design method of Von Backström *et al.* (1996) are more suited to operation in air-cooled heat exchangers. Concept 2 has the best performance in terms of pressure, however the M-fan's performance is comparable, both in terms gradient and in terms of pressure rise attained.

The fan total-to-static efficiency curves shown in figure C.2 demonstrate that the M-fan is the only design to exceed the performance target of 60% at the operating point, as well as attaining higher efficiencies at all other flow rates surveyed. The M-fan attains an operating point efficiency of 63.1% compared to 57.9% and 59.7% for Concept 1 and 2 respectively. The discrepancy in efficiency is due to the camber optimisation process that was applied to the blading of the M-fan, as presented in Chapter 3. This process allows for the aerofoil lift-to-drag ratio to be optimised along the blade span, while con-
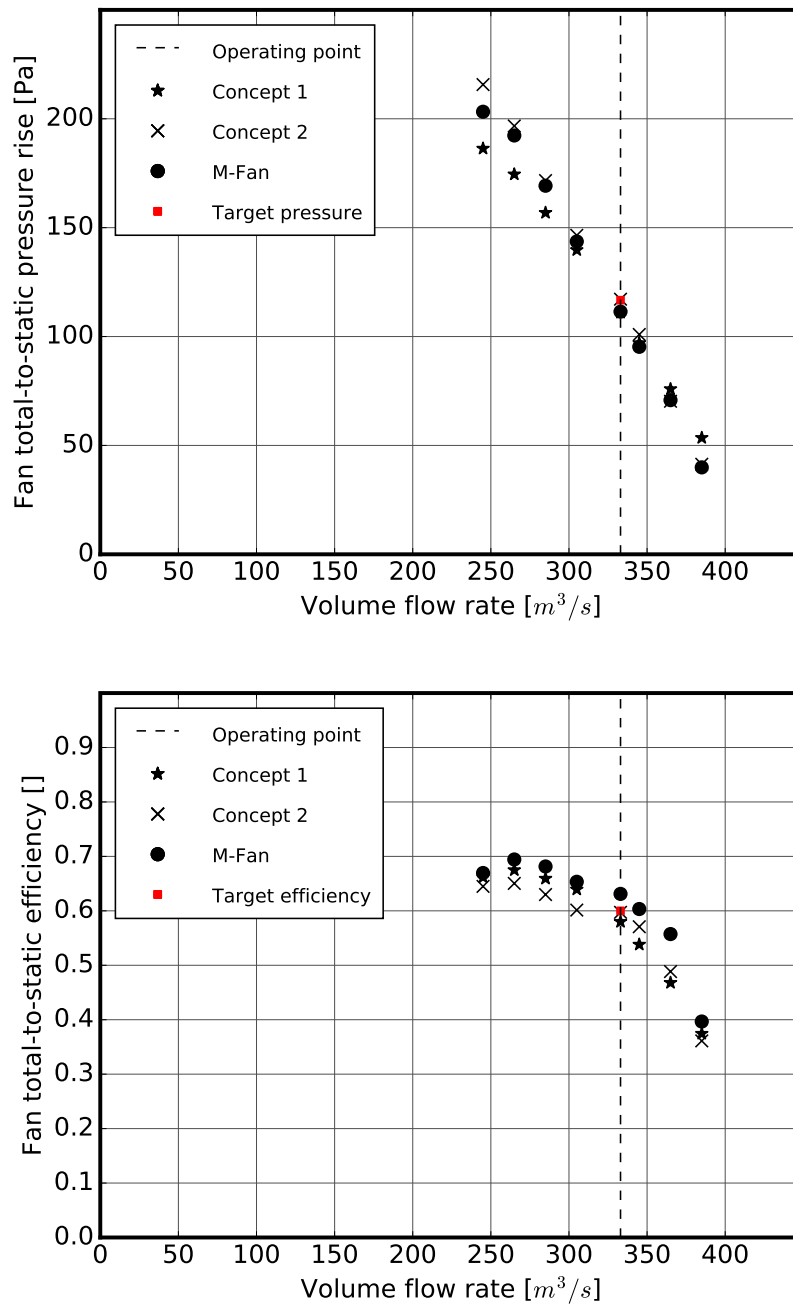
Figure C.2: ADM comparison of fan total-to-static pressure rise (top) and fan total-to-static efficiency (bottom) for the Concept 1, Concept 2 and M-fan designs

stricting the aerofoil angle of attack values at the design point to a reasonable range. This process leads to reduced drag at the blade tips, reducing power consumption and increasing fan total-to-static efficiency.
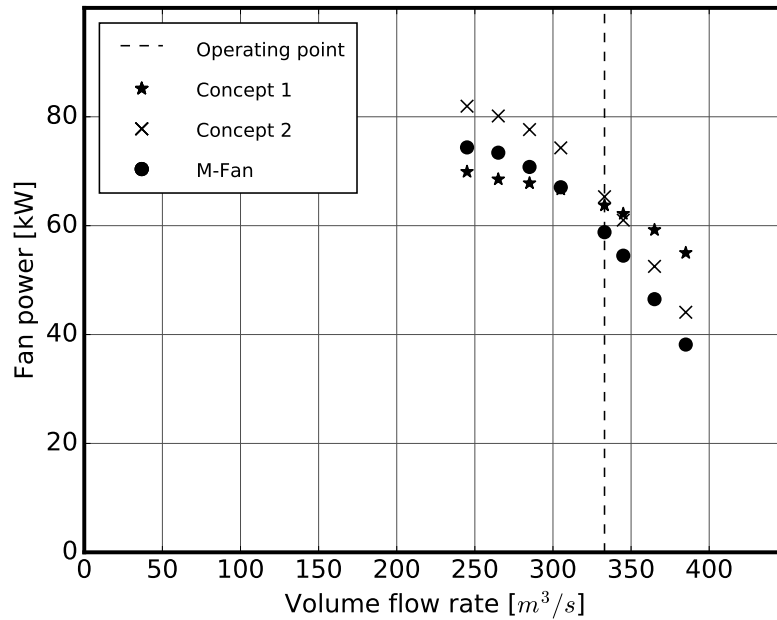
Figure C.3: ADM comparison of fan power consumption for the Concept 1, Concept 2 and M-fan designs

Figure C.3 shows the fan power vs volume flow rate curves for the three designs presented. It clearly demonstrates that the power consumption of the M-fan is significantly lower than that of the Concept 2 fan, as a result of the camber optimisation process previously mentioned. This also indicates that the M-fan will require a smaller, lighter drive motor than the Concept 2 fan. It is also clear that the power curve of the Concept 1 fan is shallower than that of both the M-fan and Concept 2 fan. This is related to the relatively shallow pressure characteristic for the Concept 1 fan, as demonstrated in figure C.2.

The above results indicate that the M-fan is the best performing fan, having a reasonable total-to-static pressure characteristic while having improved power consumption and total-to-static efficiency when compared to the earlier concepts. Fan performance results considered here also indicated that the development of the design procedure in Chapter 3 is valid and rational as the various steps included result in improved fan designs. Concept 2 is a clear improvement on Concept 1 in terms of suitability for purpose and operating point performance. This demonstrates that the differences in performance between the Concept 2 fan and the M-fan indicate that the camber optimisation procedure does indeed improve fan performance in terms of fan total-to-static efficiency while maintaining a good fan total-to-static pressure characteristic.

It is however at this stage important to note the uncertainties involved in the actuator disk model. Historical data shows that the ADM tends to under predict fan total-to-static pressure rise at low flow rates (Louw (2015),

Wilkinson *et al.* (2016)), hence the low flow region has been omitted from this survey. Studies by Louw (2015), Wilkinson *et al.* (2016) and Meyer and Kröger (2001) indicate that under certain conditions the total-to-static pressure rise and total-to-static efficiency estimated by the ADM is optimistic compared to experimental data. The findings of Van der Spuy (2011), Meyer and Kröger (2001) and Wilkinson *et al.* (2016) as well as several others show that the ADM is not particularly reliable for power prediction, tending to underestimate fan power consumption. Additionally the ADM, as well as the fan design procedure are incapable of modelling tip gap effects. For these reasons the P3DM model is developed, in order to assess the accuracy of the XFOIL ADM used to model the M-fan, as well as to validate the design procedure and model the effect of tip gap on the performance of the M-fan.

Appendix D

Aerofoil Lift Drag Properties

Accurate aerofoil lift drag data is key to producing an accurate, reliable fan design. According to Wallis (1983) it is important to select aerofoil sections carefully in order to ensure satisfactory stall properties as well as good pressure and efficiency characteristics. In the context of this study the actuator disk model (ADM) of Thiart and Von Backström (1993) which is used to compare designs is reliant on accurate aerofoil lift drag data. Without good quality data the results of the ADM will be questionable.

D.1   Introduction

In general there are two techniques to obtain the lift and drag properties of an aerofoil section, experimental tests in a wind tunnel or numerical simulations. Experimental aerofoil characterisation tests such as those performed by McGhee and Beasley (1976) and McGhee *et al.* (1977) are time consuming and costly, but provide accurate data with regards to lift, drag and stall properties. Numerical methods such as XFOIL (Drela (1989)) and two dimensional CFD simulations of aerofoil sections are relatively quick and easy ways of generating aerofoil lift and drag data, however these methods should be properly validated in order to ensure accuracy at the relevant flow conditions.

The design method presented in Chapter 3 makes use of XFOIL in order to manipulate aerofoil sections and generate the lift drag characteristics of these new sections. XFOIL is well suited for this application as it has a range of geometry manipulation and aerofoil design tools as describe by Drela and Youngren (2001). XFOIL also has the capability to produce aerofoil lift and drag data by means of a boundary layer solver as described by Drela (1989). XFOIL has successfully been used in studies by Cencelli (2006) and Carolus and Starzmann (2011*b*). Compared to two dimensional CFD simulations XFOIL is computationally light and efficient, making it far better suited to optimisation applications, such as the procedure described in Chapter 3. It should be noted however that parameters in XFOIL need to be set correctly

in order to attain reasonable results. Additionally XFOIL is unable to solve certain geometries as well as aerofoils operating at higher Reynolds numbers. For these reasons a study is carried out in this appendix in order to confirm whether or not XFOIL is suited for the generation of lift drag data for the design procedure detailed in Chapter 3 as well as the ADM described in Chapter 4. Lift drag data generated by XFOIL will be compared to experimental data and well as data generated by two dimensional CFD simulations in order to assess whether or not the XFOIL data is reliable. The CFD simulations were also carried out to assess whether CFD could be an alternative to XFOIL, as well as to generate comparative data for thicknesses where no experimental data is available. Experimental data is compared with CFD and XFOIL data for different Reynolds numbers experienced along the blading of the M-fan as well as varying aerofoil thickness, within the range encountered in the M-fan design.

D.2   CFD Model

Two dimensional CFD simulations of aerofoil sections are commonly used in literature to generate lift and drag polars. This method provides an alternative numerical means of generating data and could be integrated into a design procedure such as that described in Chapter 3. For this reason a two dimensional model of the NASA LS 0413 section is developed and the results compared to experimental and XFOIL data. A two dimensional model of the NASA LS 0409 profile is also developed for comparison with XFOIL as there is no experimental data available for this section. Both aerofoil sections are modelled with a circular computational domain with a diameter of 60 meters, as shown in figure D.1.

The domain consists of 350000 hexehedral elements meshed using ANSYS Workbench 16.0. The aerofoil section is 1 meter in length and placed at the centre of the domain as shown in figure D.1. The entire circumference of the domain is set to be a velocity inlet, with velocity components set according to the desired angle of attack and Reynolds number for each simulation. The reason for this, as well as the large distance between the boundary and the aerofoil section is to ensure as ideal as possible flow around the aerofoil. The perimeter of the aerofoil section is specified to be a smooth no slip wall.

The Spalart Allmaras turbulence model (Spalart and Allmaras (1992)) is applied in all simulations. This model was specifically developed for aerospace applications such as the modelling of aerofoils. In order to solve the boundary layer accurately the cells near the aerofoil section have been refined such that $y+ < 1$, in line with the requirements of the turbulence model, as shown in figure D.2. Lift and drag forces are calculated at the walls of the aerofoil section by means of a surface monitor, these values are then used to derive the lift and drag coefficients for the aerofoil section at the given angle of attack.

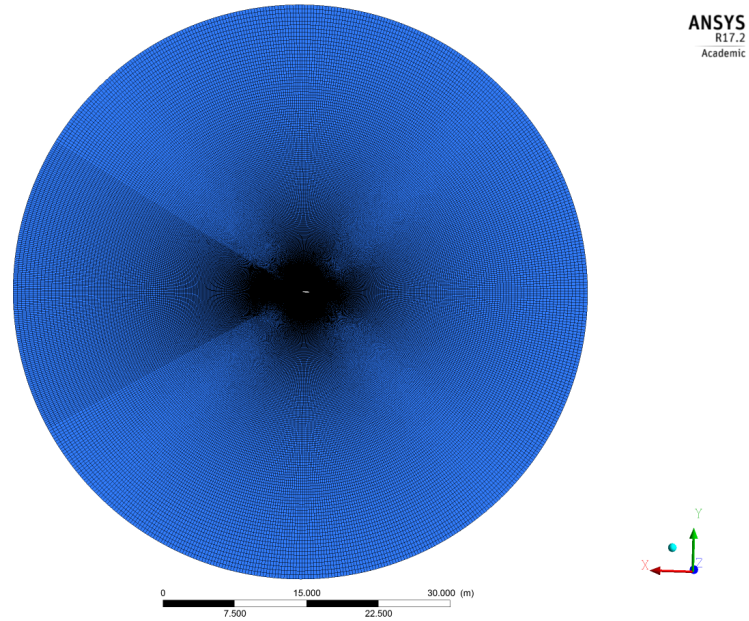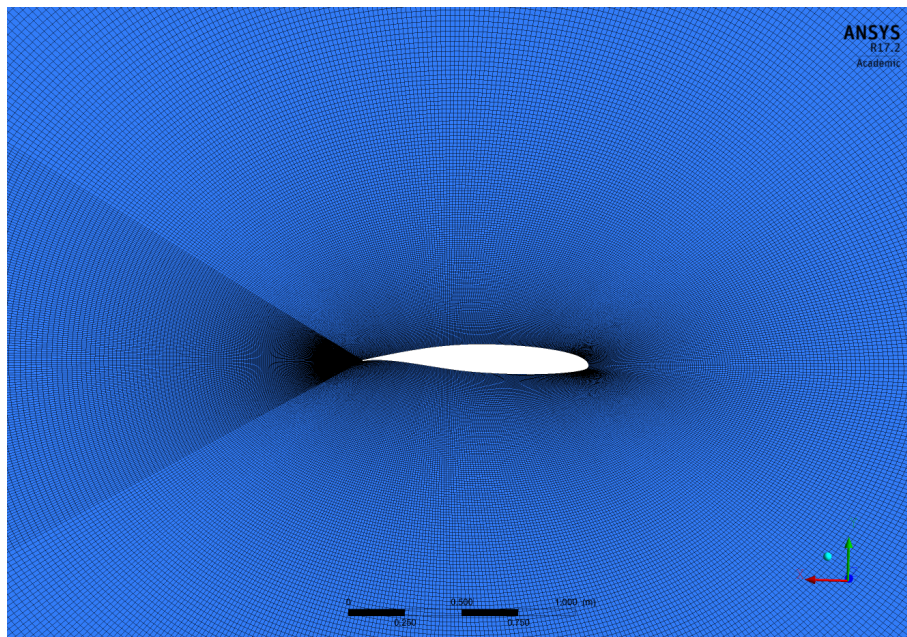Figure D.1: Computational domain and mesh for two dimensional aerofoil modelling

Figure D.2: Detail of the aerofoil section within the computational domain shown in figure D.1

All simulations are conducted within ANSYS FLUENT 16.0 and run across two processing cores. Solver settings applied are shown in table D.1. The momentum and pressure terms are under relaxed to 0.4 and 0.6 respectively

in order to aid convergence. All other values are set to the default values provided by FLUENT. Each simulation takes approximately 20 minutes to attain convergence, with higher angles of attack taking longer. Convergence levels attained in all cases are in the order of 10^{-5}.

Table D.1: ADM solver settings

Pressure - velocity coupling	SIMPLE
Pressure	Standard
Gradient	Green-Gauss node based
Momentum	Second order upwind
Modified turbulent viscosity	Second order upwind

D.3   XFOIL Validation

In order to validate the lift and drag data generation capabilities of XFOIL, lift and drag data obtain from XFOIL is compared to experimental data for the NASA LS 0413 aerofoil obtained by McGhee *et al.* (1977) as well as CFD generated data for two different Reynolds numbers, 2.1×10^6 and 3.2×10^6. Further XFOIL data is compared to CFD data for the NASA LS 0409 aerofoil section at a Reynolds number of 3.2×10^6. This is done as the M-fan blading has a minimum thickness of 9% at the tip and a maximum thickness of 13% at the root. The NASA LS 0413 is also used as the base aerofoil in the camber optimisation carried out in Chapter 3, thus all aerofoil sections along the blade span of the M-fan have a similar geometry to the NASA LS 0413 section. There is also a wealth of good experimental data available for the NASA LS 0413 section thanks to the work of McGhee *et al.* (1977).

Special attention is paid to setting the viscous parameters in XFOIL correctly. In this regard XFOIL has the capability to set trips on the aerofoil surface in order to control flow transition on the aerofoil surface. This function is useful if the transition point is known, which in this case it is not. The other parameter relevant to transition is N_{crit}, a user defined value which is the log of the amplification factor of the most amplified frequency which triggers transition Drela and Youngren (2001). This value is set to 9 by default, but can be adjusted in order to account for ambient factors that may influence transition Drela and Youngren (2001). In the case of this study the N_{crit} value is adjusted in order to improve agreement between the results of XFOIL and experimental data by accounting for possible flow disturbances and ambient factors not mentioned by McGhee and Beasley (1976).

D.3.1   Reynolds Effects

The M-fan blading has a large variation in Reynolds number across the blade span, owing to the small variation in chord length. It is well known that Reynolds number affects the lift drag characteristics of an aerofoil. For this reason XFOIL, two dimensional CFD and experimental data are compared for the NASA LS 0413 profile at different Reynolds numbers. This aims to assess the quality of the data generated by XFOIL at different Reynolds numbers, as well as determining the correct value of N_{crit} in each case.
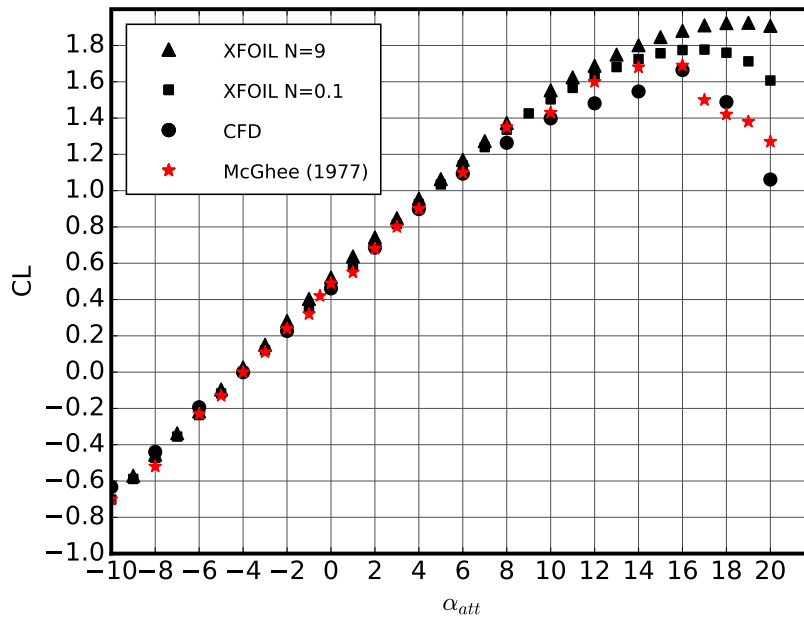

Figure D.3: C_L vs α_{att} for the NASA LS 0413 section at a Reynolds number of 2.1×10^6

Figure D.3 shows the C_L vs angle of attack properties for the NASA LS 0413 aerofoil section at a Reynolds number of 2.1×10^6, which is the approximate average Reynolds number of the M-fan blading. Data from XFOIL and CFD simulations are compared to the experimentally obtained data of McGhee *et al.* (1977). It can be seen in figure D.3 that both XFOIL simulations, as well as the CFD simulations agree well with the experimental data of McGhee *et al.* (1977) for angles of attack between -10 and 10 degrees. Beyond 10 degrees the lift coefficient values obtained by the CFD simulations deviate from the experimental data, although the CFD data does accurately predict the aerofoil's stall point. At angles of attack greater than 10 degrees the XFOIl simulation where $N_{crit} = 9$ tends to over predict the lift coefficient, this over prediction increases with angle of attack. The XFOIL simulation where $N_{crit} = 0.1$ agrees well with the experimental data until the stall point

($\alpha_{att} \approx 16°$). Beyond stall the XFOIL simulation does not correctly predict lift coefficient. This is due to the fact that XFOIL is a boundary layer solver and inaccurate once the boundary layer has separated from the aerofoil surface Drela and Youngren (2001).

Similar trends can be observed at the higher Reynolds number of 3.2×10^6, as shown in figure D.4. Once again all simulations correlate well with the experimental data of McGhee *et al.* (1977) in the linear region of the lift curve, however the CFD data begins to deviate at an angle of attack of 8 degrees. Beyond this angle of attack the data generated by the two dimensional CFD simulations become inaccurate, and the stall point is not accurately predicted. Both XFOIL simulations correlate well with the experimental data up to an angle of attack of 14 degrees. Beyond 14 degrees the simulation where $N_{crit} = 9$ starts to over predict lift coefficient, becoming increasingly inaccurate with increasing angle. As with the case shown in figure D.3, the XFOIL simulation where $N_{crit} = 0.1$ correlates well with the experimental data until the stall point ($\alpha_{att} \approx 17°$). Beyond stall the XFOIL results are once again inaccurate for the same reasons as earlier stated.

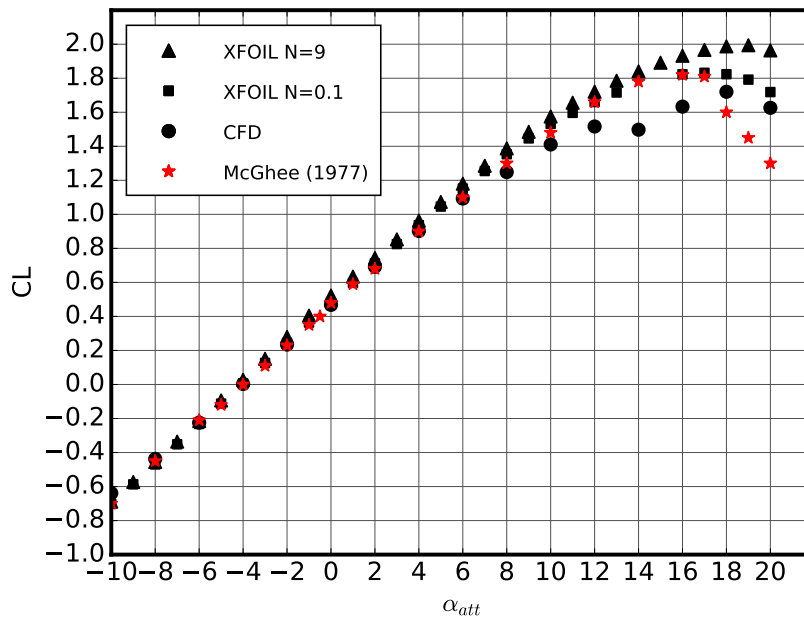Figure D.4: C_L vs α_{att} for the NASA LS 0413 section at a Reynolds number of 3.2×10^6

In terms of drag McGhee *et al.* (1977) present two sets of data at each Reynolds number, one set for a smooth aerofoil surface and another set for an aerofoil with surface roughness. Both of these data sets are compared to

drag data from the same two dimensional CFD and XFOIL simulations that generated the lift data in figures D.3 and D.4.

Figure D.5 shows the drag properties of the NASA LS 0413 aerofoil at a Reynolds number of 2.1×10^6. It can be seen that the experimental drag coefficient values with surface roughness are generally larger than those of the smooth aerofoil. At higher lift coefficients the values for both surfaces begin to correlate better. The two dimensional CFD simulations predict larger values of drag than both experimental data sets at all values of lift coefficient. The XFOIL simulation where $N_{crit} = 9$ tends to under predict drag values compared with both experimental data sets. As with the lift coefficients shown in figures D.3 and D.4 the divergence of the predicted drag values increases with lift coefficient. The XFOIL simulation where $N_{crit} = 0.1$ correlates better with the experimental drag coefficients at higher lift coefficients. This is significant as the ADM is used to predict fan performance at lower flow rates and therefore higher angles of attack and lift coefficients. The data from this simulation also correlates well with the data of McGhee *et al.* (1977) where the aerofoil has some surface roughness. This can be considered conservative for design and modelling purposes, as the final fan blades may not have a perfectly smooth surface finish when manufactured and installed.

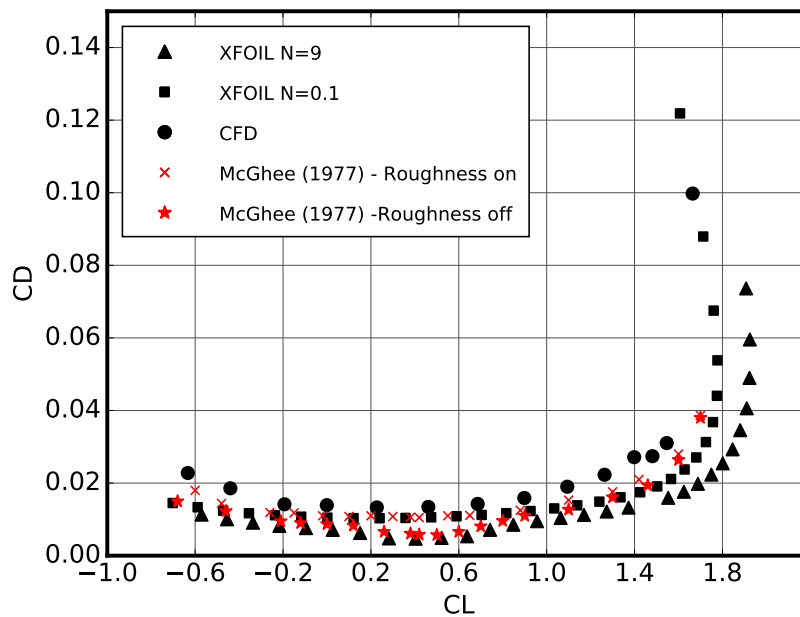Figure D.5: C_L vs C_D for the NASA LS 0413 section at a Reynolds number of 2.1×10^6

The same trends can be observed at a higher Reynolds number of 3.2×10^6, as depicted in figure D.6. The drag coefficient values predicted by two

dimensional CFD simulations are even less reliable at this Reynolds number, over predicting drag by as much as 50% at higher lift coefficients. Once again the drag values predicted by XFOIL where $N_{crit} = 9$ correlate well with the experimental data at smaller values of lift coefficient, however the drag values diverge from the experimental data for higher lift coefficients. As was the case for the lower Reynolds number, the XFOIL simulation where $N_{crit} = 0.1$ correlates well with the data of McGhee *et al.* (1977) where the aerofoil has surface roughness.
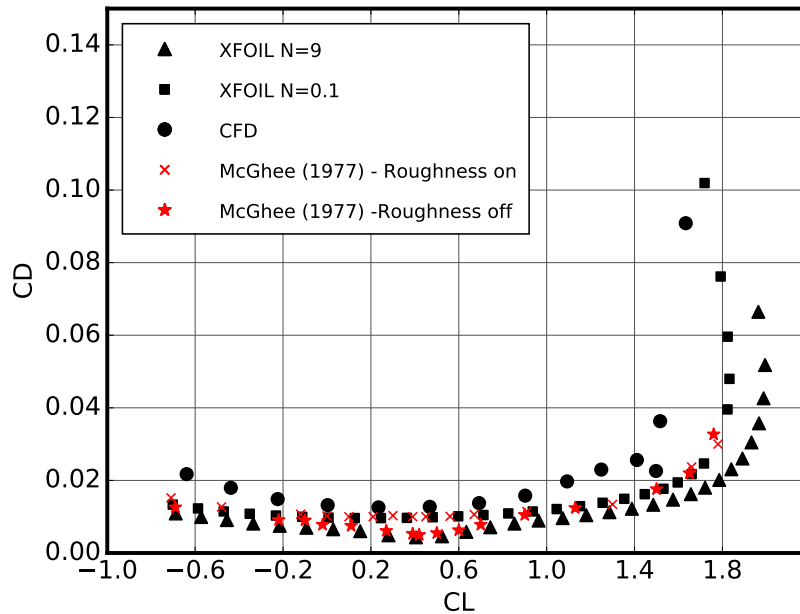
Figure D.6: C_L vs C_D for the NASA LS 0413 section at a Reynolds number of 3.2×10^6

D.3.2   Aerofoil Manipulation

As the aerofoil is manipulated in terms of thickness and camber it is important to check the validity of XFOIL for manipulated aerofoils. The maximum camber and thickness in the M-fan blading occurs at the blade root, where Reynolds numbers are relatively low. XFOIL was specifically developed as a low Reynolds number solver (Drela (1989)) and it has been shown to be reliable for low Reynolds number aerofoils provided the geometry is not particularly complex. Of more concern to this study is the accuracy of XFOIL at the blade tip region where the aerofoil section is at its thinnest and the Reynolds numbers are highest. For this reason the lift and drag properties of the NASA LS 0409 section (9% thickness) at a Reynolds number of 3.2×10^6 are simulated by

means of XFOIL and two dimensional CFD. As there is no experimental data available for this section, the results are compared in order to gauge whether or not there is any significant deviation from the trends shown in the previous section. The NASA LS 0409 section is chosen as it has the same thickness as the section at the blade tip of the M-fan. 3.2×10^6 is chosen for the Reynolds number as this corresponds well with the Reynolds number at the blade tip of the M-fan
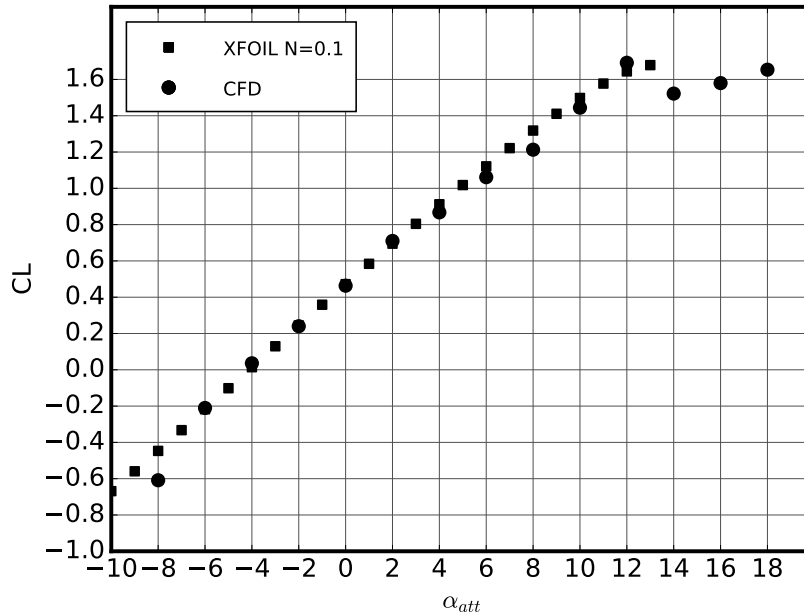
Figure D.7: C_L vs α_{att} for the NASA LS 0409 section at a Reynolds number of 3.2×10^6

Figure D.7 shows the lift coefficient vs angle of attack values predicted by XFOIL where $N_{crit} = 0.1$ and two dimensional CFD simulations. It can be seen that for angles of attack greater than 13° XFOIL did not converge. The CFD results indicate that stall may occur at angles of attack greater than 13°. This may explain why XFOIL does not occur at these values as the boundary layer solver used by XFOIL does not perform well beyond stall, especially for thin aerofoils where the onset of stall is more sudden. For angles of attack below 13° both data sets correlate well with one another, in a similar manner to that shown in figures D.3 and D.4. This indicates that for the points where XFOIL converges the results are valid.

Figure D.8 shows the drag coefficient vs lift coefficient for the NASA LS 409 aerofoil. For all values of lift coefficient the CFD simulations predict higher values of drag coefficient than XFOIL, in line with the results presented in the previous section. The drag coefficient values predicted by XFOIL are

significantly smaller than the drag coefficient values for the NASA LS 0413 section at the same Reynolds number (see figure D.6). This is in line with expectation as the NASA LS 0409 section has a smaller frontal area and surface area than the NASA LS 0413 section. Contrary to this the CFD simulations predict drag values greater or equal to those predicted for the NASA LS 0413 aerofoil. For this reason the XFOIL simulation is deemed to be a better representation of the drag properties on the NASA LS 0409 aerofoil section. This demonstrates that XFOIL is capable of providing reasonable aerofoil lift drag data for thin aerofoil sections at the highest Reynolds number present in blading of the M-fan.
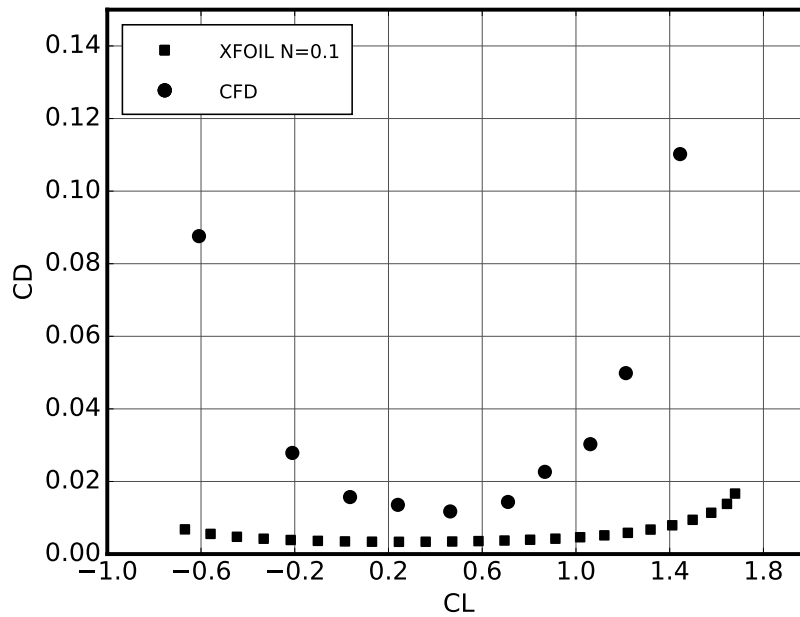
Figure D.8: C_L vs C_D for the NASA LS 0409 section at a Reynolds number of 3.2×10^6

D.4   Concluding Remarks

The results presented in this section demonstrate that XFOIL is capable of providing reasonably accurate aerofoil profile data. The accuracy of this data can be improved by setting the value of N_{crit} correctly. In the context of this study a N_{crit} value of 0.1 has been found to give the best results. At this point it is important to note that the N_{crit} value of XFOIL defines a limited range of flow effects, as detailed by Drela and Youngren (2001). These effects may or may not be present in the M-fan and a more detailed analysis would be required in order to determine the exact aerofoil properties of the M-fan

and the flow mechanisms present. This would allow for further optimisation, as well as more accurate polar prediction. This work is however beyond the scope of the present study, and the aerofoil polar values predicted by XFOIL where $N_{crit} = 0.1$ agree sufficiently well with experimental data for these simulations to be used to generate the aerofoil data used for the design procedure and the development of the ADM.

XFOIL is also shown to be more accurate than two dimensional CFD. The CFD simulations tend to correlate well with experimental data at neutral angles of attack, however they provide inaccurate data near and beyond the aerofoil stall point. This means that CFD simulations could be viable for fan design work, but not the development of the ADM. Another disadvantage of the CFD simulations is that they are more time and computational expensive than XFOIL, taking up to 30 minutes to reach convergence for each angle of attack. XFOIL was found to be capable of generating polar data for the full range of angles of attack presented here within 1 minute. This relatively fast computational time, as well as built in aerofoil design tools makes XFOIL better suited to the application presented in this study.

Appendix E

P3DM Mesh Sensitivity Study

In order to numerically model the M-fan accurately and in a computationally efficient manner a mesh sensitivity analysis is performed. This analysis aims to demonstrate the mesh sizing and quality limits in order to accurately model the fan. The mesh used consists of three sub-domains namely, the rotor, inlet and outlet sub-domains. The rotor domain is developed using ANSYS Turbogrid and consists of a structured hexehedral mesh that surrounds the blade. The inlet and outlet domains consist of unstructured polyhedral cells, in order to improve accuracy and reduce computational expense. These domains are generated using the geometric modelling and meshing tools within the ANSYS Workbench software package.

E.1   Rotor Mesh Density

In order to determine the required mesh density for this sub-domain several meshes were developed. Flow simulations on these meshes were then performed in ANSYS FLUENT 17.2 in order to determine the effect of mesh density. These tests focused on fan performance results, such as total-to-static pressure rise as well as improvement of mesh quality. In some cases two meshes of identical density, but varying bias are developed to determine the effect of mesh distribution. Meshes with high bias have more cells near the hub and shroud walls and fewer at the mid span. Meshes with low bias have a more even spanwise distribution of cells. The meshes used in this study consist solely of the rotor sub-domain detailed in Chapter 5, where the upstream and downstream mesh interfaces are set to be inlet and outlet boundary conditions. The flow rate is set to the design flow rate for the M-fan, $333\,\text{m}^3/\text{s}$. Owing to the proximity of the boundaries to the blade, the fan rotor is modelled without a tip gap for the purposes of this study, as the inclusion of a tip gap when the boundaries are so close to the fan blade results in difficulties obtaining convergence. The results of this survey, in terms of fan total-to-static pressure rise and total-to-static efficiency are displayed in table E.1. Mesh 1 in table

E.1 represents the smallest mesh density for which mesh quality is sufficient for the flow to be simulated.

Table E.1: Rotor mesh sensitivity

Mesh	No. elements	Δp_{ts} [Pa]	η_{ts}	Notes
1	298850	112.736	58.955	
2	597700	113.503	59.198	High bias
3	597700	113.462	59.148	Low bias
4	1793100	113.388	59.071	High bias
5	1793100	113.324	59.034	Low bias
6	2689450	113.251	59.006	
7	5379300	113.296	59.003	High bias
8	5379300	113.261	58.991	Low bias

It can be seen from the total-to-static pressure and efficiency values shown tin table E.1 that mesh density has a minimal effect on these results. Statistically, in terms of total-to-static pressure there is a 0.5% error between the results in table E.1, with a standard deviation of 0.168. There is an error of 0.331% between results for total-to-static efficiency, with a standard deviation of 0.00073%. As total-to-static efficiency is dependent on power, as well as volume flow and total-to-static pressure, its clear that the variation in power between the different mesh densities must be small. Given that mesh 1, with a density of 298850 cells, has the minimum number of cells for which FLUENT's minimum mesh quality limits are met, it is clear that the rotor-sub domain is mesh independent. It is apparent that adjusting the span wise mesh bias to have a higher mesh density at the hub and shroud wall regions has a negligible effect on fan performance results.

Mesh quality is an important consideration when meshing turbomachinary blading. Poor quality mesh elements may result in simulations being unable to converge, or erroneous results due to numerical instability. ANSYS Turbogrid provides the following set of mesh quality guidelines:

- Element volume: Must be greater than zero

- Face angle: Must be between 15° and 165°

- Maximum edge length ratio: 100

- Element volume ratio: Less than 20

- Connectivity number: Less than 12

Although the meshes listed in table E.1 all conform to these constraints, the influence of mesh density on quality in the rotor-sub domain is further

investigated. This is to ensure that the final mesh density selected is of high enough quality to ensure convergence and accurate results at all flow rates considered by this study. Quality is assessed using three parameters generated by FLUENT, minimum orthogonal quality, maximum orthogonal skew and maximum aspect ratio. The definitions of these parameters are provided in the ANSYS FLUENT User's Guide (ANSYS inc. (2015)). The worst values for these parameters are given by FLUENT, under the assumption that most elements will have much better values than the worst case. According to the User's Guide (ANSYS inc. (2015)), an orthogonal quality near 0 corresponds with poor mesh quality. Likewise an orthogonal skew value near 1 corresponds with low quality. Aspect ratio indicates the stretching of a cell, in general it is best minimised although this is dependent on element types and the flow being modelled. The effect of mesh density on the mesh quality of the rotor sub-domain, in terms of these parameters, is shown in table E.2. The mesh numbers in table E.1 correspond with those in table E.2.

Table E.2: Rotor mesh quality

Mesh	No. elements	Min ortho quality	Max ortho skew	Max aspect ratio
1	298850	5.29E-02	0.947	388.066
2	597700	0.173	0.827	267.544
3	597700	0.097	0.903	255.934
4	1793100	0.392	0.608	255.934
5	1793100	0.303	0.697	255.934
6	2689450	0.405	0.594	255.934
7	5379300	0.396	0.604	255.934
8	5379300	0.395	0.605	255.934

The mesh quality data in table E.2 indicates that mesh quality improves with mesh density until a mesh density of 2689450 elements. Beyond this mesh density, increasing the number of elements has less effect on mesh quality. It is also noted that high biased meshes have better quality than low biased meshes for mesh densities of less than 2689450 elements.

Considering the data presented in tables E.1 and E.2 it is clear that quality is more of a limiting factor to mesh density than fan performance estimation. For this reason all meshes used in this study have a rotor sub-domain density of 1.8×10^6 or larger. This ensures that the sub-domain has reasonable mesh quality to ensure good results at all flow rates, while minimising computational expense as far as possible. Additional the mesh density chosen also ensures that the mesh is fine enough to accurately model any local effects in the flow field in the vicinity of the M-fan blading.

E.2   Inlet and Outlet Length

The full P3DM domain consists of the rotor sub-domain, which is adjoined by the inlet and outlet sub-domains. These sub-domains aim to move the inlet and outlet boundaries further from the fan blading in order to reduce the possibility of reverse flow at the boundaries, as well as to aid convergence. In order to find suitable axial lengths for the inlet and outlet sub-domains, as study is performed to determine the impact of the axial length of these sub-domains on the fan performance predicted by the P3DM. The influence of mesh density in these sub-domains is also considered for the inlet and outlet lengths presented in Chapter 5.

Outlet sub-domains of various lengths were coupled to the zero tip gap rotor-sub domain and simulated at a flow rate of $333\,\mathrm{m^3/s}$. The results of these simulations, shown in table E.3, indicate that the length of the outlet sub-domain has negligible influence on fan performance data predicted by the simulations. For this reason an outlet length of $4\,\mathrm{m}$ is chosen, as it removes the outlet boundary a conservative distance from the fan blading.

Table E.3: Outlet length

Length [m]	Δp_{ts} [Pa]	η_{ts}
2	114.708	59.516
4	115.271	59.603
8	115.272	59.604
12	115.272	59.604
16	114.718	59.532
20	114.722	59.533

Similarly inlet sub domains with varying lengths where tested in conjunction with the rotor sub-domain and the $4\,\mathrm{m}$ outlet sub domain. The fan performance results in table E.4 indicate that as with outlet length, the influence of inlet length on the fan performance results is very small. An inlet length of $4\,\mathrm{m}$ is chosen for the inlet sub-domain as it is considered conservative. This length is also short enough that the inlet flow field is close to the assumed inflow conditions of the design method.

Table E.4: Inlet length

Length [m]	Δp_{ts} [Pa]	η_{ts}
2	114.368	59.507
4	114.546	59.403
6	114.739	59.369
8	114.825	59.319

The influence of the mesh densities of the inlet and outlet sub-domains is checked in conjunction with the mesh densities of the interface boundaries of these sub-domains. This is achieved by increasing the number of cells on the interface boundary and reducing the mesh inflation rate from this face. This results in a higher overall mesh density and an increased number of elements at the interfaces with the rotor sub-domain. The results for for this variation in mesh density are shown in table E.5, where the number of elements includes the elements in the rotor sub-domain. It can be seen from the data in table E.5 that mesh and interface density changes have a negligible effect on the fan performance values predicted by the P3DM.

Table E.5: Mesh density

Number of elements	Δp_{ts} [Pa]	η_{ts}
5866640	115.830	59.706
8671864	114.660	59.435

In conclusion this analysis has shown that an inlet sub-domain length of $4m$ and an outlet domain length of $4m$ are sufficient for the purposes of this study. Additionally these two sub-domains have adequate mesh densities to produce reliable results.

E.3   Tip Gap Density

In order for tip effects to be correctly modelled, there have to be sufficient elements present in the gap between the blade tip and the shroud. This is of particular importance as there is an interaction between the boundary layers of these two surfaces. Additionally flow structures in this region tend to be small and losses occurring in the tip gap can be significant. For this region the design tip and reduced tip meshes are run with two different tip gaps to determine whether or not 40 spanwise elements between the blade tip and shroud is sufficient.

Table E.6: Tip gap mesh density density

Tip gap	Number of elements	Δp_{ts} [Pa]	η_{ts}
reduced tip	40	104.154	55.828
	80	103.622	55.669
design tip	40	91.075	51.516
	80	90.457	51.320

Considering the results presented in table E.6, doubling the number of elements in the tip gap to 80 spanwise elements has a very small impact. Although

both total-to-static pressure and total-to-static efficiency are slightly reduced by increasing the number of elements in the tip gap, this small reduction does not justify the gain in computational time. Therefore for the purpose of this study 40 spanwise elements between the blade tip and shroud is considered adequate at both tip gaps tested.

E.4   Concluding Remarks

The mesh sensitivity study presented here demonstrates that the P3DM developed in Chapter 5 adequately satisfies geometric and mesh requirements for the purposes of this study. It is, however, important to note this mesh sensitivity study is by no means exhaustive. All simulations performed in this mesh sensitivity study were conducted at a flow rate of $333\,\mathrm{m}^3/\mathrm{s}$, the design flow rate for the M-fan. This was done as this flow rate is of particular importance in the greater context of this study. Due to the fact that only steady state simulations are performed in this study, this is considered accurate. P3DM studies of fans operating at lower flow rates, such as the work of Louw (2015), require further mesh sensitivity analysis including simulations of meshes with variable densities at lower flow rates. Should the simulation be transient, further work must also be undertaken to establish the effect of mesh and time step on the solution.